DESIGN AND PROCESSING OF CHARGE TRANSPORT POLYMER SEMICONDUCTORS AND THEIR APPLICATIONS IN N-CHANNEL ORGANIC FIELD EFFECT TRANSISTORS

A Dissertation
Presented to
The Academic Faculty

by

Carolyn Buckley

In Partial Fulfillment
of the Requirements for the Degree
Doctor of Philosophy in the
School of Chemistry and Biochemistry

Georgia Institute of Technology
August 2019

DESIGN AND PROCESSING OF CHARGE TRANSPORT POLYMER SEMICONDUCTORS AND THEIR APPLICATIONS IN N-CHANNEL ORGANIC FIELD EFFECT TRANSISTORS

Approved by:

Dr. Elsa Reichmanis, Advisor
School of Chemical & Biochemical Engineering
Georgia Institute of Technology

Dr. Will Gutekunst
School of Chemistry & Biochemistry
Georgia Institute of Technology

Dr. David Collard
School of Chemistry & Biochemistry
Georgia Institute of Technology

Dr. M. G. Finn
School of Chemistry & Biochemistry
Georgia Institute of Technology

Dr. Natalie Stingelin
School of Materials Science & Engineering
Georgia Institute of Technology

Date Approved: May 14th, 2019

ACKNOWLEDGEMENTS

Frankly, none of this would have been possible without the support and guidance of my advisor, Dr. Elsa Reichmanis. I am incredibly grateful for the opportunities she provided me, and for her invaluable guidance and advice that helped me navigate many low points in graduate school. I would also like to express my gratitude towards my fellow research group members who not only provided keen insight, new perspectives, and support and advice in the lab but whose friendship, humor, and optimism helped me through difficult times. Dr. Zhibo Yuan, Dr. Guoyan Zhang, Dr. Michael McBride, Dr. Bailey Risteen, Dr. Yo Han Kwon, Dr. Rui Chang, Brian Khau, Kristen Minnicci, Sujin Leeand Audrey Scholz were always willing to help no matter how busy they were or bizarre the request. I am truly grateful for their excellent company. I would also like to thank Dr. Ragunath Desari for his exceptional insight into synthetic chemsitry and for his support throughout the years.

I would also like to thank my family and friends for their constant support throughout the years. I would not have survived the struggles of the first years of graduate school without Dr. Hannah Narcross, who has been and continues to be a wonderful friend. I would like to thank my parents from the bottom of my heart for their continual support and for always cheering me on. Lastly, I would like to thank my wonderful husband Hanmin. I would not have been able to complete graduate school without his love, support, and humor. I truly could not have wished for a better partner to go through life with, and I look forward to the next chapter together.

TABLE OF CONTENTS

LIST OF TABLES

LIST OF FIGURES

LIST OF SYMBOLS AND ABBREVIATIONS

μ	Charge carrier transport mobility, $cm^2V^{-1}s^{-1}$
μ_e	Electron mobility, $cm^2V^{-1}s^{-1}$
μ_h	Hole mobility, $cm^2V^{-1}s^{-1}$
HOMO	Highest occupied molecular orbital, eV
LUMO	Lowest unoccupied molecular orbital, eV
SOMO	Singly occupied molecular orbital, eV
NTO	Natural transition orbital
IP	Ionization potential, eV
EA	Electron Affinity, eV
$I_{on/off}$	Current on/off ratio
V_T	Threshold voltage, V
V_{SD}	Source-drain voltage, V
I_{SD}	Source-drain current, A
E_g	Bandgap, eV
E_g^{opt}	Optical gap, eV
λ	Wavelength, nm
λ_{max}	Wavelength at max absorption, nm
CV	Cyclic voltammetry
DPV	Differential pulse voltammetry
UPS	Ultraviolet photoelectron spectroscopy
AFM	Atomic force microscopy

GIWAXs	Grazing incidence wide angle X-ray scattering
DFT	Density functional theory
t	Transfer integral
λ_E	Reorganization energy, eV
OFET	Organic field effect transistor
DSC	Differential scanning calorimetry
TGA	Thermogravimetric analysis
NMR	Nuclear magnetic resonance (spectroscopy)
eV	Electron-volt (unit of energy)

SUMMARY

The development of π-conjugated polymeric semiconductors for use in organic field effect transistors (OFETs) has been the subject of intense research focus for its potential in realizing low-cost, large-area, and flexible devices such as sensors, displays, and radio-frequency identification tags. While significant progress has been made in high-performance p-channel (hole-conducting) materials, that of their n-channel (electron-conducting) counterparts lags far behind. To enable the implementation of complementary organic-semiconductor (complimentary metal-oxide semiconductor)-like logic circuits, it is imperative to improve the electron mobility and ambient stability of unipolar n-channel conjugated polymers to match that of that of their p-type counterparts, while maintaining processability.

The prevailing donor-acceptor (D-A) design motif has led to considerable advances in polymer semiconductor performance as it allows for the fine-tuning of frontier molecular orbitals for efficient charge injection into electrodes in addition to promoting strong intermolecular π-π stacking interactions that facilitate charge transport. However, this design strategy has proven to be of limited use in developing n-channel conjugated polymers because there are relatively few building blocks with sufficient electron deficiency to achieve an electron affinity higher than +4 eV for facile electron injection and operational stability of resultant polymers. To this end, this thesis will discuss an alternative strategy of developing all-acceptor (A-A) polymers to minimize intramolecular charge transfer and preserve polymer low-lying frontier molecular orbitals. In carefully reviewing the literature, electron-withdrawing building blocks were chosen for synthesis

to be incorporated into promising A-A polymer structures in a combinatorial study. The optoelectronic properties of the polymers were characterized through cyclic voltammetry, UV-Vis and photoluminescence spectroscopy, and ultraviolet photoelectron spectroscopy. The charge carrier transport properties were investigated using bottom-gate/bottom-contact OFET device architectures. The polymer semiconductors were either spin-coated or blade-coated onto Si wafers with gold contacts and annealed at various temperatures. OFET performance studies including transfer and output curves allowed for the calculation of electron mobilities and demonstrated the unipolar (solely-electron-conducting) behavior of the A-A polymers. The polymer thin-film microstructures were investigated by 2D grazing incidence wide-angle X-ray scattering (2D-GIWAXS) and atomic force microscopy (AFM).

CHAPTER 1. INTRODUCTION

1.1 Organic Electronics

Organic materials have long played passive yet crucial roles in the electronics industry as lithographic photoresists defining key circuitry patterning and as insulators and dielectrics in the packaging of chips.[1] However since the discovery of electrical conductivity in doped polyacetylene in 1977,[2] organic semiconductors (OSCs) have been the focus of intense research efforts in developing the next generation of *active* electronic materials with optoelectronic functionalities in devices offering capabilities not readily achievable with conventional materials, combining the electronic advantages of traditional inorganic semiconductors with the chemical and mechanical benefits of organic compounds such as plastics.[3] In marked contrast with their inorganic counterparts, OSCs are lightweight, mechanically flexible, can be optically transparent, and most significantly are solution-processable; making them amenable to large-area and low-temperature deposition techniques compatible with a variety of inexpensive substrates (Figure 1-1). While not destined to replace silicon-based technologies, the potential for low-cost device fabrication suggests that OSCs can be competitive with existing applications with continued innovations in processing techniques, and capture otherwise inaccessible novel applications.[4,5]

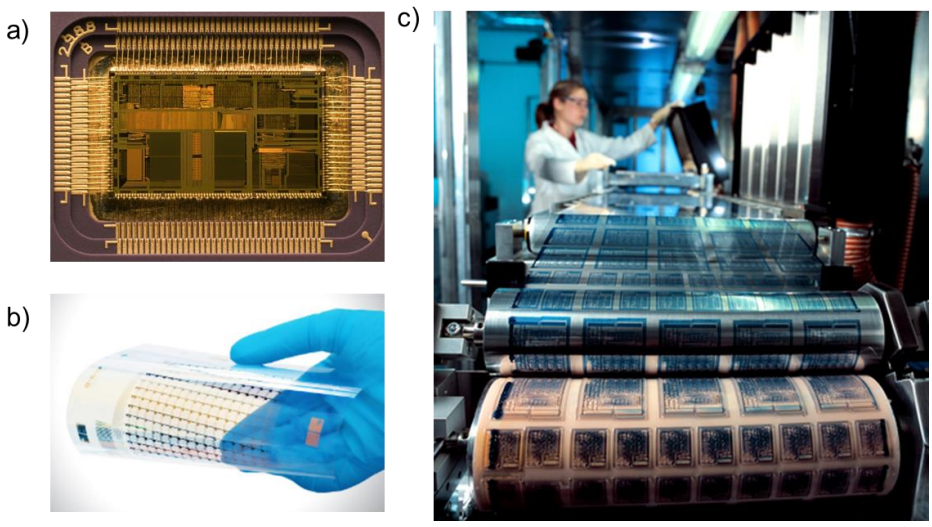

Figure 1-1 Commercialized microelectronic devices. a) Si-based microprocessor (Intel) b) Inkjet-printed flexible organic thin film transistor (BASF) c) roll-to-roll printing of organic electronic components (PolyIC).

The rapid advancement of the field over the last two decades has led to the development of numerous applications (Figure 1-2). Advances in organic light emitting diodes (OLEDs) have led to commercialized applications including foldable displays,[6] flexible solid-state lighting,[7] and energy-efficient color displays such as those seen in smart phones[8] and televisions with exceptional color purity.[9] Organic photovoltaics and dye-sensitized solar cells are promising alternative energy technologies that not only have the potential to reduce our dependence on fossil fuels but also enable small distributed energy generation that can deliver power to those without access to an electric grid.

Figure 1-2 Example applications of organic electronics. Clockwise from top left: wireless electrocardiogram and photoplethysmograms on infant (John Rogers, Northwestern University); rollable display (LG); transparent OLED lighting tiles (Osram (Siemens)); printed organic solar cell (InfinityPV).

The following will explore the fundamentals of polymeric semiconductors and the organic field effect transistor devices they are incorporated into.

1.1.1 Conductivity and Charge-Carrier Mobility

Electronic devices require materials with the ability to conduct an electrical current, which is quantified by the *conductivity* (σ) of the material. Semiconductors are a class of materials having conductivities between that of metals and of insulators (e.g. glass). The electrical conductivity of a semiconductor is proportional to the product of the charge carrier concentration and the *mobility* (μ) of these charge carriers, which is defined as the velocity of the charge carriers in a given material per unit of externally applied electric field. Equation 111 shows the expression of conductivity in a semiconductor:

$$\sigma = \frac{J}{E} = ne\mu \tag{1}$$

Where J is the current density (Acm^{-1}), E is the magnitude of the electric field (Vcm^{-1}), n is the number density of charge carriers (cm^{-3}), e is the unit of elementary charge (C), and μ is the charge mobility ($cm^2V^{-1}s^{-1}$). The charge carrier mobility is one of the key parameters used in assessing the electrical performance of a semiconductor material within a device.

1.1.2 Molecular and Electronic Structure of Organic Semiconductors

Example molecular structures of some common organic semiconductor materials are shown in Figure 1-3. The π-conjugated backbones characteristic to these materials impart the ability to conduct charge carriers and interact with light, with the optoelectronic properties dictated by their frontier molecular orbitals.

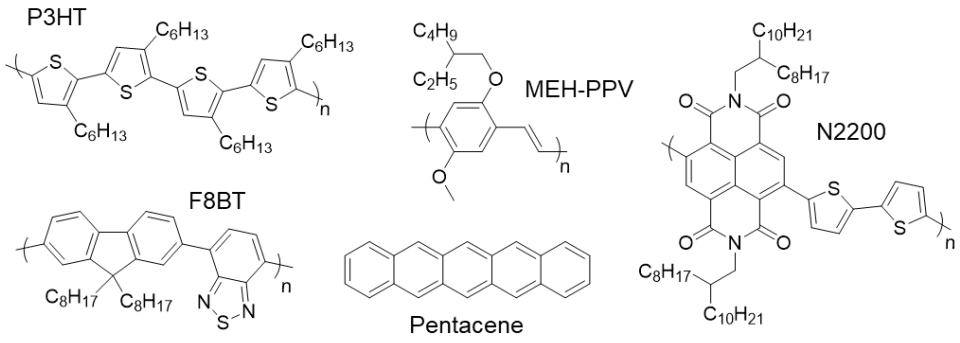

Figure 1-3 Molecular structures of representative common organic semiconductors: poly(3-hexylthiophene) (P3HT), poly(9,9-dioctylfluorene-*co*-benzothiadiazole) (F8BT), poly[2-methoxy-5-(2'-ethylhexyloxy)-*p*-phenylene vinylene] (MEH-PPV), pentacene,

poly{[N,N'-bis(2-octyldocecyl)-napthalene-1,4,5,8-bis(dicarboximide)-2,6-diyl]-*alt*-5,5'-(2,2'-bithiophene)} (N2200).

The hybridization of the conjugated backbones creates a plane of empty p-orbitals perpendicular to the sigma bonding structure which serves as a pathway for the charge carriers to travel through (Figure 1-4). The side-by-side overlapping of atomic p-orbitals is known as π bonding ('conjugation'), which creates molecular π orbitals. Interacting π orbitals come together to form bonding (π) and antibonding (π*, empty) orbitals. Bonding interactions where the parity of the interacting orbitals match (denoted by color in Figure 1-4, yellow box) increase the electron density between two atomic nuclei, while antibonding interactions decrease the electron density (manifested as 'nodes' in the wavefunctions). As π orbitals are higher in energy than σ orbitals, the frontier molecular orbitals (the highest energy orbitals, known as the HOMO and the LUMO) are π orbitals. As the number of repeating conjugated units increases in a polymer chain, the growing number of π/π* orbitals become closer in energy and lose distinction, eventually forming a delocalized band structure similar to that seen in inorganic materials such as silicon (Figure 1-4). Additionally, the energy of the HOMO increases and that of the LUMO decreases, bringing these orbitals closer in energy and decreasing the 'band gap'. When the band gap decreases to between 2 eV - 0 eV, the material is no longer an insulator and now behaves as a semiconductor.

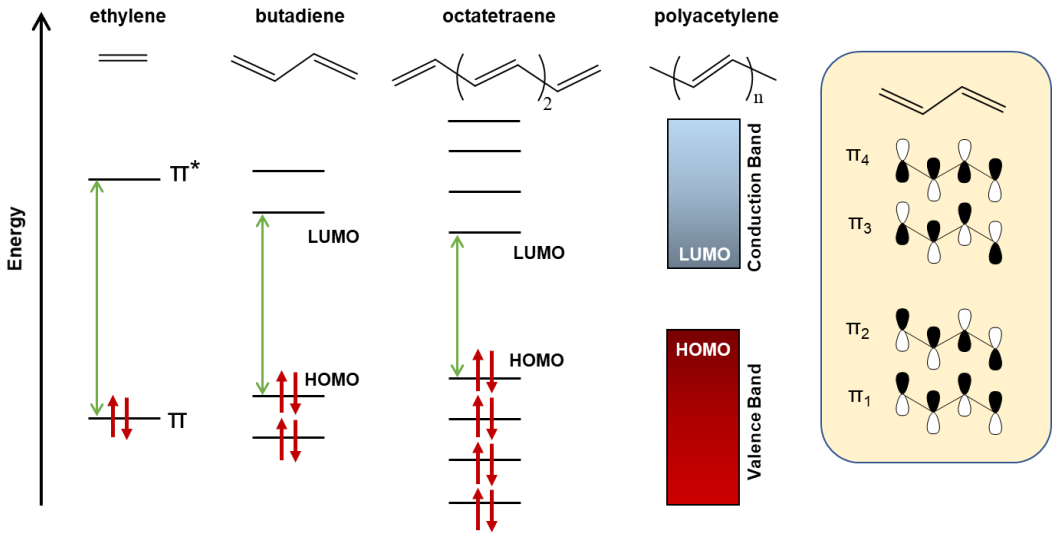

Figure 1-4 Evolution of frontier molecular orbital energy levels with increasing conjugation length in the polyene series, leading to a band structure as the number of repeat units approaches infinity.

The band gap energies typical of organic semiconductors happen to be in the visual range of the spectrum, making this class of materials particularly colorful. The energies of the HOMO and LUMO of a molecule can be 'tuned' by the introduction of electron-donating or -withdrawing moieties into the conjugated molecular system. In polymeric donor-acceptor (D-A) systems consisting of alternating electron-rich (donor) and electron poor (acceptor) monomer units, they hybridization of the D-A fragments leads to the donor contributing to the polymer HOMO and the acceptor contributing the polymer LUMO (Figure 1-5).[10–12] Though simple, the D-A molecular design strategy is powerful in that it enables control of a crucial energy gap which determines the optical, redox, and electrical transport properties of a material. This has allowed the development of materials with targeted properties 'tailored' to the specific requirements of electronic devices including OLEDs and OPVs, and the formation of ultra-low bandgap copolymers.

The term ‘electronic coupling’ describes the extent to which the frontier energy orbitals of two adjacent molecular entities are split when they interact with each other (Figure 1-4).[13] As this is essentially a function of the wavefunction overlap, it is influenced by the intermolecular distance and the lateral displacement between the two entities (as the phase difference between wavefunctions determines the bonding/anti-bonding patterns). The extent of electronic coupling in organic semiconductors is critical to the charge transport properties of materials (as will be described below), including coupling between adjacent entities within a polymer chain and between entities on separate chains. For these reasons, organic semiconductors are designed to maximize the planarity of the conjugated structures and to decrease the torsional angles along the polymer chains.

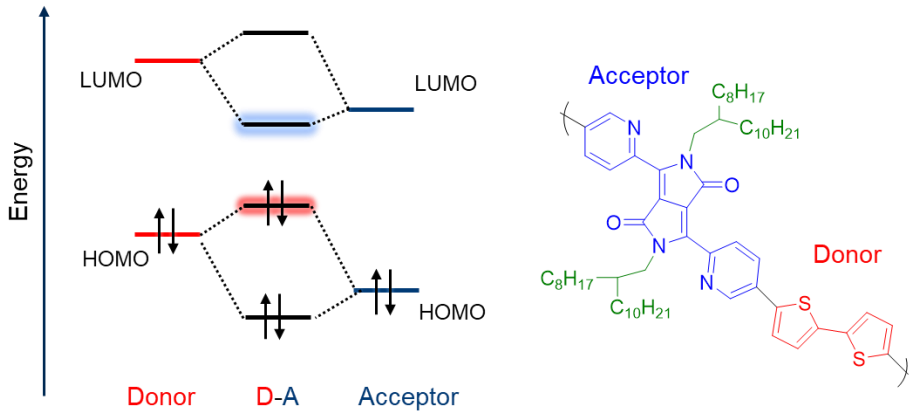

Figure 1-5 Orbital hybridization of D-A systems (left), and example D-A polymer (right).

1.1.2.1 Characterization of Electronic Structure

The preceding discussion described the electronic structure of organic semiconductors using qualitative molecular orbital (MO) theory which has a theoretical foundation in quantum mechanics, specifically on the Schrödinger equation relating the total energy of a molecule to a wavefunction describing the molecular configuration. Most

simply, an individual molecular orbital is a one-electron wavefunction associated with a specific energy level (and as such, is not an experimental observable).[14] The MO energies and wavefunction distributions of molecules in various geometries and electronic states can be calculated using a variety of computational methods,[15] with density functional theory (DFT) functionals used most frequently in organic electronics.[16,17] These computational tools have proven invaluable to the elucidation of electronic structure-property relationships and understanding the fundamental properties of extended conjugated materials. However, it is important to realize that such calculations *only* provide useful information when the inherent errors and limitations of the functionals used are recognized[18,19] and the validity of the results are critically assessed.[20,21] Computational results are ultimately approximations derived from theoretical frameworks and do not replace empirical evidence from experiment, but are indispensable as they allow for insight into phenomena that cannot be probed experimentally.

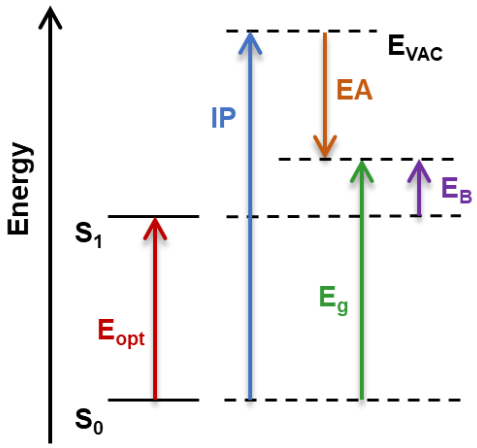

Figure 1-6 Depiction of the experimentally observable energy levels in organic semiconductors, with S_0 denoting the electronic ground state and S_1 the lowest excited state. Adapted from reference.[22]

It is often claimed that the HOMO and LUMO are directly measured with experimental ionization potentials according to Koopman's theorem, which states that the first vertical ionization potential (IP) of a molecule can be considered as the (minus) energy of the HOMO, and likewise the first vertical electron affinity (EA) the (minus) energy of the LUMO ('vertical' meaning no change in geometry is assumed) (Figure 1-6).[23,24] The IP (also known as the ionization energy[25]) is formally defined as the energy required to remove an electron from a gaseous neutral atom or molecule, while the EA is the energy required to remove an electron from a negative ion in the gaseous state.[26] The IP and EA are essentially the differences in energy between the neutral *N*-electron state and the respective $N \pm 1$ electron ionized states.[22] In the molecular case, the difference between the IP and EA is known as the 'fundamental gap', which correlates with the band gap (E_g) between valence and conduction bands in polymers and other organic solids with more delocalized band structures. Ultraviolet photoelectron spectroscopy (UPS) is used to assess the ionization energies of valence electrons, which involves measuring the kinetic energy

of electrons emitted from a sample irradiated with ultraviolet photons under ultra-high vacuum (~10^{-9} torr) which is then related to the electron's binding energy in the sample.[27–29] As unoccupied states naturally have no electrons to emit, UPS cannot be used to obtain the EA. Instead, inverse photoemission spectroscopy (IPES) is used to measure the EA, in which a collimated electron beam directed at a sample deposits electrons into high energy unoccupied states which then radiatively decay to the low energy unoccupied states, and the energy of the photons emitted from the decay process are detected.[30] Unfortunately, the limited availability of the equipment for IPES precludes widespread use of the technique, and the EA must be estimated with other methods.

Linear correlations between ionization energies and electrochemical reduction and oxidation potentials were found in earlier studies of organic compounds.[31–34] Electrochemical properties of polymers are investigated using a technique known as cyclic voltammetry (CV), in which forward and reverse linear potential scans are applied to a working electrode which measures the current from a redox-active analyte in the system.[35] The polymer is drop-casted from solution onto the surface of the working electrode, which is then submerged in a non-aqueous solution of supporting electrolyte. As the system is scanned to low potentials, the working electrodes detects a cathodic current (charges flow *out* of the electrode) as the redox-active species (the polymer) is reduced below its reduction potential. As the potential is swept up to higher potentials on the reverse scan, the working electrode detects an anodic current (charges flow *into* the electrode) as the polymer is oxidized above its oxidation potential.[36] The potential of the ferrocenium/ferrocene (Fc^+/Fc) couple is used as an internal standard to reference the

potentials in non-aqueous systems, which is itself evaluated against a common reference electrode for standardization.[37–39]

Numerous complications characteristic to the electrochemistry of semiconducting polymers precludes the measurement of standard (formal) potentials of these systems. The polymer analyte is confined to the surface of the working electrode as a solid film rather than as a solubilized freely-diffusing species, resulting in non-Nernstian electron transfer kinetics. This leads to peak-broadening and scan-rate dependent peak potentials. Additionally, the de-doping reaction is not simply the reverse of the doping reaction in polymer semiconductor films (which was well explored by Visy *et. al*).[40,41] The polymer undergoes conformational reorganization as it is charged during the doping process, which modifies the energy levels of the polymer. Penetration of the electrolyte into the polymer film ('swelling') is expected, and the interactions of the electrolyte ions and solvent molecules with the doped/undoped segments of the polymer influences the observed redox potentials. Therefore, the oxidation and reduction potentials of semiconducting polymers are evaluated using the *onset* potentials observed in the first potential sweep, where presumably the injection of charges into the HOMO/LUMO of the neutral polymer occurs and is indicated by the rise in anodic or cathodic current.

To convert solution-based electrochemical potentials to gas-phase ionization potentials, a correction factor must be used to account for both the solid-state polarization energy and to relate the potential of a reference electrode to vacuum scale.[42,43] Inconsistencies in the use of internal standards, standard electrode potential scales, and discrepancies in correlating electrode potentials to the Fermi scale make it difficult to determine the precision of such conversion factors.[42,44] Given these uncertainties, the onset

potentials of a polymer, detailed electrochemical experimental conditions, and the specific conversion factors used should be reported to simplify the comparison of reported values in the literature.

1.1.3 Charge Transport in Organic Semiconductors

The rate of charge transfer is mainly determined by two key parameters; the transfer integral and the reorganization energy.[45–48] The transfer integral (*t*) is related to the strength of the electronic coupling between two adjacent molecular entities, and describes the ease of charge transfer between these two entities in a given direction.[13] In highly crystalline structures at low temperatures (structures maximizing charge delocalization), charge transport is similar to that seen in inorganic semiconductors and is described as being in the band-like regime where the bandwidths of the HOMO and LUMO levels of interacting polymer chains determine charge mobilities. At higher temperatures (e.g. room temperature, where thermal energy is ~2.5 kJ/mol), localization of charge carriers occurs as the bandwidths are decreased due to phonon-scattering processes which in turn decreases charge mobilities. Charge transport in room-temperature polymer semiconductors involves the intra- and inter-chain hopping of charge carriers (known as the 'hopping regime'). Most simply, a charge carried by a radical ion transfers to a neighboring neutral molecule, itself becoming oxidized (in the case of electron transfer) to the neutral state while the other molecule is reduced.[49] As each molecule is now in a new electronic state, changes in equilibrium geometry occur due to the different bonding arrangements (Figure 1-7).

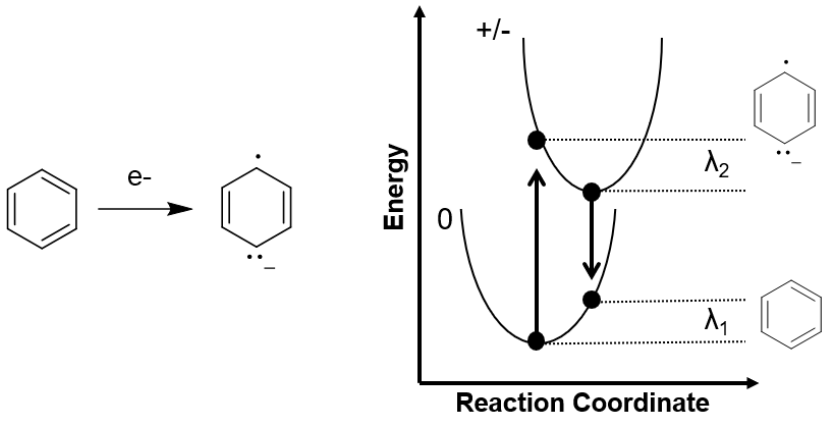

Figure 1-7 Schematic Representation of the potential energy surfaces of the initial and final state upon charge transfer, with relevant internal reorganization energies noted.

The reorganization energy is the energy required to 'reorganize' the molecular system upon charge transfer. This includes not only the 'internal' reorganization energy of geometry changes within the molecule itself, but also the 'external' reorganization energy of the surrounding medium as it polarizes/relaxes to accommodate the new charge (or lack thereof).

The rate of charge hopping (k_{ET}) is derived from Marcus theory[49], and can be described as shown in Equation 2 where T is the temperature, λ is the reorganization energy (see Figure 1-7), *t* is the transfer integral, and *h* and k_B are the Planck and Boltzmann constants respectively. It can be seen from Equation 2 that charge transfer is a thermally-activated process, and that maximizing the transfer integral and minimizing the reorganization energy upon charge transfer are key to increasing the rate of charge transport.

$$k_{ET} = \frac{4\pi^2}{h}\frac{1}{\sqrt{4\pi t k_B T}}t^2 exp\left(-\frac{\lambda}{4k_B T}\right) \quad (2)$$

1.2 Organic Field Effect Transistors

1.2.1 Components and Structures of Organic Field Effect Transistors

Organic field-effect transistors are basic circuitry elements that allow measurements of field effect mobility via the application of an applied gate voltage that is capacitively coupled to the polymer semiconductor. OFET devices are comprised of layers of materials assembled on a substrate: the gate, source, and drain electrodes, the gate dielectric, and the semiconductor. The four types of device architectures are shown in Figure 1-8: bottom gate bottom contact (BGBC- Figure 1-8a), top gate bottom contact (TGBC- Figure 1-8b), top gate top contact (TGTC-Figure 1-8c), and bottom gate top contact (BGTC-Figure 1-8e).

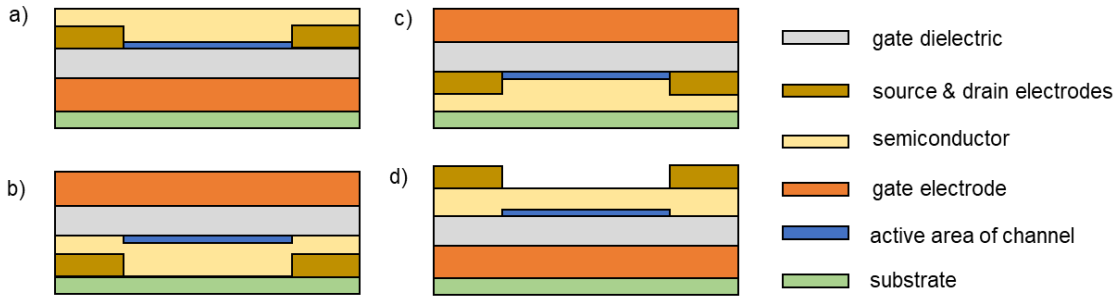

Figure 1-8 OFET device architectures. a) bottom gate bottom contact b) top gate bottom contact c) top gate top contact e) bottom gate top contact

BGTC and TGBC devices have 'staggered' geometries, in which the active areas of the conductive channels are offset from the source and drain contacts. Conversely, BGBC and TGTC structures are 'coplanar' as these active areas are between the source and drain contacts. The staggered geometries generally exhibit lower contact resistance due to the extended injection area (gap between the gate electrode and contacts) which can also vary charge carrier injection dynamics.[50,51] Top-gate electrodes can act as encapsulation layers and reduce environmental degradation due to water and oxygen in devices they are

incorporated into, however the integrity of the semiconductor may be compromised during deposition. Likewise, the semiconductor integrity can be compromised during the deposition of source/drain contacts in BGTC structures.[52] BGBC structures, though exposed, have the advantage of maintaining pristine semiconductor/dielectric interfaces as semiconductor deposition is the final step in device fabrication. Device geometries must be noted when comparing reports of OFET performance.

The gate electrode is commonly a metal or doped semiconductor, which is covered with an insulating dielectric such as an inorganic oxide layer (e.g. SiO_2) or an insulating polymer (e.g. poly(methylmethacrylate)). The dielectric layer has a profound impact on device performance not only for its capacitance but also for its effect on the dynamics of the semiconductor-dielectric interface where the active area of the channel resides (which is at most only a few nanometers wide).[53] The surface energy and roughness of the dielectric influences the morphology of the deposited semiconductor films and the trap density at the interface, both of which have extensive implications for charge transport. Inorganic oxides in particular are plagued with high trap densities due to characteristically rough surfaces and terminal hydroxyl groups which serve as charge traps upon reduction by charge carriers. Surface modification of SiO_2 gate dielectrics through the introduction of organosilane self-assembled monolayers (SAMs) is a common approach to passivating these charge traps and adjusting the physical properties of the dielectric surface.[54]

The source and drain electrodes are typically high work function metallic contacts (e.g. gold) which can be vapor-deposited through a shadow mask or painted/printed on with conductive inks. The organic semiconductor layer (~50 nm thick) can be vapor-

deposited (if small molecules) or processed from solution (spin-coating, blade-coating, ink-jet printing, etc).

1.2.2 Organic Field Effect Transistor Operation and Characterization

The operation of an OFET is dependent on the application of two potentials as shown in Figure 1-9; the voltage applied between the source and drain electrodes known as the source-drain voltage, V_D, and that applied to the gate electrode known as V_G. The semiconductor and gate electrode are capacitively coupled so that an applied gate bias induces charge carrier accumulation at the semiconductor/dielectric interface; this "turns on" the transistor through the 'field effect'.

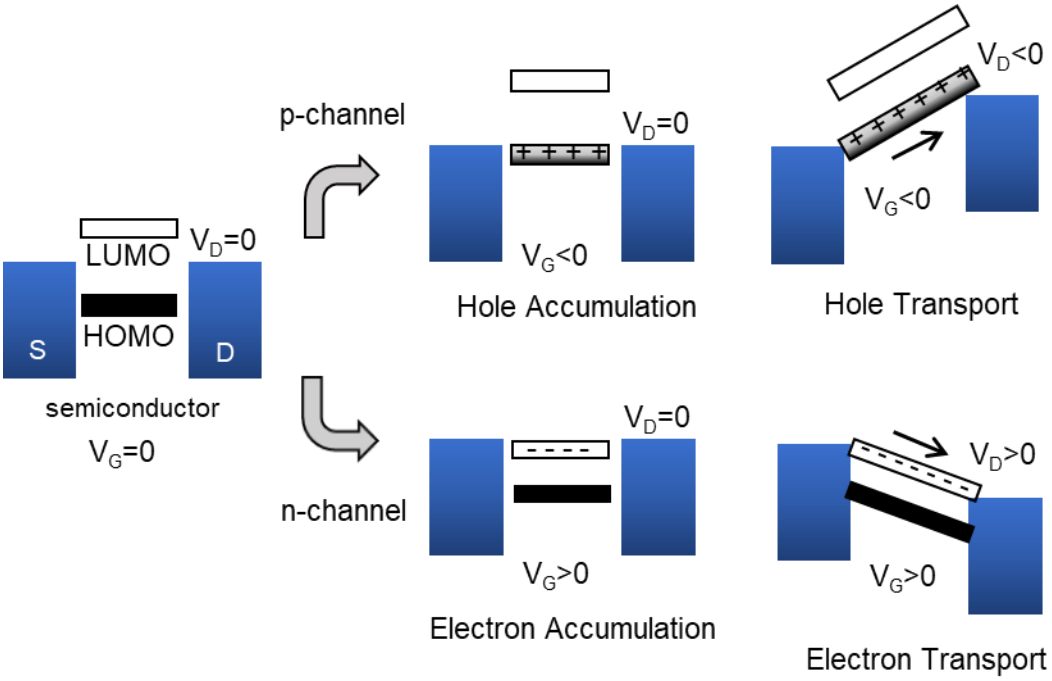

Figure 1-9 Simplified energy level depiction of an OFET at various applications of V_D and V_G. Adapted from reference.[55]

The HOMO and LUMO levels in the semiconductor shift to higher energies relative to the Fermi levels of the metal contacts (which are externally controlled) in response to a negative applied V_G in a p-channel device (all opposite for n-channel).[55] When V_G is large enough, the FMOs of the semiconductor become resonant with the Fermi levels of the contacts which allows charge carriers to flow between them. When there is no applied V_G, there is no charge accumulation and the transistor is "off". Most of the induced charge carriers are mobile and move in response to an applied V_D, resulting in a current between the source and drain contacts (I_{SD}). In a real device, a small V_G is required to first fill the charge traps present at the semiconductor/dielectric interface before mobile charge carriers can accumulate. This trap-filling voltage is known as the threshold voltage, V_T.

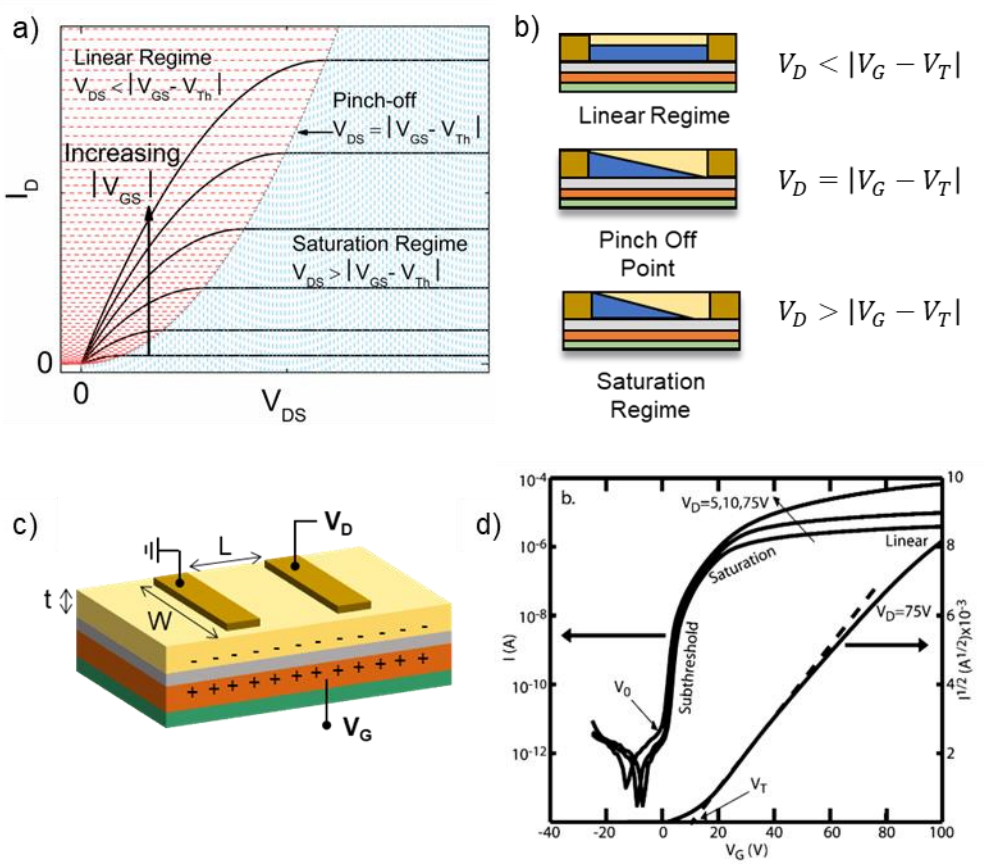

Figure 1-10 Operation of an OFET. a) Ideal output characteristics with I_D shown on a logarithmic scale (from reference [56]) b) Evolution of carrier concentration profile in an OFET c) schematic of BGTC OFET with relevant voltages and geometric variables d) Example transfer curves shown on semi-logarithmic axes (from reference [55]).

The evolution of I_D with an increasing V_D and constant V_G is shown in Figure 1-10a. OFET measurements under these conditions are known as *output characteristics*. When $V_D < |V_G - V_T|$, the device is in the *linear regime* (red shaded region, Figure 1-10a) where I_D increases linearly with V_D. As V_D approaches $|V_G - V_T|$, the space around the drain electrode is depleted of charge carriers and is 'pinched off' (Figure 1-101-10b). As V_D increases this depletion zone increases as well and the current I_D becomes saturated; hence, where $V_D > |V_G - V_T|$ is considered the *saturation regime* (blue shaded region, Figure 1-10a).

Conversely, for a given constant V_D the magnitude of I_{SD} is a function of V_G, as shown in Figure 1-10d. OFET measurements under these conditions are known as *transfer characteristics*, and key OFET performance values are extracted from these measurements. The expression for I_D in the linear regime is shown in equation 3:

$$I_{D,lin} = \frac{W}{L} C_{ox} \mu \left[(V_G - V_T) V_D - \frac{V_D^2}{2} \right] \quad (3)$$

Where *W* and *L* are the length and width of the channel (see Figure 1-10c), C_{ox} the capacitance of the dielectric per unit area (in units of nF/cm^2), and μ is the carrier mobility (i.e. the velocity per unit electric field, expressed in units of $cm^2V^{-1}s^{-1}$). The mobility in the linear regime is extracted from the slope of the I_D-V_D curve. The expression for I_D in the saturation regime is shown in equation 4:

$$I_{D,sat} = \frac{W}{2L} C_{ox} \mu (V_G - V_T)^2 \quad (4)$$

Where the device mobility can be derived from the slope of $I_{D,sat}^{1/2}$ vs. V_G (Figure 1-10d, right axis). The threshold voltage of the device is taken as the y-intercept of the linear extrapolation of the $I_{D,sat}^{1/2}$ vs. V_G slope. A large on/off current ratio, $I_{on/off}$ (reported as 10^x), is required so the 'on' and 'off' states are clearly distinguishable.

The charge-carrier mobility (μ), the threshold voltage (V_T), and current ratio ($I_{on/off}$) are the figures of merit most commonly used to evaluate OFET device performance. While these performance characteristics can be modified through careful selection and design of the semiconductor material it is imperative to recognize that these

metrics are properties of the device itself, and do not directly reflect any intrinsic properties of the semiconductor material. Device performance is dependent on the device geometry, processing, operating conditions, current detection limits of the measurement apparatus, and the integrity of the mobility extraction procedures.[57–65] For OFETs to compete directly with the entrenched a-Si-H devices, they need meet the same performance standards; including $\mu \geq 1$ $cm^2V^{-1}s^{-1}$ and $I_{on/off} \geq 10^6$ at a maximum operating voltage of 15 V (or less).[66] Ideally, OFETs should not have large voltage shifts and should be stable after prolonged exposure to ambient conditions.[67]

1.3 Charge Transport Materials for Organic Field Effect Transistors

Many D-A polymers have shown high charge carrier mobilities, however the nature of the D-A design strategy produces narrow bandgap copolymers with high HOMOs and low LUMOs, resulting in ambipolar charge transport behaviour in OFETs. Ambipolar semiconductors are attractive as they can greatly simplify the fabrication process of complementary metal-oxide semiconductor (CMOS)-like complimentary circuits. Unfortunately, the low on/off ratios and high off currents characteristic to ambipolar devices greatly increases their power consumption.[68]

1.3.1 The N-Channel Challenge

Significant progress has been made in improving the performance of p-channel devices, however the performance of n-channel devices lags far behind.[61] To enable the fabrication of CMOS-like complimentary circuits, both p- and n-channel devices of comparable performance are required, and improving the performance of n-channel OFETs remains a key challenge in the field. Theoretical studies have shown electrons and holes to

have similar (though not identical) reorganization energies and transfer integrals in most organic semiconductors; hence it cannot be said that electrons are inherently less mobile than holes in these systems.[48] The extent to which n-channel or p-channel transport behaviour dominates is a factor of not only of the intrinsic properties of the semiconductor itself but also of the device architecture. The following will discuss factors for poor n-channel device performance relative to that of p-channel devices and the challenges this presents to polymer semiconductor design.

1.3.1.1 Semiconductor Stability

During device operation, the polymer semiconductor in an n-channel OFET is effectively 'doped' with electrons injected from the source electrode. These organic radical anions are unstable and are easily oxidized upon contact with water or oxygen, meaning n-channel devices cannot be operated in ambient atmosphere. D.M. de Leeuw et. al. first highlighted the inherent redox instabilities that had been observed in n-doped conjugated polymer semiconductors and stated that an anionic polymer should have an oxidation potential greater than +0.571 V (vs. SCE) to be stable towards both water and oxygen (as calculated for pH of 7 and neglecting any overpotentials).[69] Operational OFET stabilities of anthracene derivatives was investigated by Wang *et. al.*, in which they found a material having a reduction potential between -0.6 - -0.4 V (vs. SCE) would have stable n-channel performance.[70] After a decade of research on organic semiconductors for n-channel devices, the reduction potential of -0.4 V (vs SCE) (or an EA of -4.0 eV vs. vacuum) remains the benchmark to expect a given semiconductor to have ambient operational stability.[71] This presents quite a challenge to synthetic chemists to design increasingly electron deficient moieties.

1.3.1.2 Charge Carrier Trapping at the Semiconductor/Dielectric Interface

The silanol (-SiOH) moieties on SiO_2 dielectric surfaces effectively serve as electron traps that inhibit charge transport.[72,73] Upon electron trapping, $-SiO^-$ is formed on the SiO_2 surface. The exact mechanisms of electron trapping are disputed, but are thought to be a dynamic of electrochemical interactions between the charge carriers, the surface silanols on the SiO_2 dielectrics and trace amounts of H_2O and O_2 adsorbed onto the dielectric surface.[74,75] The substrates of n-channel OFETs have also been found to become more negatively charged after being stressed at positive gate biases.[76,77] The formation of $-SiO^-$ upon electron trapping not only increases the electron injection barrier (resulting in a decrease of electron current), but also increases the V_T for hole accumulation while reducing V_T for electron accumulation causing both to positively shift in the transfer curves.[76] In this way, the electron current is simultaneously suppressed while hole current is increased.[73] Surface treatment of SiO_2 dielectrics with SAMs to 'passivate' the surface is necessary for n-channel operation.[52,54,78,79] However, it should be noted that the self-assembled organosilanes commonly used to passivate SiO_2 has been shown to incompletely cover the surfaces, meaning free silanol groups are indeed still present on 'passivated' surfaces.[80] While SAMs can alleviate the e- trapping, trace amounts of water can be trapped in films and at the surface of the insulator/semiconductor interface which cannot be completely removed under vacuum. Blom *et. al.* even reported the presence of bishydrated oxygen complexes as common electron traps in single-carrier diodes that had been fabricated in an N_2-filled glovebox and tested under vacuum.[81] These reports highlight the practical limitations on experimental conditions that have plagued the pursuit of n-

channel OFET devices, and which should always be considered in evaluating the performance of these devices.

1.3.1.3 Contact Resistance and Charge Carrier Injection

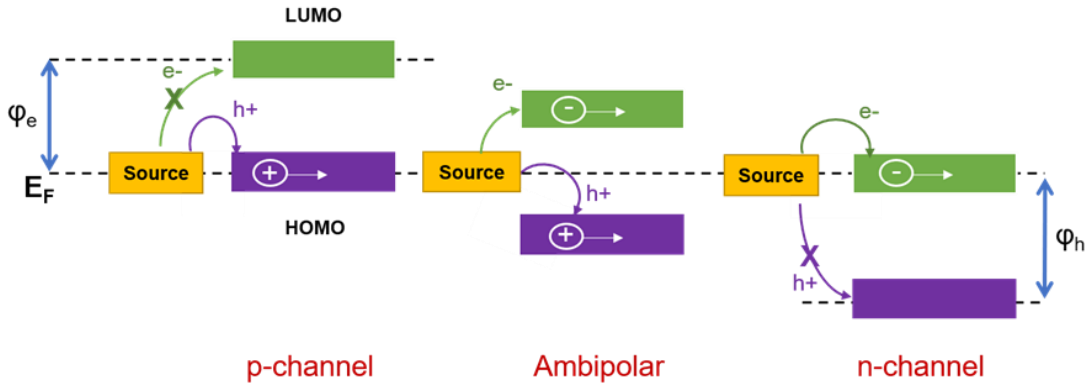

Figure 1-11 Energy level alignment of source electrode with semiconductor FMOs. Adapted from reference.[82]

In addition to electrochemical stability, the low frontier energy levels of polymer semiconductors for n-channel OFETs presents challenges in efficient electron injection.[59,83,84] As shown in Figure 1-11, energetic alignment of the frontier energy levels of the polymer semiconductor with the fermi energy of the source electrode impacts the majority charge carrier injected into the device.[85] Ohmic contacts are expected when the work function of the source electrode is aligned with a FMO of the semiconductor within a few tenths of an eV.[86–88] Larger misalignments lead to non-ohmic contacts with the formation of potential barriers at the electrode/semiconductor interface, resulting in poor charge injection and increased contact resistance.[50,59] The electron injection barrier height, φ_e, is decreased as the LUMO energy of the semiconductor is lowered to be more closely aligned with the Fermi energy of the source electrode material. The low work-function electrodes amenable to efficient electron injection into most semiconducting polymers

(such as Al, Ba, and Ca)[85,89] are themselves prone to rapid oxidation in ambient atmosphere, presenting prohibitive difficulties in device fabrication. For this reason, Au electrodes with a Fermi energy of -5.1 eV are the most commonly used electrodes in n-channel devices despite being more favourable for hole injection.[85]

CHAPTER 2. SYNERGISTIC USE OF BITHIAZOLE AND PYRIDINYL SUBSTITUTION FOR EFFECTIVE ELECTRON TRANSPORT MATERIALS

2.1 Introduction[1]

The prevailing donor-acceptor (D-A) design motif has led to significant advances in polymer semiconductor performance as it allows for the fine-tuning of frontier molecular orbitals for efficient charge injection in addition to promoting strong intermolecular π-π stacking interactions that facilitate charge transport.[82,90] This design strategy, however, has proven to be of limited use in developing n-channel conjugated polymers because there are relatively few building blocks with sufficient electron deficiency to achieve an electron affinity higher than +4 eV (*i.e.*, roughly speaking, a lowest unoccupied molecular orbital (LUMO) energy below -4 eV) for facile electron injection and operational stability of resultant polymers. In addition, the decrease in ionization potential and electron affinity (destabilization of the highest-occupied molecular orbital (HOMO) and LUMO energy levels) upon incorporation of a donor unit often leads to ambipolar behavior in OFET devices (Figure 2-1), which can lead to unbalanced hole/electron mobilities, undesirable leakage currents and small current on/off ratios (I_{ON}/I_{OFF}).[45,91–96]

[1] Reproduced in part with permission from *Chemistry of Materials*, submitted for publication. Unpublished work copyright 2019 American Chemical Society.

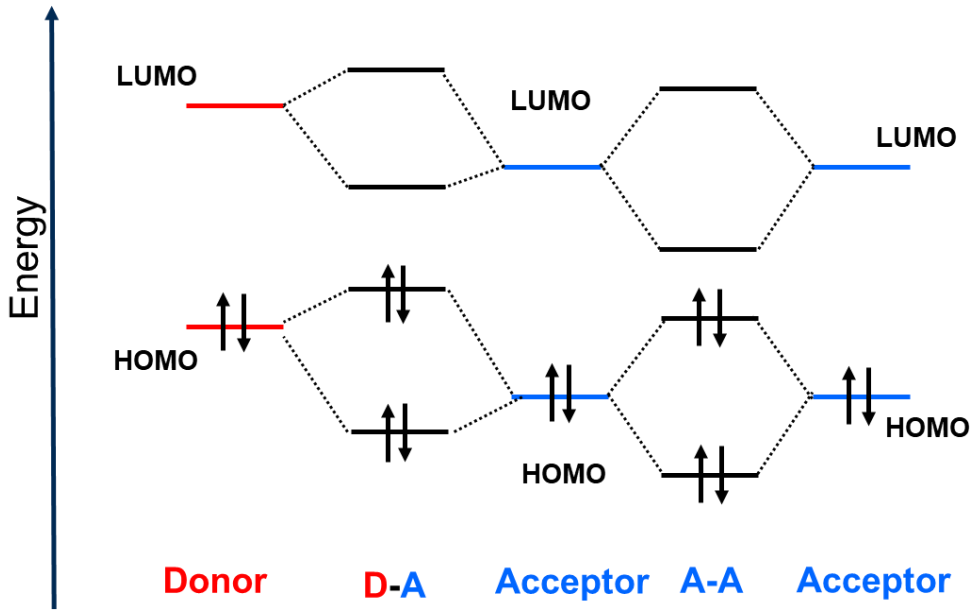

Figure 2-1 Depiction of the reasoning behind donor-acceptor and all-acceptor molecular design strategies. Note the destabilizing effect of the donor moiety in the D-A copolymer.

The use of all-acceptor (A-A) polymers to minimize intramolecular charge transfer and preserve polymer low lying frontier molecular orbitals (FMOs) has been demonstrated to successfully result in unipolar n-channel materials upon incorporation into conventional transistor devices.[97–103] Performance improvements were observed because the increased electron affinity facilitated electron injection and the increased ionization potentials diminished hole accumulation. While the synthesis of many acceptor units poses difficulties, the pursuit of high-performance A-A polymers is challenged further by the relative steric bulk of common electron-deficient moieties (e.g. perylenediimides, naphthalenediimides, etc). For instance, steric effects can lead to twisted polymer backbones, which negatively impacts molecular packing in thin films and adversely affects charge transport.[94,95,104] While the introduction of a "spacer" unit such as 2,2'-bithiophene (BT) has produced high performance n-channel polymer semiconductors,[105–107] the

electron-rich nature of the thiophene units can also reduce the ionization potential (destabilize the HOMO) and lead to ambipolar behavior.[99]

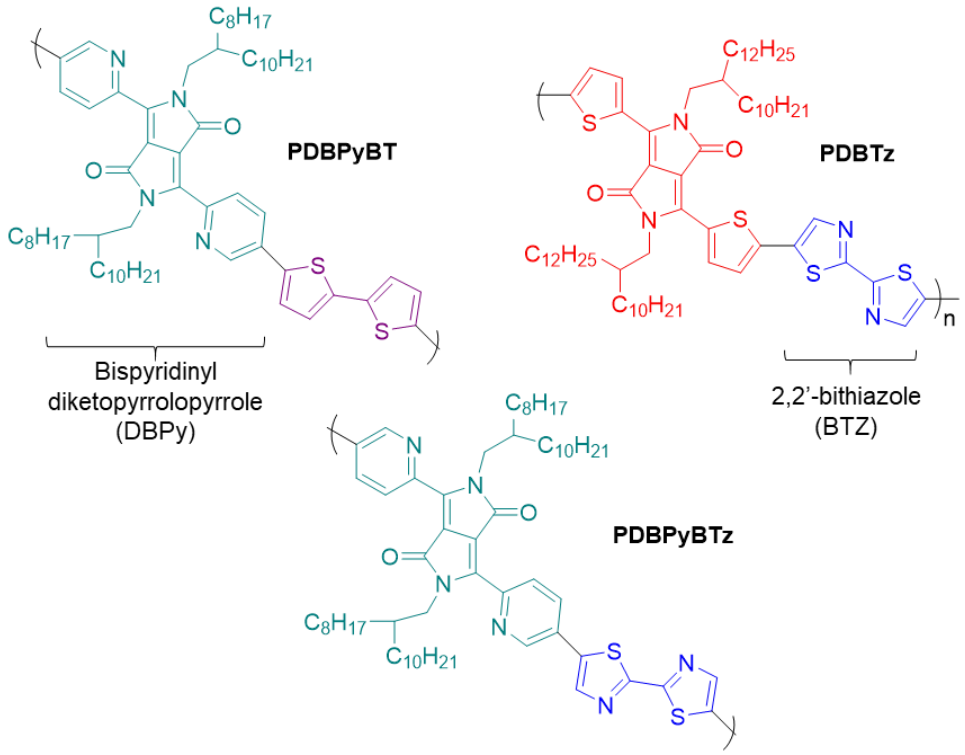

Figure 2-2 Structures of PDBPyBT, PDBTz, and PDBPyBTz copolymers

Sun. *et. al.* introduced a high-performance ambipolar material based on a pyridine-flanked diketopyrrolopyrrole (DBPy) unit as an acceptor and BT as a donor, which exhibited electron and hole-mobilities of 6.3 $cm^2V^{-1}s^{-1}$ and 2.78 $cm^2V^{-1}s^{-1}$, respectively (structure shown in Figure 2-2).[106] Similarly, ambipolar behavior was observed in a copolymer of DBPy and electron-donating thieno[3,2-*b*]thiophene with a reported mobility of 3.36 $cm^2V^{-1}s^{-1}$ for holes and 2.65 $cm^2V^{-1}s^{-1}$ for electrons.[108] Unipolar n-channel behavior was observed when hole-injection was suppressed with polyethyleneimine (PEI)-modified Au electrodes.[108] Interestingly, Mueller *et. al.* reported more pronounced n-channel behavior in pyridine-flanked DPP polymers upon fluorination of a thiophene

comonomer.[109] Six-membered rings flanking the DPP, diketopyrrolopyrrole, are generally more electron-deficient than five-membered ring alternatives as the six π-electrons are delocalized over a larger ring. The DBPy unit is especially attractive for use in n-channel polymers since the pyridine electronegative nitrogen atom not only serves to lower the FMOs *vs*. phenyl rings, but also relieves steric interactions between the lactam oxygen atoms and the α-hydrogen atoms present in diphenyl-DPPs.[110] Our quantum-chemical calculations corroborate the previously reported 0° dihedral angle seen between the pyridine and the DPP core (*vide infra*), making the DBPy unit completely planar.[106] The high electron mobilities seen in DBPy–based ambipolar polymeric semiconductors suggest that the pyridine substituted moiety may be a promising acceptor for incorporation into A-A copolymers.

A viable second acceptor unit, namely 2,2'-bithiazole (BTz), might be considered as an effective comonomer (structure shown in Figure 2-2). In contrast to the more commonly used BT, BTz is more electron-deficient due to the presence of an electronegative nitrogen atom within the five-membered ring that serves to increase the electron affinity.[111] The interaction between the nitrogen lone pairs and antibonding orbitals in the adjacent thiazole rings facilitate 'locking' the BTz unit into a planar conformation,[111] in contrast to the BT analog that exhibits a dihedral angle of ~30°.[112] Recently, we developed a synthetic strategy for the facile incorporation of BTz into conjugated polymers, and further demonstrated that the replacement of BT with BTz increases the electron affinity of the resultant polymer thereby promoting n-channel charge transfer characteristics as determined by OFET performance.[113] The BTz and thiophene-flanked DPP D-A copolymer exhibited an electron mobility of 0.3 $cm^2V^{-1}s^{-1}$ in top-

contact/bottom gate (TCBG) OFET devices.[113] Subsequently, BTz was polymerized with DPP to afford a dithiazole-DPP A-A copolymer having a unipolar field-effect mobility up to 0.067 $cm^2V^{-1}s^{-1}$ in a bottom-gate/bottom-contact (BGBC) device.[97]

This chapter describes the copolymerization of the BTz distannane monomer with a brominated DBPy to afford an all-acceptor, unipolar n-channel polymer, poly(dipyridinyldiketopyrrolopyrrole-bithiazole), PDBPyBTz, as shown in Figure 2-2). With the combination of two planar electron-deficient units, both of which had demonstrated high electron mobility in isoelectronic conjugated polymer precursors, poly(dithienyldiketopyrrolopyrrole-bithiazole) PDBTz and poly(dipyridinyldiketopyrrolopyrrole-bithiophene) PDBPyBT, the optoelectronic properties and device performance characteristics of this new 'all acceptor' polymer semiconducting material with these analogous structures are explored. The computational, photophysical, morphological and device investigations demonstrate that the all-acceptor approach with judicious choice of molecular structural moieties can lead to the design and development of effective electron transport semiconducting materials.

2.2 Experimental

2.2.1 Materials and Methods

Chloroform, dichloromethane, toluene, p-xylene, isopropanol, tetrahydrofuran (THF), dimethylformamide (DMF), chlorobenzene, and 1,2-dichlorobenzene (o-DCB) were purchases as anhydrous grade solvents from Sigma-Aldrich. THF was distilled from sodium benzophenone in a solvent purification system (SPS). 2-Bromothiazole was purchased from Scientific Matrix. Tetrabutylammonium bromide (n-Bu_4NBr), n,n-

diisopropylethylamine (DIPEA), diisopropylamine (DIPA), palladium(II) acetate ($Pd(OAC)_2$), tris(dibenzylideneacetone)-dipalladium(0) ($Pd_2(dba)_3$, tri(o-tolyl)phosphine ($P(o\text{-}tolyl)_3$), sodium diethyldithiocarbamate, and tetra-*n*butylammonium hexafluorophosphate ($[n\text{-}Bu_4N]^+[PF_6]^-$) were purchased from Sigma-Aldrich. *N*-octadecyltrichlorosilane (OTS-18) was purchased from Gelest, Inc. Silica gel was purchased from Sorbent Technologies (Premium Rf^{TM}, porosity: 60A; particle size: 40-75 μm). Molecular weights of polymer samples were determined with a Tosoh EcoSec-HT (high temperature) Gel Permeation Chromatograph (GPC) with a refractive index detector and polystyrene standards. All samples were run in 1,3,5-trichlorobenzene eluent at 135 ^oC. PDBPyBT (poly(dipyridinyldiketopyrrolopyrrole-bithiophene, "DPPDPyBT", M321) was purchased from Ossila Ltd.

The polymer thermal decomposition temperature was measured with a Perkin-Elmer Pyris-1 thermogravimetric analyzer (TGA) in a nitrogen atmosphere (25 mL/min) with a heating rate of 10 ^oC/min. Polymer thermal transitions were measured with a TA Q200 Differential Scanning Calorimeter (DSC) in a nitrogen atmosphere (50 mL/min) with a heating/cooling rate of 10 ^oC/min. Each sample was scanned for three cycles.

UV-vis absorption spectra were recorded on an Agilent 8453 UV-Visible Spectrophotometer. Polymer films for UV-vis absorption characterization were prepared by spin-coating polymer solutions in p-xylene (5 mg/mL) and chloroform (5 mg/mL) onto pristine SiO_2 glass substrates and OTS-18 pre-treated glass covered substrates. The details of OTS-18 pre-treatment are depicted in the section on "OFET Device Fabrication and Characterization". Photoluminescence (PL) spectra were taken using a continuous-wave

(CW) laser emitting 637 nm light at the maximum power of 50 mW (Coherent CUBE, USA).

PL emission from the sample was collected from an optical fiber (core diameter 600 μm) and sent to an Ocean Optics spectrometer (USB4000). Solutions were measured in glass cuvettes (1 cm x 1 cm), at a 90^{o} angle with respect to the incident excitation beam, while films were tilted at 45^{o} with respect to the beam. A 650 nm long pass filter was used to remove pump scatter from the spectra.

Cyclic voltammetry was performed in a three-electrode cell using a Princeton Applied Research 273 potentiostat/galvanostat under CorrWare control. The electrolyte was 0.5 M tetrabutylammonium hexafluorophosphate ($TBAPF_6$, Acros Organics, 98% recrystallized from hot ethanol) dissolved in propylene carbonate. A glassy carbon electrode with drop-cast polymer film (1 mg/mL solution in $CHCl_3$) was used as the working electrode. A glassy carbon rod served as the counter electrode, and an Ag/Ag^+ electrode (10 mM $AgNO_3$ and 0.5 M $TBAPF_6$ in acetonitrile, 0.085 V vs. Fc/Fc^+) was used as the reference. The experiments were performed in an inert atmosphere with scan rates of 50 mV/s.

Ultraviolet Photoemission Spectra (UPS) were measured on Kratos Axis Ultra DLD XPS/UPS system, using a He-I lamp radiation at 21.2 eV. All samples were in electronic equilibrium with the spectrometer via a metallic clip on the surface and were run at a base pressure of 10^{-9} Torr. The Fermi level was calibrated using atomically clean silver. UPS were acquired at 5 eV pass energy and 0.05 eV step size with the aperture and iris set to 55 μm. From the secondary electron edge (SEE) of the UPS we calculated the work

function (ϕ = 21.22-SEE) for each polymer, and from the emission close to the Fermi level we determine the position of the valence band maximum. IP (= -HOMO) and ϕ were calculated by equations (5) and (6):

$$IP = h\upsilon - \left(E_{cutoff} - \varepsilon_V^F\right) \quad (5)$$

$$\phi = h\vartheta - E_{cutoff} \quad (6)$$

Where $h\upsilon$, E_{cutoff}, and ε_V^F denote the incident photon energy (HE I, 21.22 eV), the high binding energy cutoff, and the lowest binding energy point, respectively.

The surface morphologies of PDBPyBTz films were characterized by Atomic Force Microscopy (AFM) using a Bruker Dimension Icon Atomic Force Microscope System with ScanAsyst in the tapping mode using a silicon etched probe tip (Mikromasch USA, HQ:NSC14/NO AL). Polymer films for AFM characterization were prepared by spin-coating polymer solutions in chloroform (4 mg/mL) and p-xylene (4 mg/mL) onto OTS-18 pre-treated SiO_2 dielectric (300 nm) / p++ doped Si substrates.

2D-GIWAXS characterization was carried out using beamline 11-3 at the Stanford synchrotron radiation light source (SSRL). The beam was kept at an energy of 12.7 keV, with the incident angle controlled at 0.13-0.14°. WxDiff software was used for reducing the 2D scattering maps into 1D intensity vs. q-spacing plots. Polymer film orientation distribution was investigated by Herman's orientation function (*S*), as shown in Equation (7) and (8):

$$f = \frac{\int_0^{\pi/2} I(\chi) cos^2(\chi) \sin(\chi)\, d\chi}{\int_0^{\pi/2} I(\chi) \sin(\chi)\, d\chi} \quad (7)$$

$$S = \frac{1}{2}(3f - 1) \quad (8)$$

To simplify the calculations, χ was defined as 0^o at the q_z axis (out-of-plane), and as 90^o at the q_{xy} axis (in-plane). The $I(\chi)$ term is the <100> or <010> intensity at each χ, and $\sin(\chi)$ represents a geometric intensity correction factor. The molecular orientation parameter, *f*, refers to the average lattice plane orientation relative to χ_{max}, the azimuthal angle at which $I(\chi)$ approaches the maximum. According to equation (4), S =1, if on average, the lattice planes completely align parallel to χ_{max}; S = -1/2 if they completely orient perpendicular to χ_{max}; while S = 0 if the lattice planes orient randomly.

BCBG OFETs were fabricated on a heavily *p*-doped silicon wafer <100> as the gate electrode with a 300 nm thick layer of thermally grown SiO_2 as the gate dielectric. Au source and drain contacts (50 nm of Au with 3 nm of Cr as the adhesion layer) with fixed channel dimensions (50 μm in length and 2 mm in width) were deposited via E-beam using a photolithography lift-off process. Prior to deposition of polymer semiconductors, the devices were cleaned in acetone for 30 minutes and subsequently rinsed with acetone, methanol, and isopropanol in sequence. The SiO_2 surface was pretreated by UV/ozone for 30 minutes followed by immersion into a 2.54 x 10^{-3} M (1 μL/mL) solution of OTS-18 in anhydrous toluene. The devices were then cleaned by sonication in toluene for 10 minutes, followed by rinsing sequentially with acetone, methanol, and isopropanol, and drying under a flow of N_2. The H_2O contact angle for the SiO_2 surface after OTS-18 treatment was

in the range of 95-105°; the OTS-18 modified SiO_2 dielectric has a capacitance of 1.1 x 10^{-4} Fm^{-2}. Polymer solutions (10 mg/ml) were then blade coated onto substrates or spin-coated (90 s, 1500 rpm) under ambient conditions. The capacitances of the dielectric layers were measured using an Agilent 4284A Precision LCR Meter. All OFET characterizations were performed using a probe station inside a nitrogen filled glovebox using an Agilent 4155C semiconductor parameter. The FET mobilities were calculated from the saturation regime in the transfer plots of V_G versus I_{SD} by extracting the slope of the linear range of V_G vs. $I_{SD}^{1/2}$ plot and using equation 9:

$$\frac{\delta I_{SD}^{1/2}}{\delta V_G} = (\mu_e C_{ox} \frac{W}{2L})^{1/2} \quad (9)$$

Where I_{SD} and V_{SD} are the source-drain current (A) and source-drain voltage (V), respectively; V_G is the gate voltage (V) scanning from -20 to 80 V (for BGBC OFETs) in the transfer plot; C_{ox} is the capacitance per unit area of the gate dielectric layer. W and L refer to the channel length and width; μ_e represents the electron field-effect mobility in the saturation regime ($cm^2V^{-1}s^{-1}$). In this study, the threshold voltage, V_T, was calculated by extrapolating $V_T = V_G$ at $I_{SD} = 0$ in the V_G vs. $I_{SD}^{1/2}$ curve. The current on/off ratio, $I_{on/off}$, was determined through dividing maximum I_{SD} (I_{ON}) by the minimum I_{SD} at about V_G in the range of -20 to 0 V (I_{OFF}). It was noted that PDBPyBTz field-effect mobility was more stable and hysteresis was reduced after thermal annealing at 150 °C for 90 minutes in OFETs and no obvious improvement was observed at annealing temperatures above 150 °C.

The microwave irradiated polymerizations were conducted using a CEM Discover SP System. ^{1}H and ^{13}C NMR spectra were recorded using a Varian Mercury Vx 300 nuclear magnetic resonance spectrometer or Bruker Avance IIIHD 700 nuclear magnetic resonance spectrometer. The complete synthetic route to PDBPyBTz is shown in Figure 2-3. Associated NMR spectra can be found in the appendix.

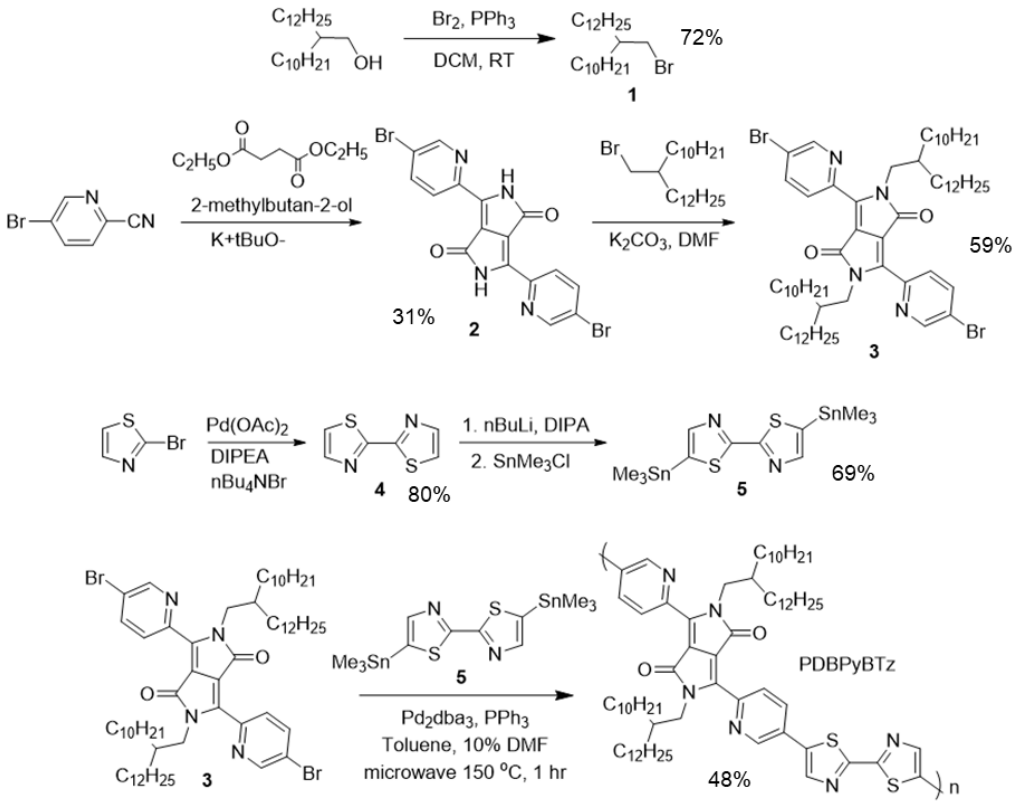

Figure 2-3 Synthetic Route to PDBPyBTz

2.2.1.1 Synthesis of 11-(bromomethyl)tricosane (**1**)

PPh_3 (6.6 g, 25.1 mmol) was added to a 100 mL round bottom flask equipped with a stir bar and addition funnel, which was then degassed/refilled with N_2 three times. 15 mL of anhydrous dichloromethane (DCM) was then transferred to the flask to dissolve the

PPh_3. The reaction flask was then placed in an ice-bath. When the reaction mix was at 0 ^oC, Br_2 (1.1 mL, 21.4 mmol) was then added drop-wise via the addition funnel, turning the solution from yellow to orange. 2-Decyl-1-tetradecanol (10 g, 28.1 mmol) was then added dropwise to the reaction mix, followed by an additional 4 mL of DCM. The reaction mix was then allowed to reach room temperature and stirred overnight. The solvents were then removed, and the product extracted with hexanes and purified via column chromatography (silica gel, hexanes eluent) to yield 8.5 g of colorless transparent oil (72% yield). ^1H NMR (300 MHz, $CDCl_3$): δ 3.45 (d, J = 3.4 Hz, 2H), 1.59 (m, 1H), 1.27 (m, 40 H), 0.88 (m, 6H). NMR agreed with that reported by Guo *et. al.*[114]

2.2.1.2 Synthesis of PyDPP (**2**)

5-Bromopyridine-2-carbonitrile (6.19 g, 34 mmol), diethyl succinate (2.61 g, 15 mmol), and 2-methylbutan-ol (70 mL) were added to an oven-dried round bottom flask equipped with a condenser and stirred at room temperature. Oven-dried potassium t-butoxide (4.14 g, 37 mmol) was then added all at once, at room temperature. The reaction was heated to 100 ^oC and allowed to stir overnight. The reaction mixture was then allowed to reach room temperature, and precipitated in MeOH followed by filtration to yield 2.08 g of insoluble red solid (31% crude yield). The insoluble product was used in the next step without characterization.[106]

2.2.1.3 Synthesis of PyDPP-Al (**3**)

PyDPP (**2**) (500 mg, 1.1 mmol) and potassium carbonate (400 mg, 2.9 mmol) were combined in a round bottom flask which was placed under N_2. Anhydrous dimethylformamide (DMF) was then added via cannula. The mixture was stirred at 90 ^oC

for 30 minutes to dissolve, where the reaction mixture turned from red to dark blue. 1-bromo-2-octyldodecane (**1**, 1.15 g, 2.7 mmol) was then added via syringe then heated to 130 ^{o}C, turning from blue to maroon within a minute of adding the alkyl bromide. The reaction was closely monitored via TLC for disappearance of starting material, then allowed to cool to room temperature after 1 hour. The reaction mixture was diluted with ethyl acetate (EtOAc) and washed with brine (9 x 20 mL) to remove DMF, then the solvent was rotovapped from the combined organic fractions. The product was then purified via column chromatography (silica gel, toluene eluent) to give 0.660 g of an oily maroon solid (59% yield). ^{1}H NMR (300 MHz, $CDCl_3$) δ 8.94 (d, J = 8.6 Hz, 2H), 8.74 (d, J = 2.4 Hz, 2H), 8.01 (dd, J = 8.6 Hz, 2H), 4.28 (d, J = 7.3 Hz, 4H), 1.60 (s, 2H), 1.20 (s, 90 H), 0.87 (t, J = 8.5 Hz, 17H). ^{13}C NMR (400 MHz, $CDCl_3$) δ 162.47, 150.09, 146.05, 144.96, 139.69, 128.34, 122.45, 111.42, 45.29, 38.21, 31.93, 31.90, 31.44, 30.01, 30.00, 29.68, 29.66, 29.62, 29.56, 29.37, 29.33, 26.37, 22.69, 22.68,14.13, 14.12. Overlapping of alkyl peaks in ^{13}C NMR spectra. Both NMR spectra are in agreement with previous reports.[106,115,116] Please see Figure A-2 and Figure A-3 in Appendix for spectra.

2.2.1.4 Synthesis of 2,2'-Bithiazole (**4**)

Freshly distilled diisopropylethylamine (DIPEA, 2.13 mL, 12.20 mmol), 2-bromothiazole (2.00 g, 12.20 mmol), tetra-n-butylammonium bromide (1.97 g, 6.1 mmol), and palladium(II) acetate ($Pd[OAc]_2$, 0.14 g, 0.61 mmol) were dissolved in anhydrous toluene (30 mL) under N_2, and refluxed at 120 ^{o}C overnight. The reaction mixture was then allowed to reach room temperature before extraction into dichloromethane, and the combined organic fractions washed with brine and dried over $MgSO_4$. The solvent was removed leaving a brown oil which was purified via column chromatography (silica gel,

dichloromethane eluent). Yellow solid was collected (0.82 g), which was recrystallized in heptanes to produce an off-white crystalline solid (yield 80%).[113] ^{1}H NMR ($CDCl_3$, 300 MHz) δ 7.91 (d, J = 7.80 Hz, 2H), 7.45 (d, J = 7.45 Hz, 2H). Please see Figure A-4 in Appendix for spectrum.

2.2.1.5 Synthesis of 5,5'-Bis(trimethylstannyl)-2,2'-bithiazole (**5**)

Freshly distilled diisopropylamine (DIPA, 0.6 mL, 4.27 mmol) in anhydrous THF (2 mL) under N_2 was cooled to -78 ^{o}C, followed by dropwise addition of n-butyl lithium (1.37 mL [2.5 M solution in hexanes], 3.7 mmol) to prepare the lithium diisopropylamide reagent. The solution was stirred for 30 minutes under N_2 at 0 ^{o}C, then cooled back down to -78 ^{o}C for the dropwise addition of a solution of 2,2'-bithiazole (200 mg, 1.22 mmol) in THF (1 mL) which generated an orange solution. After stirring at -78 ^{o}C for 2 hours a solution of trimethyl tin chloride (4.44 mL [1.0 M solution in hexanes], 4.44 mmol) was added, and the reaction mix allowed to reach room temperature and stir for 12 hours. The reaction mix was then poured into distilled H_2O, extracted with DCM, and the combined organic fractions washed with brine and dried over $MgSO_4$. The solvent was removed then the product was washed with hexanes at -78 ^{o}C, leaving 0.417 g of an off-yellow/orange solid (69% yield).[113] ^{1}H NMR (300 MHz, $CDCl_3$) δ 7.79 (s, 2H), 0.44 (s, 18 H). Please see Figure A-5 in Appendix for spectrum.

2.2.1.6 Polymerization of PDBPyBTz

An oven-dried 10 mL microwave vial was charged with monomer **5** (150 mg, 3.04×10^{-4} mmol), monomer **3** (305.5 mg, 3.04×10^{-4} mmol, triphenylphosphine (9.3 mg, 3.55×10^{-5} mmol), tris(dibenzylideneacetone)dipalladium(0) (8.06 mg, 8.81×10^{-6} mmol),

anhydrous toluene (7.8 mL) and anhydrous dimethylformamide (0.78 mL) under nitrogen atmosphere. The mixture was placed in a microwave reactor for 60 minutes at 100 ^{o}C at 200 W power while stirring at 0 atm. The color of the reaction mixture turned from blue to purple after polymerization. The reaction mix was then precipitated into methanol, and the solids collected by filtering through a cellulose Soxhlet thimble. The polymer was then purified via sequential Soxhlet extraction in MeOH (24 hr), acetone (24 hr), hexanes (24 hr), and extracted with $CHCl_3$ (24 hr). The concentrated chloroform solution was precipitated in MeOH and filtered to yield 0.217 g of blue solid (48% yield). NMR spectra (Figure A-6, Figure A-7, appendix) of very low resolution, and individual peaks cannot be identified and for this reason no couplings or integration data are included. ^{1}H NMR ($CDCl_3$, 700 MHz) δ 9.10-7.41 (m, aromatic peaks), 4.34 (m, presumably N-CH_2 peak), 1.98-0.57 (m, alkyl peaks). ^{13}C NMR ($CDCl_3$, 700 MHz, ppm) δ 161.92, 160.66, 149.81, 145.93, 144.09, 141.37, 137.51, 133.46, 127.62, 111.59, 38.31, 31.93, 31.47, 30.10, 29.70, 29.39, 26.45, 22.68, 14.12 (many overlapping peaks). M_w = 11,849, PDI ($Đ$) = 1.7 (Figure 2-4). T_g at 66.9 ^{o}C.

2.2.1.7 Molecular Weight Distribution

PDBTz was synthesized according to literature procedures[113] using **1** as the side chain, with a M_W of 46,175, M_N of 12,042 g/mol and $Đ$ of 3.83 (Figure 2-5). A commercial sample of PDBPyBT was purchased from Ossila chemical, and found to have a M_W of 29,300, M_N of 11,350, and $Đ$ of 2.58 (Figure 2-6). GPC analysis was performed under the same conditions for all polymers for consistency.

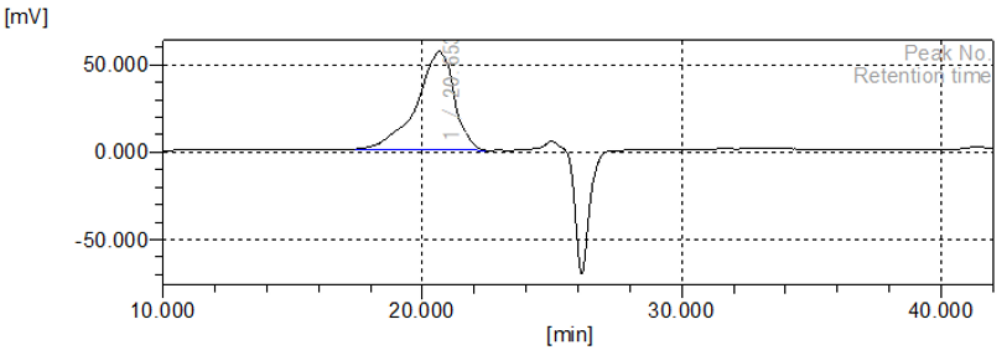

Molecular mass calculation result (RI)

Total

	[min]	[mV]	[mol]		
Peak start	17.390	1.772	145,299	Mn	6,915
Peak top	20.653	57.493	6,733	Mw	11,849
Peak end	22.465	1.079	1,223	Mz	24,393
				Mz+1	45,728
				Mv	11,849
Height [mV]			56.167	Mp	6,734
Area [mV*s]			5672.407	Mz/Mw	2.059
Height% [%]			100.000	Mw/Mn	1.714
[eta]			11848.56967	Mz+1/Mw	3.859

Figure 2-4 GPC characterization of PDBPyTz in 1,3,5-trichlorobenzene at 135 °C.[2]

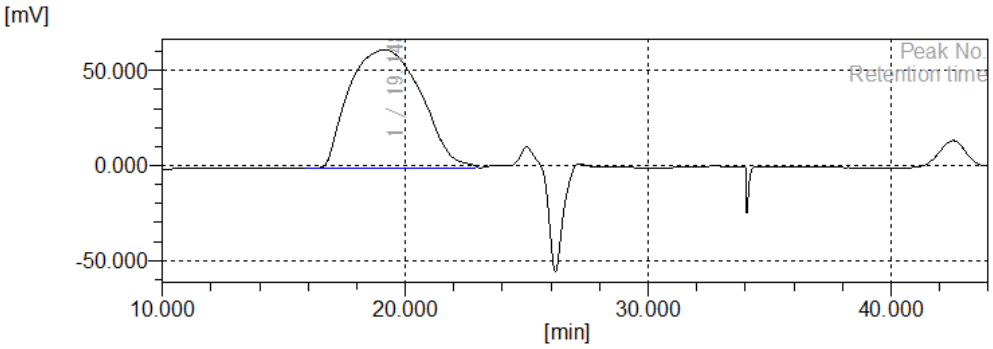

Molecular mass calculation result (RI)

Peak 1 Valley Peak

	[min]	[mV]	[mol]		
Peak start	15.908	-1.411	583,356	Mn	12,042
Peak top	19.148	60.943	30,350	Mw	46,175
Peak end	22.923	-0.583	409	Mz	96,606
				Mz+1	142,923
				Mv	46,175
Height [mV]			62.403	Mp	36,240
Area [mV*s]			12887.977	Mz/Mw	2.092
Area% [%]			100.000	Mw/Mn	3.835
[eta]			46175.07076	Mz+1/Mw	3.095

Figure 2-5 GPC characterization of PDBTz with TCB at 135 °C.[3]

[2] GPC analysis of PDBPyBTz done by Dr. Bing Xu

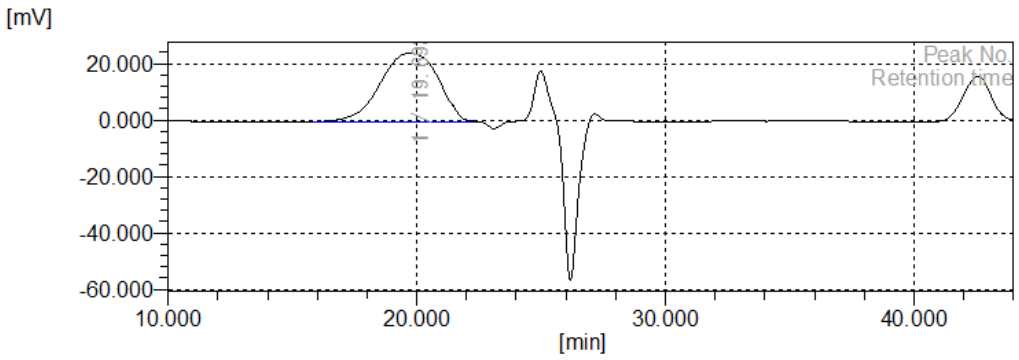

Molecular mass calculation result (RI)

Peak 1 Valley Peak

	[min]	[mV]	[mol]		
Peak start	15.813	-0.584	639,841	Mn	11,350
Peak top	19.693	23.775	18,101	Mw	29,300
Peak end	22.355	-0.499	903	Mz	77,723
				Mz+1	180,095
				Mv	29,300
Height [mV]			24.463	Mp	20,615
Area [mV*s]			3967.822	Mz/Mw	2.653
Area% [%]			100.000	Mw/Mn	2.582
[eta]			29300.07001	Mz+1/Mw	6.147

Figure 2-6 GPC characterization of PDBPyBT with TCB at 135 ^{o}C.[4]

2.2.1.8 Thermal Characterization

PDBPyBTz is stable up to 335 ^{o}C (Figure 2-7). DSC characterization (Figure 2-8) showed a glass transition temperature at 66.9 ^{o}C but no other thermal transitions up to 290 ^{o}C. These results are not unusual as it is common for conjugated DPP-polymers to exhibit high thermal stability and not have a melting temperature below the decomposition temperature.

[3] GPC analysis of PDBTz done by Bronson Cox
[4] GPC analysis of PDBPyBT done by Bronson Cox

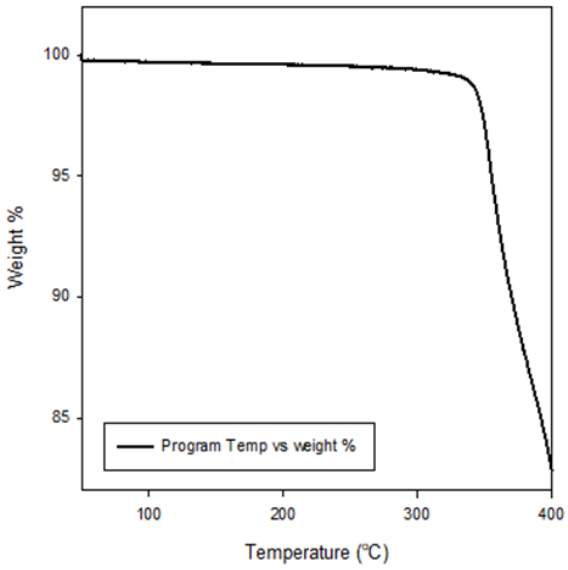

Figure 2-7 Thermogravimetric Characterization of PDBPyBTz in nitrogen atmosphere (25 mL/min) at a heating rate of 10 °C/min.

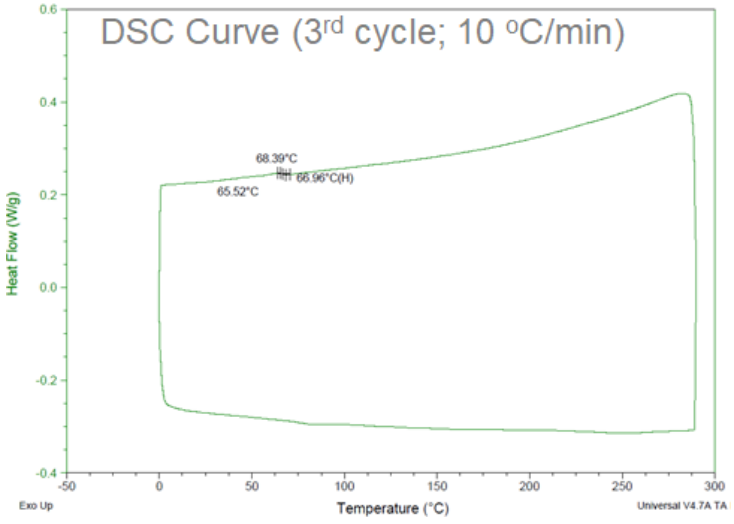

Figure 2-8 Thermal characterization of PDBPyBTz using differential scanning calorimetry. DSC characterization was based on the 3rd heating/cooling process in a nitrogen atmosphere with a nitrogen flow rate of 50 mL/min and a heating/cooling rate of 10 °C/min.

2.3 Results and Discussion

2.3.1 Molecular Geometry and Frontier Orbitals[5]

It is useful to begin with a discussion of the equilibrium geometry of PDBPyBTz at room temperature, as the planarity of the conjugated backbone directly impacts the conjugation length along a single polymer chain. The total energies of a single repeat unit of PDBPyBTz were calculated as a function of the indicated torsional angles shown in Figure 2-9 (note the alkyl chains were replaced with a t-butyl group to save computational time). Thermal energy at standard temperature (300 K) is denoted with the black dotted line for reference.

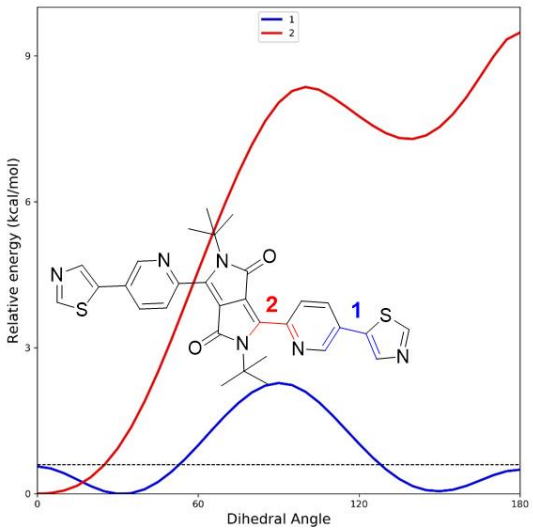

Figure 2-9 Potential energy surface (PES) curves illustrating the torsional angles between the DPP and pyridinyl units (red line), between the pyridine and thiazole units (blue line), with the geometry optimized at the ωB97X-D/6-31G(d,p) level of theory. The dotted line

[5] The results presented in Section 2.3.1 are a result of a collaboration primarily between Dr. Simil Thomas (Bredas lab) and Carolyn Buckley (myself). All computations were performed by Dr. Simil Thomas and are presented here as they are integral to the interpretation of experimental results and hence the conclusions made from the study. In no way do I claim credit for any of the computations presented here. All figures containing computational results will be noted in the spirit of full transparency and to avoid any confusion.

represents thermal energy at 300 K (≈0.6 kcal/mol). [Computational results done by Dr. Simil Thomas]

There are two energy minima at 30° and 150° for the torsional angle between the thiazole and pyridinyl units, with a small barrier height of *ca.* 2.4 kcal mol^{-1} (less then ambient thermal energy) at 0° between these minima. As the 2,2'-bithiazole moiety is known to be planar[117], one can expect the entire monomer unit to be oriented ± 30° with the neighboring pyridinyl moieties at room temperature. The torsional angle between the pyridine and DPP-core has a single minimum at 0°, with a large torsional energy barrier far surpassing thermal energy at 300 K. It clear that the pyridinyl nitrogen energetically favors facing the neighboring amide nitrogen and will not deviate far from this coplanar formation in ambient conditions.[113]

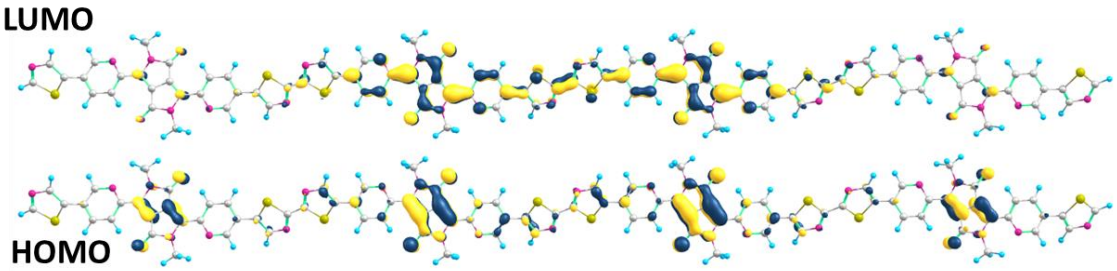

Figure 2-10 Visualization of the frontier molecular orbitals of the PDBPyBTz tetramer obtained at the tuned-ωB97XD/6-31G(d,p) level. [Calculations done by Dr. Simil Thomas]

The frontier molecular orbital wavefunctions for the PDBPyBTz tetramer are shown in Figure 2-10. The orbital coefficients are indicated by the size of the colored 'clouds' above and below the respective atoms, representing the electron density distribution across the surface of the molecule with the parity of the orbitals denoted by color. It can be seen (Figure 2-10) that the HOMO is localized on the core DPP moieties,

while the LUMO is slightly more delocalized across the conjugated backbone with noticeably larger orbital coefficients on the pyridinyl and bithiazole moieties.

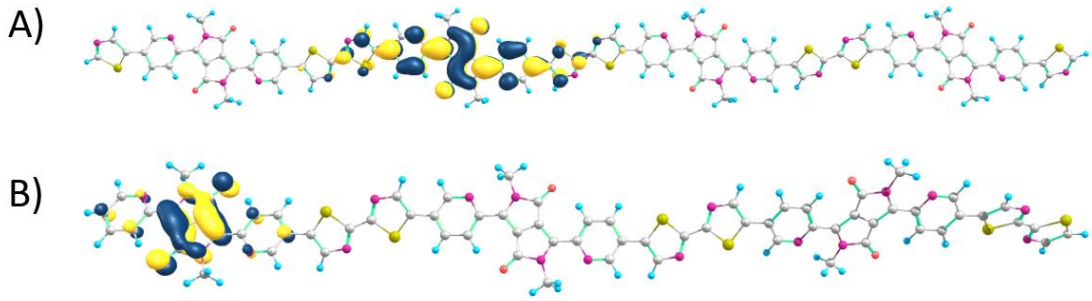

Figure 2-11 Singly occupied molecular orbitals (SOMOs) of the PDBPyBTz tetramer, depicting a) the anion and b) the cation wavefunctions. [Calculations done by Dr. Simil Thomas as the ωB97XD/6-31G(d,p) level]

In a transistor device the injection of holes and electrons from the source and drain contacts under an applied bias essentially 'dopes' the polymer semiconductor, and so it is useful to visualize how the electron density is distributed across the molecular structure in the cationic and anionic forms (as it would be in bearing injected holes and electrons, respectively). Figure 2-11a shows the anion wavefunction distributed across a single repeat unit of the PDBPyBTz tetramer, while Figure 2-11b shows the cation wavefunction largely localized on the DPP core and minimally present on the flanking pyridinyl units.

2.3.2 Characterization of Optoelectronic Properties

The UV-vis absorption spectra for both solution and blade-coated thin films of PDBPyBTz are presented in Figure 2-12, while the spectral characteristics are summarized in Table 2-1. The more intense absorption bands between 550-700 nm, and the lower intensity bands between 350-450 nm are attributed to π-π* transitions. Minimal positive solvatochromism was seen in the 0-1 blue-shift of λ_{max} from the chloroform to p-xylene

solutions, indicating a slight destabilization of this excited state upon decreasing solvent polarity.[118] The λ_{max} of the chloroform solution (632 nm) and thin film (656 nm) for the 0-0 transition of PDBPyBTz is blue-shifted from that of its bithiophene analog, PDBPyBT (683 nm and 695 nm, respectively)[106] and its thiophene substituted DPP analog PDBTz (767 nm and 765 nm, respectively).[113] This is consistent with the lesser electron-rich nature of PDBPyBTz that consists of two acceptor units, in comparison to that in typical D-A copolymers.

Table 2-1 UV-Vis spectral absorption characteristics of PDBPyBTz and analogous previously reported polymer structures.

		0-0		0-1		
Polymer	Solvent	$\lambda_{max}^{abs, soln}$ [nm]	$\lambda_{max}^{abs, film}$ [nm]	$\lambda_{max}^{abs, soln}$ [nm]	$\lambda_{max}^{abs, film}$ [nm]	E_g^{opt} [eV]
PDBPyBTz	$CHCl_3$	632	656	591	600	1.47
	p-xylene	636	656	588	602	1.47
PDBTz[113]	$CHCl_3$	767	765	702	697	1.33
PDBPyBT[106]	$CHCl_3$	683	695	~630	~650	1.65

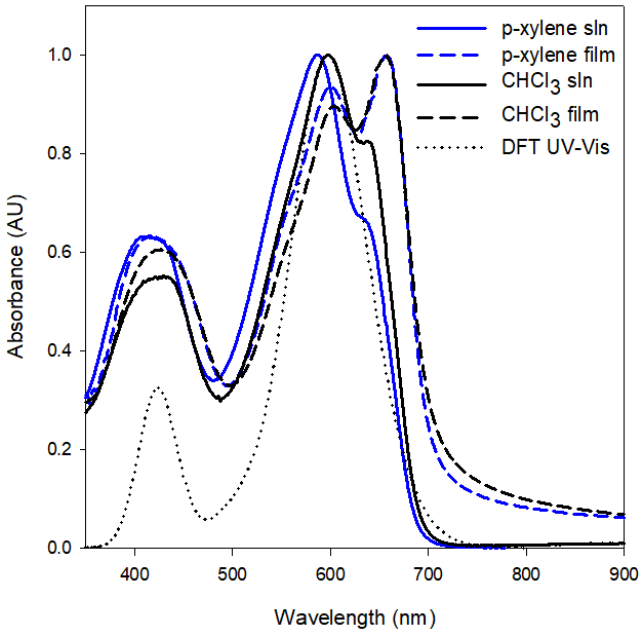

Figure 2-12 UV-Vis Spectra of PDBPyBTz in both solution (1 x 10^{-6} M, chloroform, p-xylene) and thin film, and the calculated TD-DFT spectrum (assuming a surrounding medium with a dielectric constant corresponding to $CHCl_3$) [DFT done by Dr. Simil Thomas]. Film UV-Vis spectra were obtained by spincoating solutions onto UV-ozone cleaned SiO_2 slides before deposition.

The changes observed in the solution vs. solid-state absorption spectra are consequences of an increase in intermolecular interactions and molecular ordering among the PDBPyBTz chains, and can provide insight into the types of aggregates formed, provided that the strengths of the intermolecular excitonic coupling and vibronic coupling are similar.[119] The absorption spectra of the thin films, having similar maxima at 656 nm, are bathochromically shifted from the solution spectra of the polymer in either solvent, which is indicative of J-aggregation according to Kasha's theory.[120] In addition, the ratio of the first two vibronic peak intensities for the 0-0/0-1 transitions is below unity in both solution spectra and becomes inverted in the thin-film absorption spectra. This observation is further evidence of J-aggregation, as it has been shown that with increasing exciton bandwidth, J-[H]-aggregates will show an increase [decrease] in the ratio of the oscillator

strengths of the first two vibronic peaks in absorption spectra.[119,121,122] Interestingly, there is no change in the λ_{max} of the films after annealing above the T_g at 100 °C for 1.5 hours. The optical gap (E_g^{opt}) of PDBPyBTz evaluated from the solid-state absorption onset is *ca.* 1.47 eV, which is smaller than that of PDBPyBT (E_g = 1.65 eV)[106] but larger than that of PDBTz (E_g = 1.33 eV).[113]

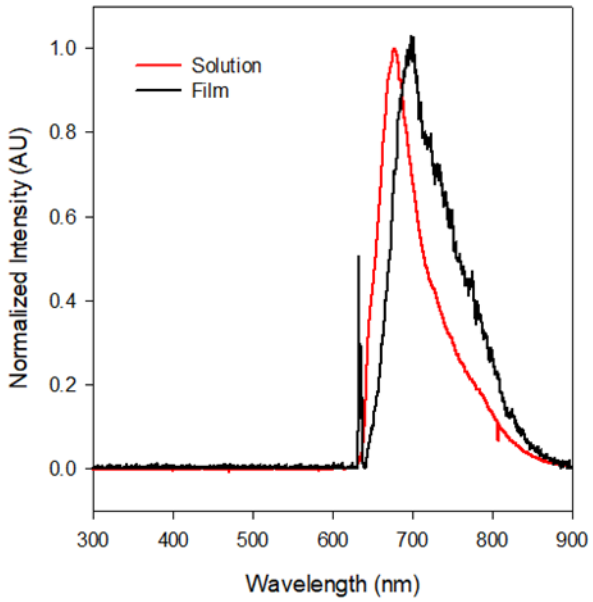

Figure 2-13 Photoluminescence spectra of PDBPyBTz in both solution (chloroform) and thin film.[6]

Photoluminescence spectra of PDBPyBTz were obtained for both solution and thin-film, using an excitation wavelength of 637 nm from a continuous-wave laser (Figure 2-13). The fluorescence spectrum of the thin film had a λ_{max} of 698 nm, while λ_{max} in the solution state was at 679 nm. It should be noted that the fluorescence spectra are not mirror

[6] PL spectra obtained with much help from Dr. Ilaria Bargigia

images of the absorption spectra, both being single-peaked and displaying Stokes shifts of 47 and 42 nm for solution and film absorption maxima, respectively.

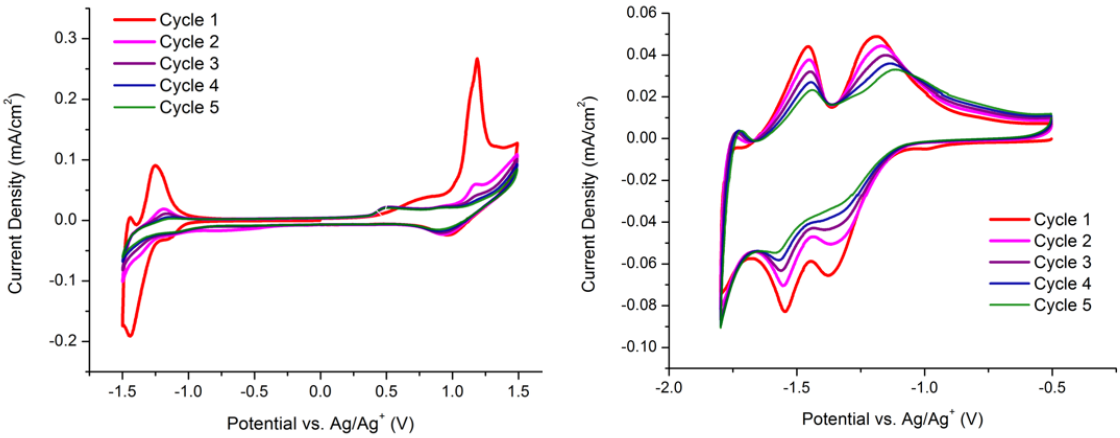

Figure 2-14 Electrochemical characterizations of PDBPyBTz polymer films under cyclic voltammetry (CV). PDBPyBTz thin films drop-casted on glassy carbon electrode. $TBAPF_6$ (0.5 M, propylene carbonate) electrolyte, Ag/Ag^+ (10mM $AgNO_3$/MeCN, 0.085 V vs. Fc/Fc^+) reference electrode.

The redox potentials of PDBPyBTz thin films were investigated using cyclic voltammetry (Figure 2-14). PDBPyBTz exhibits an onset reduction peak at -1.256 V (vs. Fc+/Fc), followed by two reversible reduction peaks at -1.460 V and -1.618 V (vs. Fc/Fc+). The reversibility of the two reductions demonstrates the stability of PDBPyBTz as an electron carrier. An onset oxidation potential is seen at 0.346 V (vs. Fc+/Fc), followed by an irreversible oxidation peak at 1.131 V (vs. Fc+/Fc). As the energy of the standard calomel electrode (SCE) is taken to be 4.7 eV vs. vacuum[123], and Fc+/Fc is +0.380 V vs. SCE[38], the formal potential of the Fc+/Fc redox couple can be approximated as -5.1 eV on the energy scale.[44,100] With this approximation, the onset oxidation and reduction potentials correspond to an ionization potential (IP) and electron affinity (EA) of 5.45 and 3.84 eV, respectively, and a transport gap of 1.61 eV.

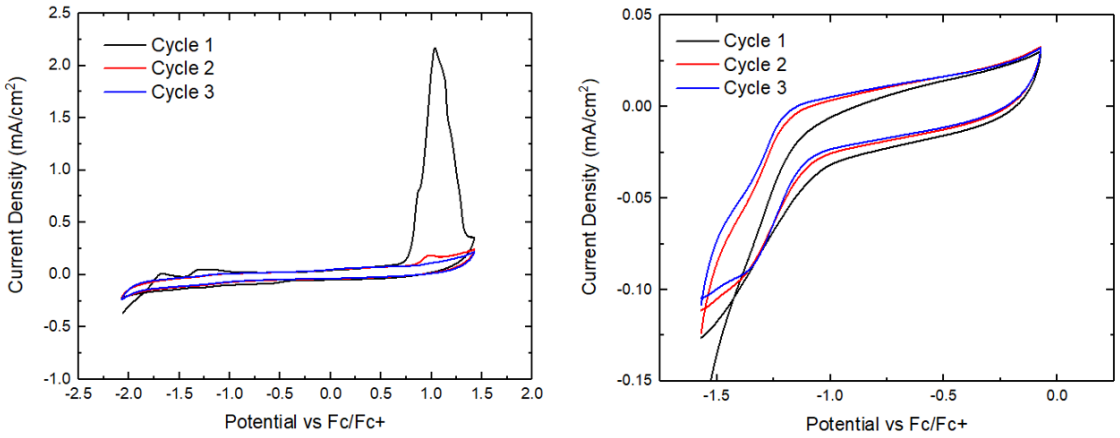

Figure 2-15 Cyclic voltammograms of PDBPyBT polymer films. Polymer thin films drop-casted on glassy carbon electrode. $TBAPF_6$ (0.5 M, propylene carbonate) electrolyte, Ag/Ag^+ (10 mM $AgNO_3$/MeCN, 0.085 V vs. Fc/Fc^+)[7]

The ionization potentials of PDBPyBTz and PDBTz were estimated from cyclic voltammetry in a similar manner, using the approximations mentioned above. PDBPyBT (Figure 2-15) had an irreversible oxidation peak at +1.033 V (vs. Fc/Fc+) with an onset oxidation potential of +0.7429 V (vs. Fc/Fc+). One reversible reduction peak can be seen at -1.335 V (vs. Fc/Fc+), with the onset reduction potential at -1.055 V (vs. Fc/Fc+). These onset oxidation and reduction potentials of PDBPyBT correspond to an IP of -5.84 eV and an EA of -4.04 eV, respectively.

[7] CV of PDBPyBTz taken by Brian Khau

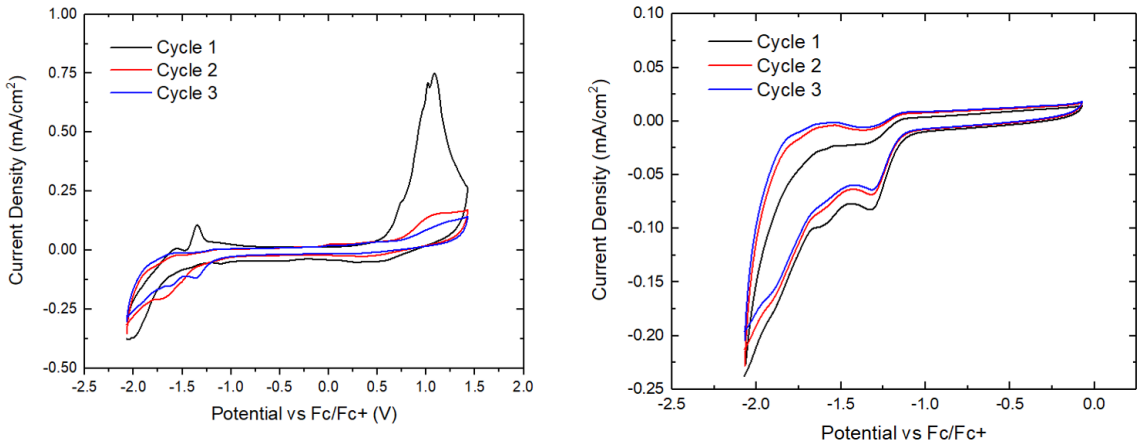

Figure 2-16 Cyclic voltammograms of PDBTz polymer films. Polymer thin films drop-casted on glassy carbon electrode. $TBAPF_6$ (0.5 M, propylene carbonate) electrolyte, Ag/Ag+ (10 mM $AgNO_3$/MeCN, 0.085 V vs. Fc/Fc+) reference electrode.[8]

PDBTz (Figure 2-16) has two reversible reduction peaks at -1.323 V and -1.599 V (vs. Fc/Fc+), with the onset of the (first) reduction at 1.140 V (vs. Fc/Fc+). The irreversible oxidation peak at +1.083 V (vs. Fc/Fc+) in the first potential sweep is preceded by the onset oxidation potential of +0.499 V (vs. Fc/Fc+). These onset oxidation and reduction potentials of PDBTz correspond to an IP of -5.60 eV and an EA of -3.96 eV, respectively.

[8] CV of PDBTz taken by Brian Khau

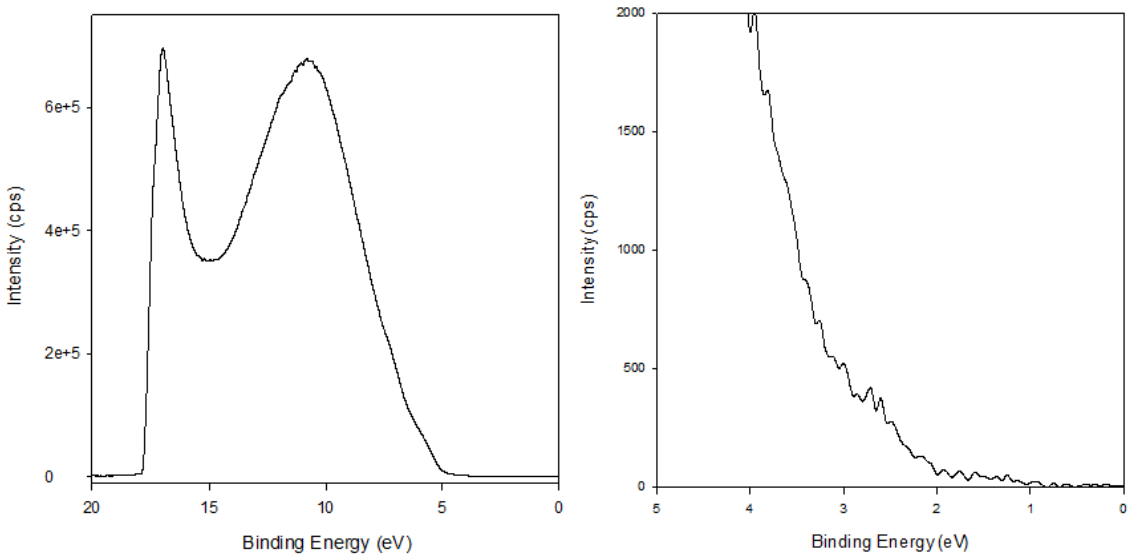

Figure 2-17. (left) UPS characterization of blade-coated PDBPyBTz film on ITO-coated glass; (right) zoomed-in of lower binding energy region of UPS spectrum.

Ultraviolet photoelectron spectroscopy (UPS) was used to determine the intrinsic IP of thin films of PDBPyBTz, which was found to be 5.2 eV (Figure 2-17). With an optical gap of 1.47 eV and an exciton binding energy of approximately 0.14 eV (estimated using the transport gap of 1.61 eV), this would predict an electron affinity of 3.59 eV. Considering the assumptions and uncertainties inherent to conversion factors relating redox potentials to solid-state ionization potentials, we consider the values obtained from the UPS measurements to be consistent with that estimated from the cyclic voltammetry results.[44,124] Both the CV and UPS results of PDBPyBTz are suggestive of good ambient stability towards oxidation.[69]

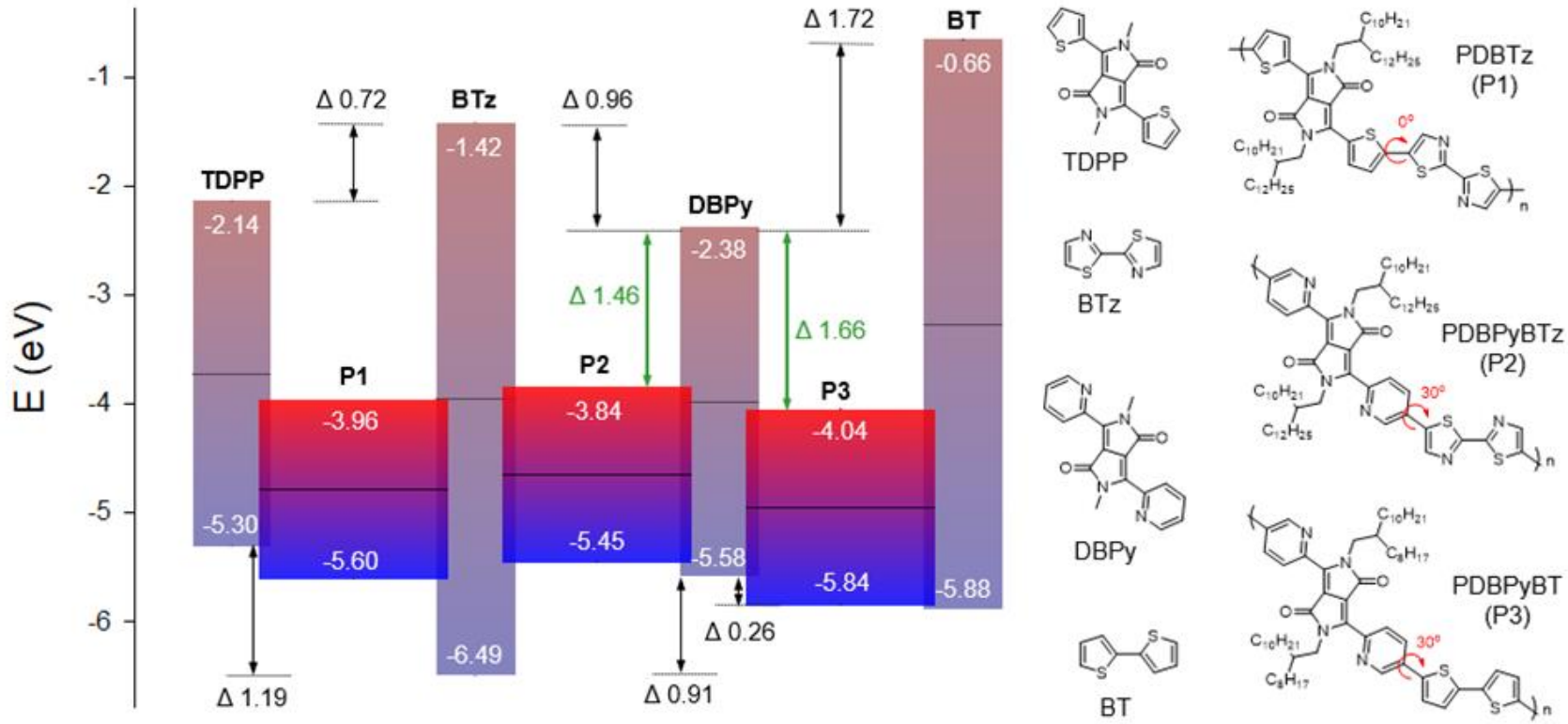

Figure 2-18**.** Comparison of the DFT-ωB97XD calculated [by Dr. Simil Thomas] ionization potentials and electron affinities for the monomer units with the experimental values for the resultant polymers, in units of eV. Energy differences between monomer units are given in black, and energy differences between EA energies are given in green.

A comparison of the calculated and experimental IPs and EAs between PDBPyBTz, analogous materials PDBTz and PDBPyBT, and component monomers reveals the difficulties in determining structure-property relationships in narrow bandgap polymeric semiconductors (Figure 2-18). In contrast with previous studies[113,125] and the conventional approach to the D-A (and A-A) design strategy, the substitution of the bithiophene moiety with bithiazole in PDBPyBTz did not result in larger estimated IP and EA values than those observed for PDBPyBT. Similarly, the use of the DBPy moiety did not result in the expected lower ionization energies in comparison to the TDPP moiety.[106] Electrochemical methods of estimating gas-phase ionization potentials present a number of sources of uncertainty which make it difficult to evaluate the precision of these estimations and consequently the qualitative value in comparing estimations between polymer semiconductors.[42–44,126] Indeed, there are minor discrepancies observed between previously reported estimations of IP and EA for PDBPyBT[106], PDBTz[113], and those reported here. Bearing these uncertainties in mind, the results can be understood by examining the theoretical MO calculations of the frontier orbital geometries in assessing the effectiveness of π-delocalization in the system.

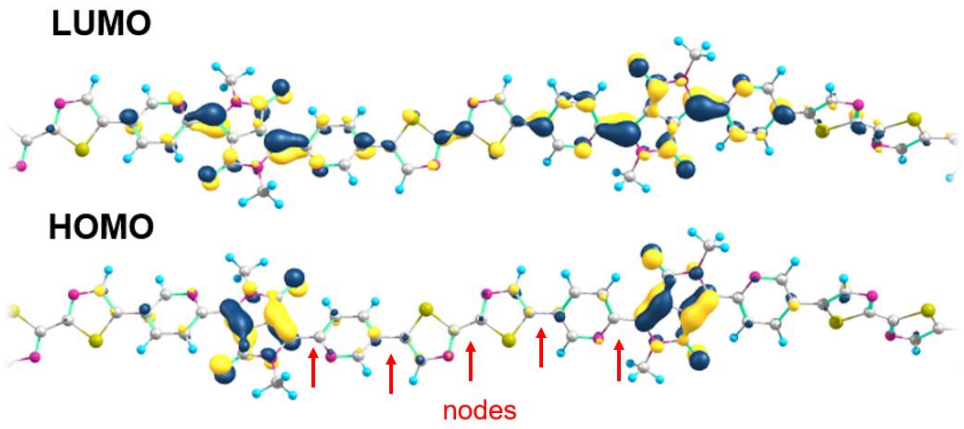

Figure 2-19 Magnification of the frontier orbital wavefunctions for examining the orbital parities. Representative nodes in the HOMO wavefunction are denoted with red arrows. [Calculations done by Dr. Simil Thomas]

As discussed above, the HOMO coefficients are localized on the DPP aromatic core and minimally present on the flanking pyridinyl moieties or BTz units (Figure 2-10). Upon closer inspection, nodes in the HOMO wavefunction can be seen on both the pyridinyl carbon atoms connected to the DPP core, between the atoms connecting the pyridinyl and BTz moieties, and between the two adjacent thiazole moieties (Figure 2-19). Nodes between these units are absent in the LUMO wavefunction, which has greater delocalization along the polymer chain. Similar nodal patterns are seen between the SOMOs of the ions, with the anion wavefunction delocalized across the repeating unit and the cation wavefunction localized on the DPP core (Figure 2-11). The electronic structure of these wavefunctions may explain why greater LUMO stabilization was seen in PDBPyBT than in PDBPyBTz despite a larger energy difference between the monomer units of the former (Figure 2-18). These observations highlight the need to consider the fundamental principles of perturbation MO theory in selecting monomeric units using the A-A design strategy; namely, that the strength of the interaction is not only dependent on

the relative orbital energies of the component moieties, but also a function of the degree of orbital overlap which affects the final shape of the product orbitals.[15] The differences in the spatial extent of positive and negative charge carriers has implications for charge transport[49,127] between holes and electrons in thin films,[46] which can affect the performance of these materials in OFET devices.[128]

2.3.3 OFET Device Characteristics

The charge carrier properties of PDBPyBTz were evaluated in bottom-gate, bottom-contact (BGBC) OFET devices using a p-doped Si substrate as the gate electrode, with a 300 nm thick layer of thermally grown SiO_2 as the gate dielectric, which was passivated with OTS-18 to minimize surface charge trapping. As stated in the experimental section of this chapter, the fixed channel dimensions were 50 μm in length and 2 mm in width.

Similar to a previous report of an all-acceptor DPP-polymer,[97] PDBPyBTz-based OFETs demonstrated solely n-channel transport with negligible hysteresis (Figure 2-20), and no obvious source-drain current under negative gate bias even when Au electrodes were used. The mobilities were extracted from the saturation regime, and the OFET performance measured for six devices under each processing condition. Representative transfer and output curves for PDBPyBTz OFET devices blade-coated from p-xylene are shown in Figure 2-21 and Figure 2-22, respectively. The average electron mobility (μ_e) of blade-coated PDBPyBTz devices were approximately 0.02 $cm^2V^{-1}s^{-1}$, with a maximum μ_e of 0.054 $cm^2V^{-1}s^{-1}$ (Table 2-2).

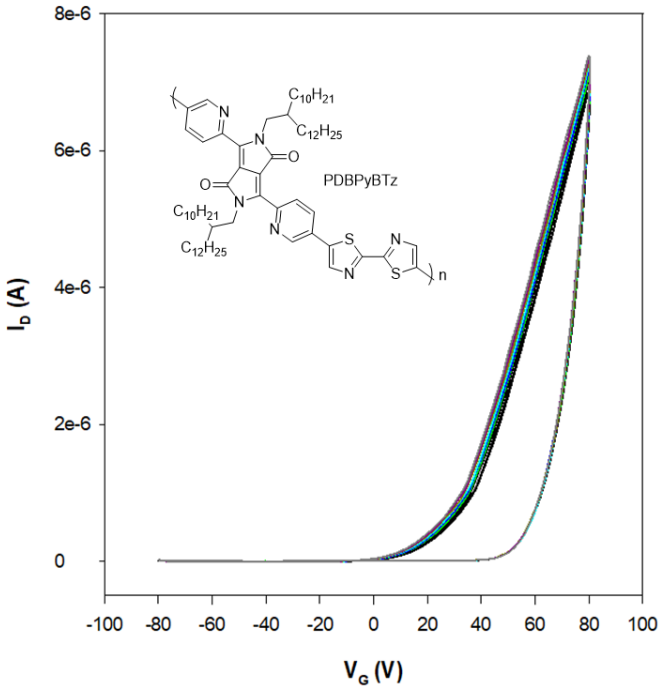

Figure 2-20 Transfer curve of BGBC OFET device with PDBPyBTz (blade-coated from p-xylene solution) over a gate bias range of -80 V to 80 V over 20 consecutive potential sweeps. The scale of the current (I_D) is linear as shown here.

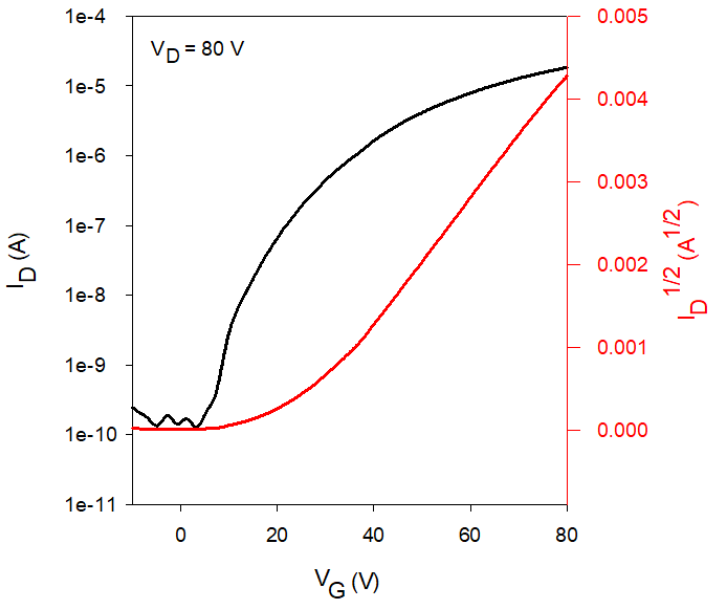

Figure 2-21 Representative transfer curve of PDBPyBTz blade-coated from p-xylene solution in BGBC OFET under positive gate bias in the saturation regime, zoomed-in to show the linearity of the $I_D^{1/2}$ vs. V_G curve.

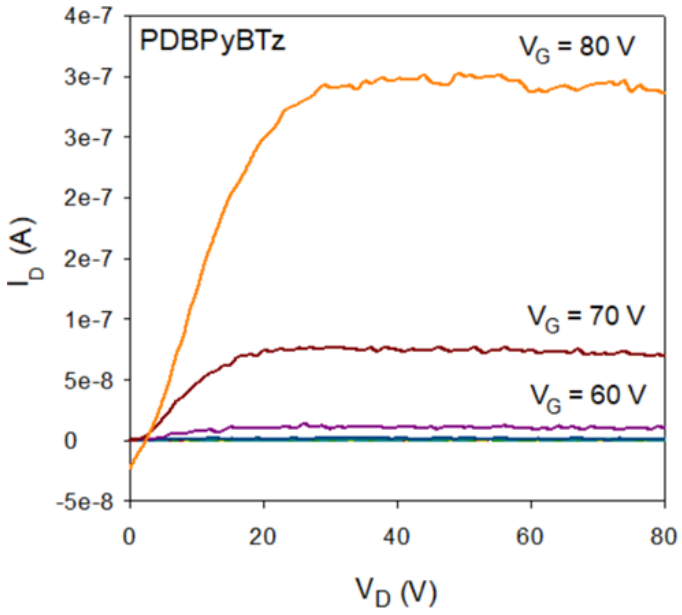

Figure 2-22 Representative output curves of PDBPyBTz (blade-coated from p-xylene) BGBC OFET devices (corresponding to that shown in Figure 2-21).

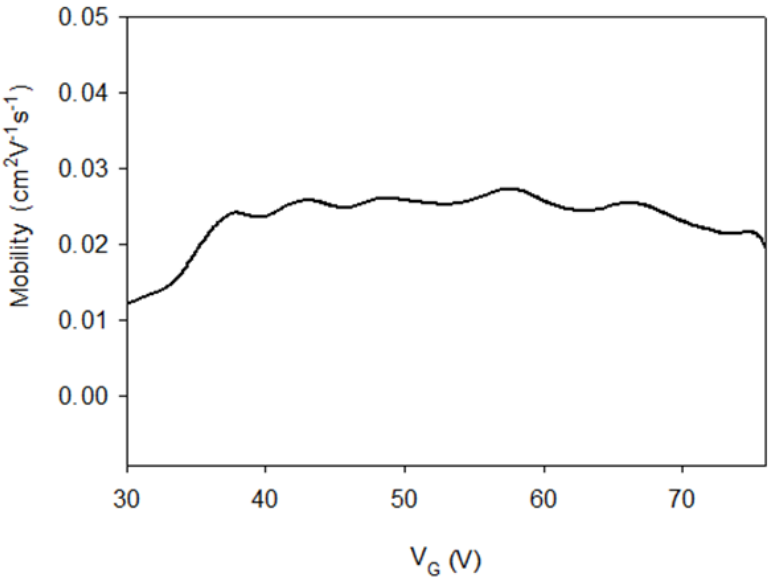

Figure 2-23 Plot of mobility vs. gate bias of PDBPyBTz devices

The mobility is reasonably independent of gate bias over a large voltage range (specifically the range from which mobilities were extracted), as shown in Figure 2-23. This suggests the devices do not violate the assumptions of the gradual channel

approximation and gives us confidence that the mobilities extracted from the data using the Schockley equations are reasonably accurate.[60,61] Below a gate bias of approximately 35 V, the mobility becomes noticeably dependent on the gate bias as the device enters the sub-threshold regime.

Table 2-2 FET transport properties of PDBPyBTz on OTS-modified BGBC OFET devices under varying annealing temperatures and processing solvents.

Polymer	Solvent	Annealing	μ_e [$cm^2V^{-1}s^{-1}$]		V_T	I_{ON}/I_{OFF}
			Average	Max	[V]	
PDBPyBTz	$CHCl_3$	Pristine	0.010 ± 0.002	0.013	23.1 ± 2.2	10^4-10^5
		100 ºC	0.019 ± 0.002	0.022	22.6 ± 2.9	10^2-10^5
		125 ºC	0.017 ± 0.001	0.019	18.0 ± 1.3	10^2-10^6
		150 ºC	0.017 ± 0.001	0.019	20.1 ± 3.4	10^3-10^4
	p-xylene	Pristine	0.018 ± 0.007	0.023	27.5 ± 1.0	10^4-10^5
		100 ºC	0.021 ± 0.002	0.027	26.2 ± 1.5	10^2-10^6
		125 ºC	0.020 ± 0.001	0.023	23.9 ± 2.5	10^4-10^6
		150 ºC	0.023 ± 0.002	0.030	30.5 ± 3.5	10^3-10^6

As shown in Table 2-2, there did not appear to be much difference in OFET performance between PDBPyBTz devices blade-coated from p-xylene or chloroform. Additionally, annealing the devices only marginally improved the OFET performance, with no clear trends seen in the averaged data. While PDBPyBTz did not show a melting temperature below its decomposition temperature, the annealing temperatures used were above the T_g (Figure 2-7, Figure 2-8). The annealing results are unusual for organic semiconductors, as annealing typically allows for the polymer chains to locally arrange themselves in more thermodynamically favorable arrangements maximizing intermolecular (interchain) interactions, which is coincidentally beneficial for charge transport (e.g. increased crystallinity, increased interchain interactions, closer π-π stacking, etc).[129–131]

As the reference publications of the analogous PDBPyBT and PDBTz polymers reported the mobilities of devices of different architectures and materials[106,113], it was decided that the performance of these semiconductors in OFET devices (identical to those used for PDBPyBTz in this study) under the same processing conditions would provide for an invaluable comparison between the three semiconductors. The OFET performance data for spin-coated and blade-coated devices of the polymers are shown in Table 2-3 (gate leakage currents shown in Figure A-15). The data was collected from 6 devices for each processing condition. Interestingly, there were only negligible differences in n-channel performance between spin- and blade-coated devices of PDBPyBTz. In contrast, PDBPyBTz and PDBTz demonstrated remarkably different performance from PDBPyBTz (Figure 2-24). Both PDBPyBT and PDBTz demonstrated ambipolar behaviour whereas

PDBPyBTz was unipolar (n-channel) in the same OFET device structures (Figure 2-24 and Figure 2-25).

Table 2-3 OFET performance results of PDBPyBTz, PDBPyBT, and PDBTz under various processing conditions

Polymer	Process	Solvent	μ_e [$cm^2V^{-1}s^{-1}$]		V_T	I_{ON}/I_{OFF}	μ_h [$cm^2V^{-1}s^{-1}$]		V_T	I_{ON}/I_{OFF}
			Average	Max	[V]		Average	Max	[V]	
PDBPyBTz	Blade	$CHCl_3$	0.010 ± 0.002	0.013	23.1 ± 2.2	10^4-10^5	-	-	-	-
		p-xylene	0.019 ± 0.002	0.022	22.6 ± 2.9	10^2-10^5	-	-	-	-
	Spin	$CHCl_3$	0.018 ± 0.007	0.023	27.5 ± 1.0	10^4-10^5	-	-	-	-
		p-xylene	0.021 ± 0.006	0.032	23.9 ± 2.5	10^4-10^5	-	-	-	-
PDBPyBT	Blade	$CHCl_3$	6.6×10^{-4} $\pm 5.5\times10^{-4}$	1.9×10^{-3}	14.2 ± 9.6	10^2-10^4	5.07×10^{-4} $\pm 1.3\times10^{-4}$	7.5×10^{-4}	-23.8 ± 6.81	10^3-10^4
		p-xylene	4.4×10^{-4} $\pm 7.8\times10^{-5}$	5.51×10^{-4}	-37.9 ± 6.3	10^2-10^3	4.6×10^{-4} $\pm 2.1\times10^{-3}$	2.1×10^{-3}	-31.9 ± 4.84	10^2-10^3
	Spin	$CHCl_3$	0.020 ± 0.007	0.031	-16.5	10^4	*	*	*	*
		p-xylene	0.065 $\pm 7.4\times10^{-4}$	0.031	-18.6 ± 3.9	10^2-10^3	*	*	*	*
PDBTz	Blade	p-xylene	2.24×10^{-4} $\pm 5.2\times10^{-5}$	3.6×10^{-4}	-6.24 ± 1.5	10^2	*	*	*	*

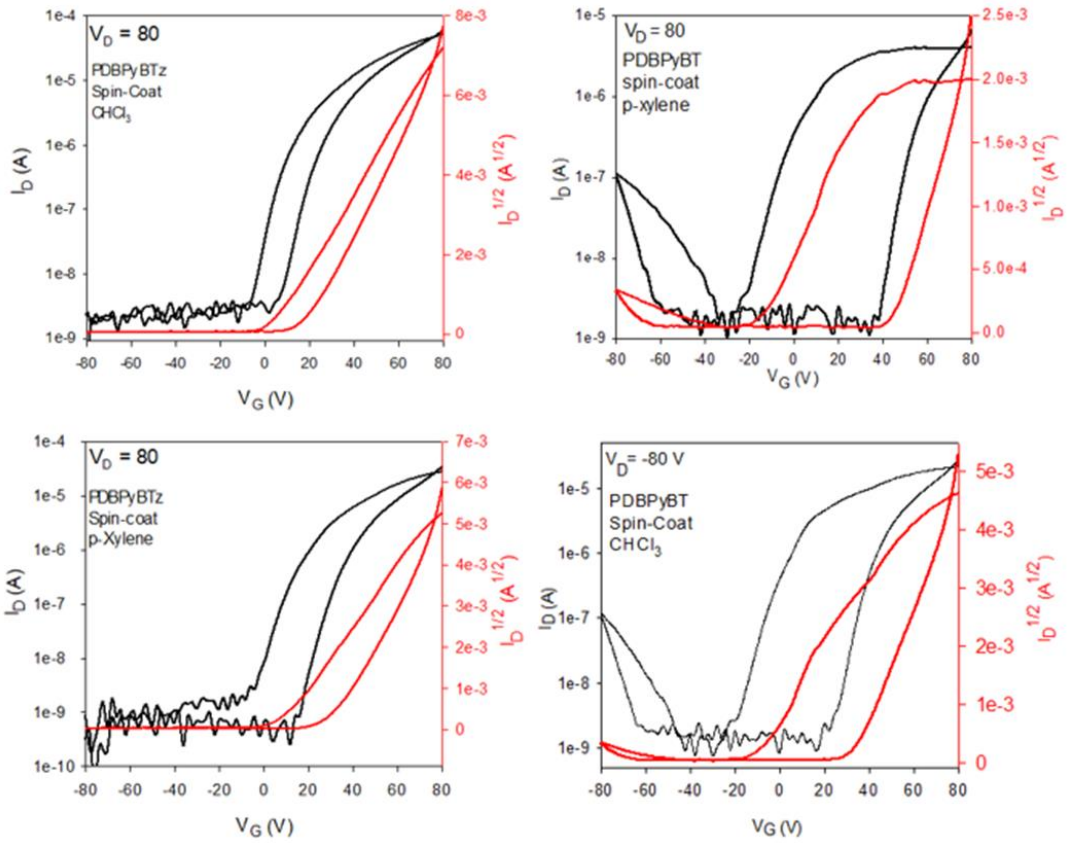

Figure 2-24 Representative comparison of transfer characteristics of the BGBC OFET devices fabricated by spin-coating solutions of PDBPyBTz (left) and PDBPyBT (right) from $CHCl_3$ (top) and p-xylene (bottom) solutions.

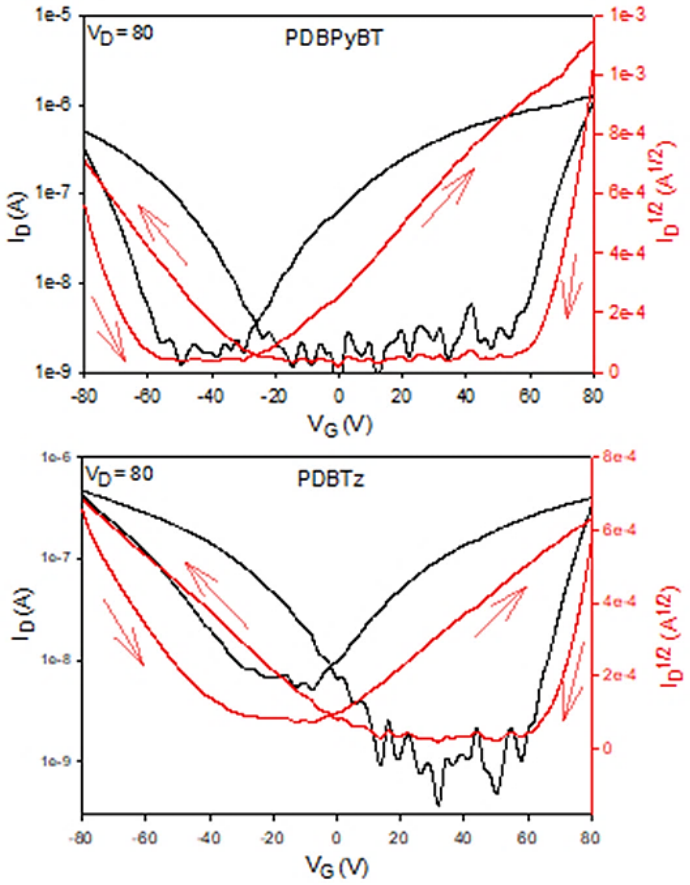

Figure 2-25 Transfer characteristics of PDBPyBT (top) and PDBTz (bottom) blade-coated from p-xylene, with direction of the bias sweep noted with red arrows.

PDBPyBT blade-coated from p-xylene had an average μ_e of 4.4×10^{-4} $cm^2V^{-1}s^{-1}$, while PDBTz deposited under the same conditions had an average μ_e of 2.2×10^{-4} $cm^2V^{-1}s^{-1}$; both these values are two orders of magnitude below that seen for PDBPyBTz. OFET devices fabricated with both PDBPyBTz and PDBTz exhibited severe hysteresis, as can be seen in the transfer curves (Figure 2-24, Figure 2-25). The changes in the device performance with each consecutive sweep of the gate bias was similar for both PDBPyBT and PDBTz.

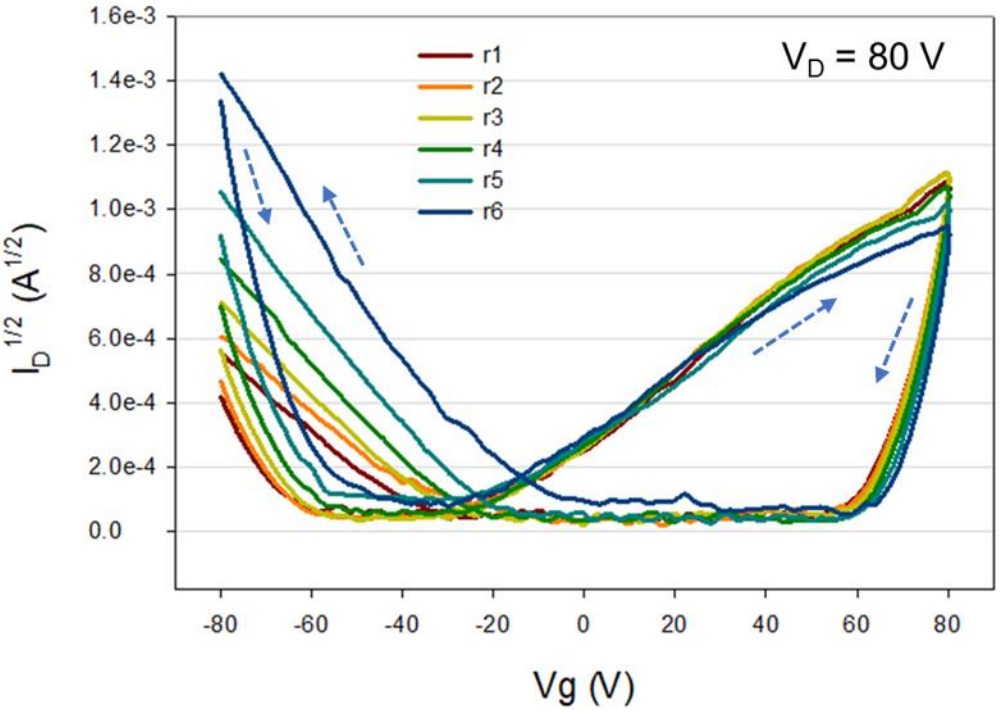

Figure 2-26 Example bias effects shown for six consecutive gate bias sweeps of an OFET device with PDBPyBT blade-coated from p-xylene. The direction of the voltage sweep is indicated with blue arrows.

The bias effects can be seen in Figure 2-26, in which the hole current increases with each consecutive cycle with visibly obvious increases in the slope of the $I_D^{1/2}$ curve (from which mobility is extracted). The hole-current V_T shifts in an increasingly positive direction with each potential sweep in the direction of gate-bias. Conversely, the electron current decreases with each potential sweep, but this change in current is much smaller than that seen in the hole current. These bias effects likely indicate the trapping of electron charges (Figure 2-27), as it is like the charge-trapping effects described by Okachi *et. al.*[63,64]

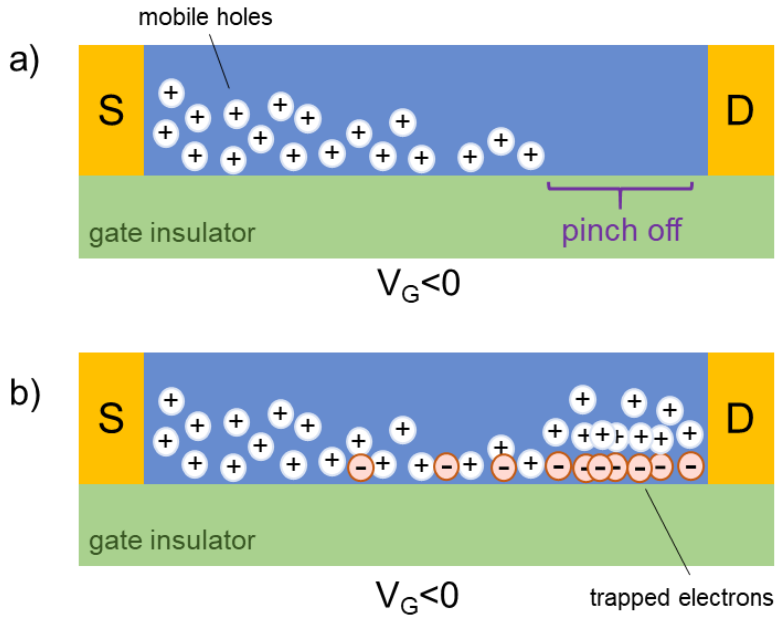

Figure 2-27 a) Distribution of induced mobile holes along the active channel in a non-ideal transistor [a typical OFET] under a negative gate bias in the saturation regime during the first potential sweep [before any electrons are injected]. b) the same device in a subsequent potential sweep under negative gate bias, where trapped electrons [injected while device was under positive gate bias] increase the number of injected holes to satisfy charge neutrality. Figure adapted from reference [64].

In the first potential sweep starting at a negative gate bias, only holes are present as the mobile charge carriers until the potential is swept past $V_G = 0$ and under positive gate bias, when electrons are then injected as the majority charge carriers. Electron traps present in the active channel effectively dope the channel and cause non-ideal transistor characteristics as excess mobile holes are then injected to maintain charge neutrality. The current limitations normally present due to the pinch-off point are further reduced with each potential sweep (Figure 2-27b), further increasing the measured drain current. These effects would explain the increasing hole current and the increasingly positive shifts of V_T for this hole current with each potential sweep. For these reasons the hole mobilities were not extracted for PDBPyBT and PDBTz devices (denoted by the asterisks in Table 2-3), as

the discrepancies of the V_T across the active channel violates the assumptions of the Schockley equation, which precludes reliable hole mobility extraction.[82,132]

It is interesting that the polymer with the highest estimated frontier energy levels (and hence the least efficient electron injection with Au contacts) (Figure 2-18) was the only polymer that demonstrated solely n-channel transport. As all the devices in this study were fabricated simultaneously under the same conditions, it is speculated that hole-traps specific to PDBPyBTz are the source of the unipolar charge transport. Bithiazole has been reported to form complexes with Lewis acids[133] and it is possible that such interactions may be occurring with the BTz moieties in PDBPyBTz and the hole charge carriers, effectively blocking hole transport.

2.3.4 Thin Film Morphology and Microstructure

The surface morphologies of PDBPyBTz, PDBTz, and PDBPyBT films blade-coated onto OTS-modified Si-substrates were characterized using tapping-mode atomic force microscopy (AFM). Non-annealed films blade-coated from both p-xylene and $CHCl_3$ solutions of PDBPyBTz appear to exhibit similar granular morphologies (Figure 2-28). The similarity in the surface morphologies is consistent with the similarity in OFET device performance parameters observed between films cast from the two solvents, as film morphology is known to have a profound influence on charge transport properties.[134–136] Upon annealing, the PDBPyBTz film cast from p-xylene forms a more interconnected structure, whereas the film coated from chloroform had no discernable morphology (apart from what is presumably deposited aggregates).

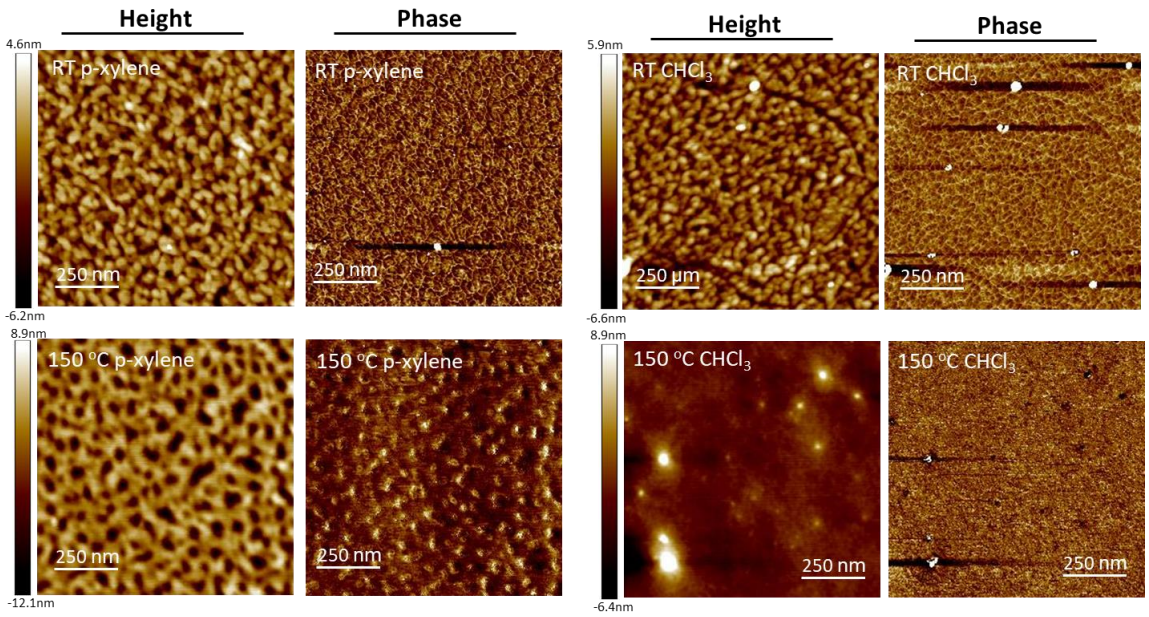

Figure 2-28 AFM images of PDBPyBTz devices blade-coated from p-xylene (left) and $CHCl_3$ (right) onto OTS-18 modified Si/SiO_2 substrates. Pristine substrates are shown in the top row, while those annealed at 150 °C for 30 minutes are shown in the bottom row.[9]

AFM images of pristine PDBPyBT and PDBTz devices blade-coated from p-xylene can be seen in Figure 2-28. The PDBTz film appears to have small fibrous structures.

[9] Images taken by Dr. Michael McBride

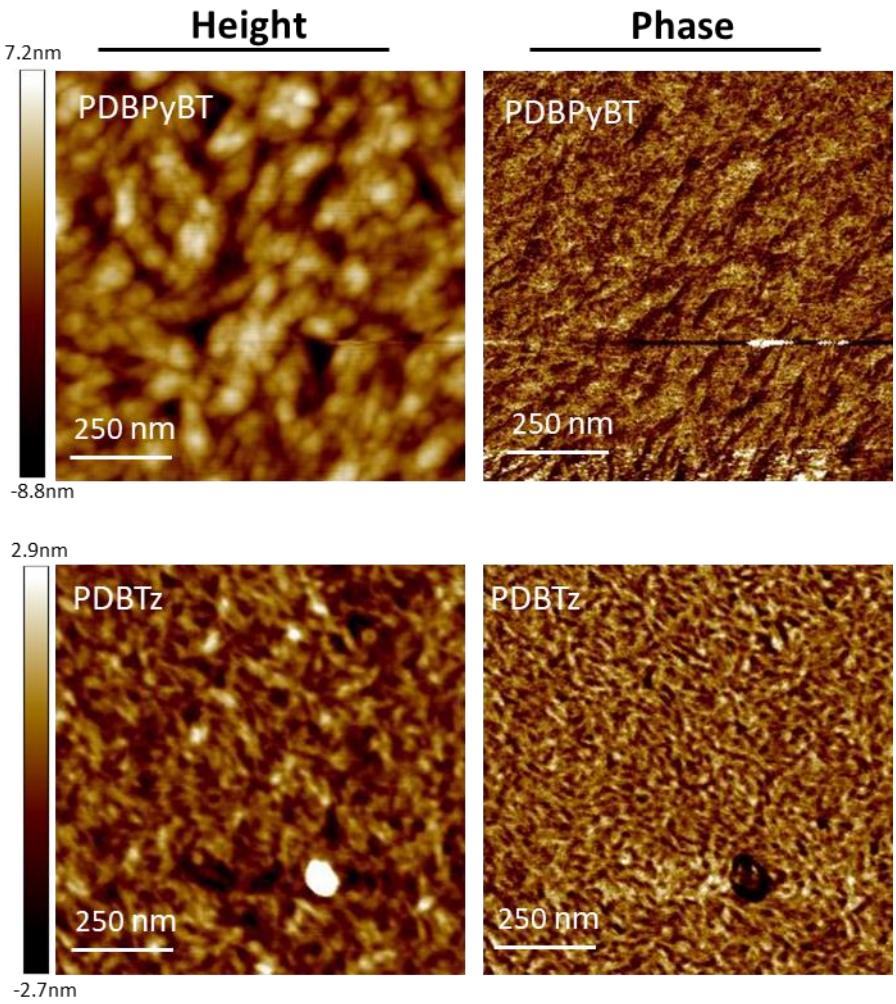

Figure 2-29 AFM images of pristine PDBPyBT (top row) and PDBTz (bottom row) devices blade-coated from p-xylene onto OTS-18 coated substrates.[10]

[10] Images taken by Dr. Michael McBride

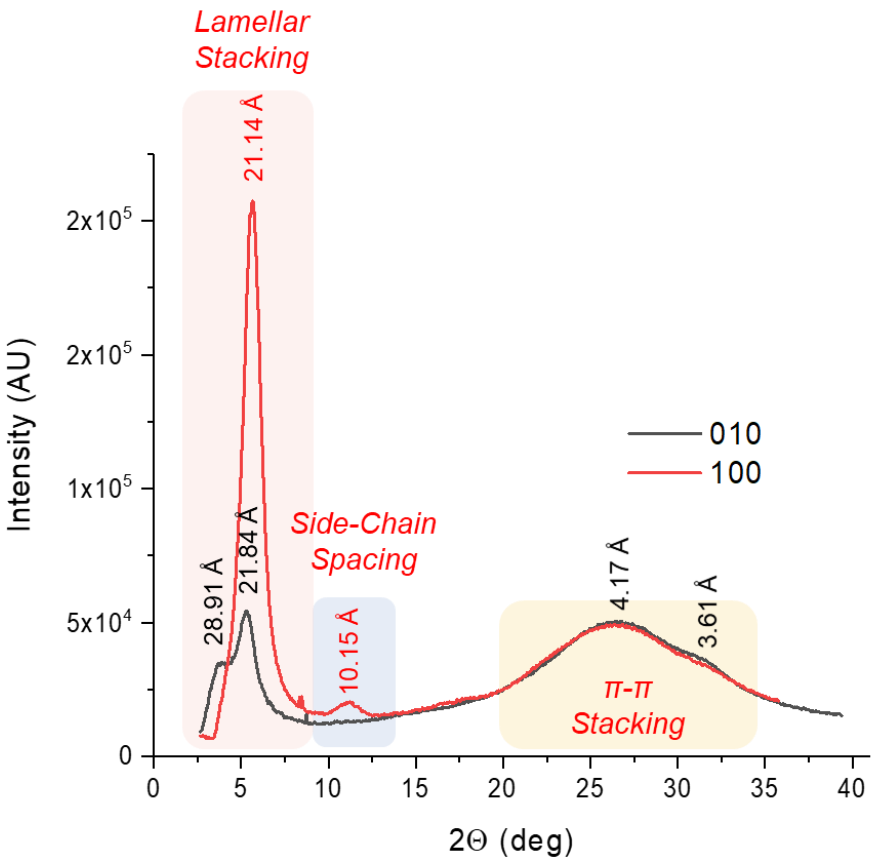

Figure 2-30 GIWAXS line cut patterns of blade-coated PDBPyBTz thin films on OTS-modified Si/SiO_2 substrates.

To investigate PDBPyBTz chain packing, we carried out two-dimensional grazing-incidence wide-angle X-ray scattering (2D-GIWAXS) on blade-coated films cast from p-xylene onto OTS-modified Si substrates (300 nm SiO_2 dielectric on heavily p-doped Si) (Figure 2-30; x-ray scattering patterns shown in Figure A-14). An isotropic ring can be observed at $2\theta = \sim 25^o$ corresponding to a d-spacing of 0.417 nm (4.17 Å), which is on the order typical of π-π stacking distances. The scattering intensities of this ring are similar in magnitude in both the [h00] and [0k0] directions. The well-defined diffraction peak at $2\theta = \sim 6^o$ corresponding to a d-spacing of 2.11 nm (21.1 Å) is attributed to highly ordered lamellar d-spacing between the polymer chains and is of higher intensity in the [h00]

direction than the [0k0] direction. The [200] peak at $2\theta = \sim 11^{o}$ indicates a higher order of lamellar spacing between the 2-octyldodecyl side-chains separating the polymer chains. Herman's orientation parameter was calculated to quantify the orientation distribution of the first-order lamellar stacking peak ([100]) and resulted in an S value of 0.46, indicating a mainly edge-on orientation.[137] Such an edge-on orientation is conducive to in-plane charge-transport mobilities, such as those measured in OFET devices.[105]

2.4 Summary and Conclusions

A semiconducting polymer, PDBPyBTz, was synthesized using the all-acceptor design strategy using Stille microwave copolymerization of the electron deficient 2,2'-bithiazole and bispyridinyl diketopyrrolopyrrole moieties. A high electron affinity of 3.87 eV was estimated from electrochemical potentials, which is promising for stable n-channel OFET device operation. Spectral properties include a low optical bandgap of 1.47 eV and a λ_{max} of 656 nm for the material in thin-film form. BGBC devices fabricated using blade-coated PDBPyBTz active layers demonstrated unipolar n-channel charge transport, with electron mobilities reaching 0.02 $cm^2V^{-1}s^{-1}$. That the IP and EA values of PDBPyBTz were lower (which corresponds to frontier levels higher in energy) in comparison with the analogous PDBPyBT and PDBTz copolymers comprised of more electron-rich monomers was a surprising result, which highlights the need to consider orbital parity and wavefunction distribution between component units in polymeric semiconductors in determining structure-property relationships of product materials and compatibility between candidate monomer pairs. It remains unclear why PDBPyBTz exhibited unipolar n-channel charge transport while the analogous PDBPyBT and PDBTz had ambipolar charge transport despite both having lower frontier energy levels than PDBPyBTz, but

further investigation into the nature of the charge traps present in PDBPyBT films would likely clarify these surprising results.

CHAPTER 3. NANOFIBER GROWTH OF NAPTHALENE-DIIMIDE POLYMERIC SEMICONDUCTORS IN BLADE-COATED THIN FILMS

3.1 Introduction[11]

One of the main drivers for the pursuit of organic electronics is the solution-processability of the active component materials, which has the potential to reduce manufacturing costs, enable large-area fabrication processes, and increase the variety of suitable substrates relative to their inorganic counterparts.[5,138–141] Solution deposition techniques include inkjet printing, spin-coating[142–145], brush-painting[146], dip-coating[147,148], and blade-coating[149–151], among others. The deposition method has a profound influence on the morphology and alignment of semiconducting polymers within thin films, and hence the charge transport characteristics of the devices that are produced.[152–154] Understanding the relationships between processing, morphology, and the resulting OFET performance of a polymer and how it relates to the molecular structure is of critical importance in the improvement of both the performance and reproducibility of devices.[135,155–157]

The most commonly-used laboratory method of depositing polymer solutions for thin-films is spin-coating however this method is wasteful of materials and not amenable to commercial-scale large-area deposition of homogenous films, and more efficient deposition strategies are needed for industrial-scale applications.[154] In contrast, the blade-

[11] Reproduced in part from Yuan, Z.; Buckley, C.; Thomas, S.; Zhang, G.; Bargigia, I.; Wang, G.; Fu, B.; Silva, C.; Bredas, J. L.; Reichmanis, E. *Macromolecules* 2018, *51*, 7320-7328. Copyright 2018, American Chemical Society.

coating method is not only more efficient in the use of materials but is also more easily scaled-up from laboratory optimization to high-throughput and large-area processing.[5,140,158,159] For these reasons, blade-coating was chosen as the processing technique for evaluating the mobilities in our studies of polymeric semiconductors for n-channel OFET devices.

The blade-coating process itself is simple, consisting of a blade dragging a polymer solution over a substrate surface, leaving a thin layer of solution which dries to leave a polymeric thin film as the solvent evaporates (Figure 3-1).

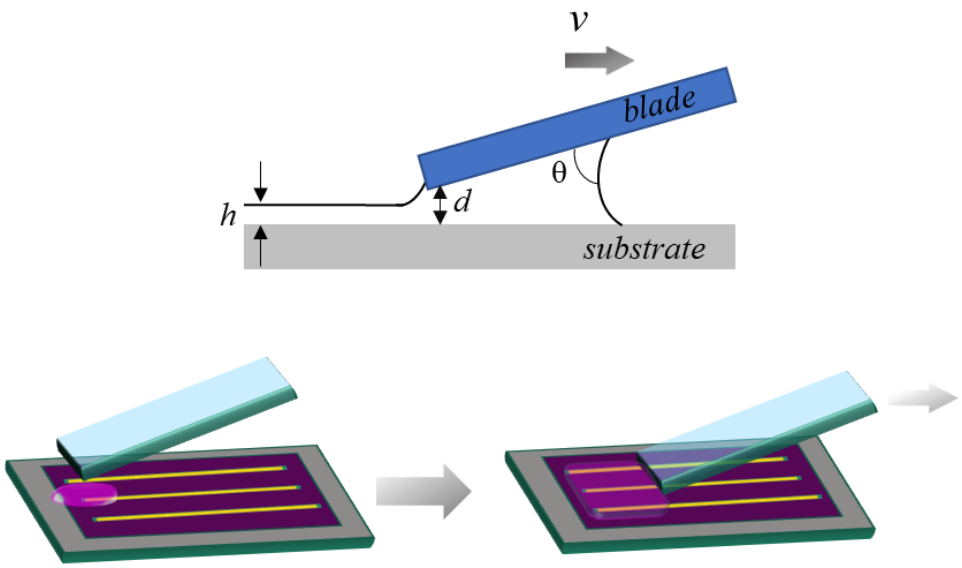

Figure 3-1 Schematic of the blade-coating process, with relevant parameters defined at top

The thickness of the film (*h*, Figure 3-1) is determined by the velocity (*v*) of the blade. At lower velocities, the polymer solution is concentrated at the blade contact as the solvent evaporates at the surface of the meniscus (known as the evaporation regime). At faster velocities, the polymer solution is dragged out by viscous forces and dried *after* the

film is formed (known as the Landau-Levich regime).[151,160] The final film structure is determined by the drying conditions, which in turn is a factor of the solvent and the substrate temperature.

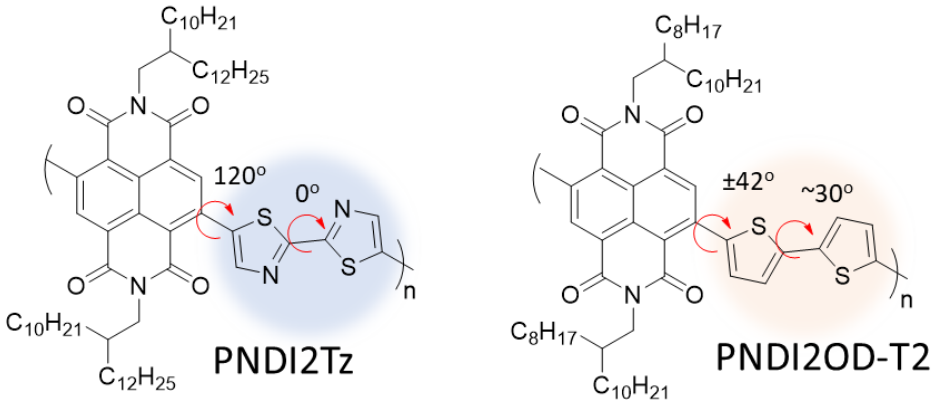

Figure 3-2 Molecular structures of PNDI2Tz (left) and PNDI2OD-T2 (right), with their reported backbone torsional angles noted in red.

While preparing devices to study the OFET characteristics of PNDI2Tz (Figure 3-2), interesting morphological features were noticed on blade-coated films deposited on heated substrates. Additionally, it was noted that the highest mobility PNDI2Tz devices were on octadecyltrichlorosilane (OTS)-modified substrates. This chapter will describe investigations into observed nanofiber formation of the PNDI2Tz polymer (synthesized by Dr. Zhibo Yuan and characterized as part of a joint collaboration with the author).[125,161] Similar processing studies were performed in parallel on the structurally similar PNDI2OD-T2 (synthesized by Carolyn Buckley) to look for similarities in film-forming behavior.

3.2 Experimental

3.2.1 Materials and Methods

All reagents and solvents were reagent-grade, purchased from commercial sources and were used as received. Chloroform, dichloromethane, toluene, *p*-xylene (PX), isopropanol (IPA), tetrahydrofuran (THF), dimethylformamide (DMF), chlorobenzene, 1,2-o-dichlorobenzene (*o*-DCB), 1,2,4-trichlorobenzene (TCB) were purchased as anhydrous-grade solvents from Sigma-Aldrich. THF was purified in an Mbraun solvent purification system (MB-SPS-800-AUTO). 2-Bromothiazole was purchased from Scientific Matrix. Tetrabutylammonium bromide (*n*-Bu_4NBr), *n*,*n*-diisopropylethylamine (DIPEA), diisopropylamine (DIPA), palladium(II) acetate ($Pd(OAc)_2$), tris(dibenzylideneacetone)-dipalladium(0) ($Pd_2(dba)_3$, tri(*o*-tolyl)phosphine (P-(*o*-tolyl)$_3$), sodium diethyldithiocarbamate, and tetra-*n*-butylamminium hexafluorophosphate ([*n*-$Bu_4N]^+[PF_6]^-$), and ethylene glycol (EG) were purchased from Sigma-Aldrich. *N*-octadecyltrichlorosilane (OTS), phenyltrichlorosilane (PTS), and hexamethyldisilazane (HMDS) was purchased from Gelest, Inc. Silica gel was purchased from Sorbent Technologies (Premium Rf^{TM}, porosity: 60 Å; particle size: 40-75 μm). Anhydrous chlorobenzene was degassed prior to use via a freeze-pump-thaw process.

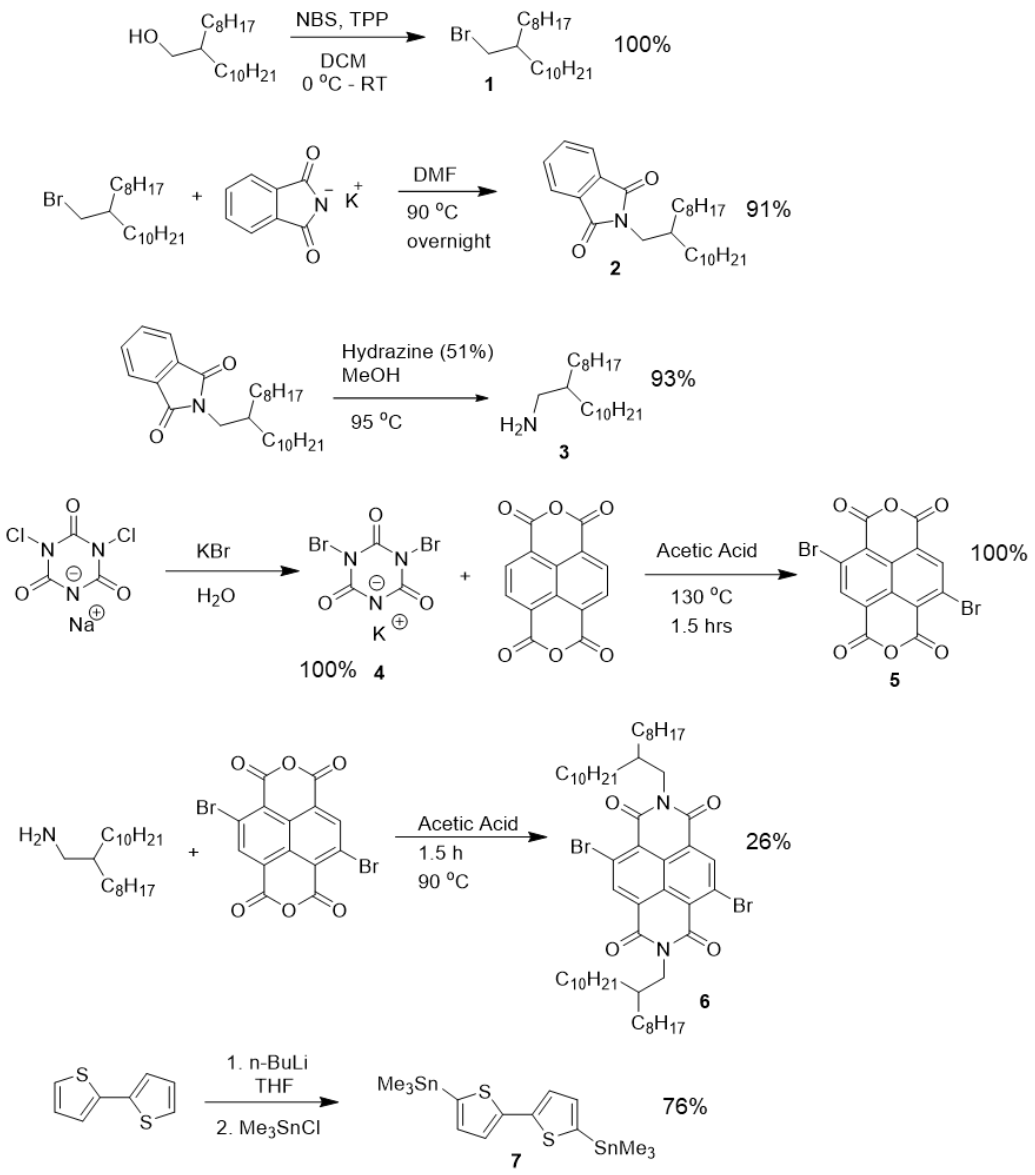

Figure 3-3 Synthetic scheme for the monomeric components of PNDI2OD-T2

3.2.1.1 Synthesis of 9-(bromomethyl)nonadecane (**1**)

Triphenylphosphine (21.06 g, 80.3 mmol) was dissolved in DCM (60 mL) at room temperature under N_2. 2-Octyldodecanol (20 g, 66.9 mmol) was added via syringe, and the reaction mix brought to 0 °C. N-bromosuccinimide (14.30 g, 80.3 mmol) was added slowly to the reaction mix, with care taken to not allow the reaction temperature to exceed 30 °C.

After addition was complete, the reaction was allowed to continue to react at 0 ^{o}C for 30 minutes before warming to RT. The solvents were then removed, and the orange residue diluted with hexanes, and passed through a silica gel plug which was then washed with more hexanes. The solvent was then removed to give a colorless oil (full conversion). ^{1}H NMR ($CDCl_3$, 300 MHz) δ 3.45 (d, J = 4.7 Hz, 2H), 1.59 (m, 1H), 1.27 (s, 32H), 0.88 (t, J = 6.7 Hz, 6H). ^{1}H NMR spectrum matches the literature report.[162] The spectra can be found in Appendix (Figure A-10).

3.2.1.2 Synthesis of 2-(2-ocyldodecyl)isoindoline-1,3-dione (**2**)

9-(bromomethyl)nonadecane (10.0 g, 27.6 mmol) and potassium phthalimide (6.14 g, 33.1 mmol) were added to 30 mL dimethylformamide under N_2 and stirred overnight at 100 ^{o}C. The reaction mix was then allowed to cool to RT and poured into dH_2O and transferred to a separatory funnel. The product was extracted with DCM (3 x 10 mL), washed with 0.2 M KOH (2 x 25 mL), dH_2O (8 x 25 mL), and saturated ammonium chloride (2 x 25 mL). The collected organic fractions were dried over $MgSO_4$ and purified via column chromatography (silica gel, DCM eluent) to obtain the product as a light yellow oil (91% yield). ^{1}H NMR ($CDCl_3$, 300 MHz) δ 7.87-7.77 (m, 2H), 7.75-7.64 (m, 2H), 3.56 (d, J = 7.3 Hz, 2H), 1.87 (s, 1H), 1.23 (s, 32 H), 0.86 (t, J = 6.7 Hz, 6H). ^{1}H NMR spectrum matches the literature report.[162] The spectra can be found in Appendix (Figure A-9).

3.2.1.3 Synthesis of 2-octyldodecylamine (**3**)

N-(2-decyltetradecyl) phthalimide (14.99 g, 35 mmol), hydrazine hydrate (5.13 mL 51%, 105 mmol), and 100 mL of MeOH were stirred at 95 ^{o}C and monitored by TLC. After the disappearance of the starting imide, the methanol was removed and the residue diluted

with 100 mL DCM and washed with 10% KOH (2 x 50 mL). Aqueous layers were combined and extracted with DCM (3 x 20 mL) and dried over $MgSO_4$. The removal of solvents afforded a yellow oil which was used in the next synthesis without further purification (93% yield). ^{1}H NMR ($CDCl_3$, 300 MHz) δ 2.60 (d, J = 3.5 Hz, 1H), 1.26 (s, 36H), 0.88 (t, J = 6.7 Hz, 3H). ^{1}H NMR spectrum matches the literature report.[162] Spectra in Appendix (Figure A-11).

3.2.1.4 Synthesis of Potassium Dibromoisocyanurate (**4**)

Sodium dichloroisocyanurate dihydrate (66 g, 230 mmol) was dissolved in 600 mL of dH_2O. In a separate flask, potassium bromide (71.4 g, 609 mmol) was dissolved in 1500 mL dH_2O. The dichloroisocyanurate solution was then added to the solution of potassium bromide, and mechanically stirred for 15 minutes (caution: solution becomes very viscous as white precipitate forms). The reaction mix was then filtered, the white precipitates washed with dH_2O, and dried under vacuum overnight. The product was used in the next step with no characterization.

3.2.1.5 Synthesis of 2,6-dibromo-1,4,5,8-tetracarboxynaphthalenediimide (**5**)

Naphthalene dianhydride (9.99 g, 37.3 mmol) and potassium dibromoisocyanurate (26.65 g, 82 mmol) was added to 300 mL sulfuric acid (12 N) and brought to 85 ^{o}C under N_2 to react overnight. The reaction mix was allowed to cool, poured into ice water and then filtered, washed with dH_2O, and dried over high vac to yield 19.12 g of a yellow solid (full conversion). ^{1}H NMR (d_6-DMSO, 400 MHz) Spectra in Appendix (Figure A-12).

3.2.1.6 Synthesis of C_8C_{10}-Alkylated NDI (**6**)

2-octyldodecylamine (18.21 g, 61.19 mmol) and the dibrominated naphthalene dianhydride (6.5 g, 15.29 mmol) was added to 200 mL acetic acid (12 N) and refluxed at 130 ^{o}C for 1.5 hours. After cooling to RT, the reaction mix was poured into cold methanol and filtered, then washed with MeOH and dried under high vac to give bright red solids. The product was purified via column chromatography (silica gel, 40 % DCM/Hexanes) to yield yellow solids (26% yield). Spectra in Appendix (Figure A-13). ^{1}H NMR ($CDCl_3$, 400 MHz) δ 8.99 (s, 2H), 4.14 (d, J = 7.3 Hz, 4H), 1.97 (m, 2H), 1.40 -1.17 (m, 64 H), 0.86 (m, 12 H). ^{1}H NMR spectrum matches the literature report.[163]

3.2.1.7 Synthesis of 5,5'-bis(trimethylstannyl)-2,2'-bithiophene (**7**)

2,2'-Bithiophene (2 g, 12.02 mmol) was added to anhydrous THF (100 mL) at room temperature under N_2 and allowed to stir for 15 minutes to dissolve before cooling to -78 ^{o}C. A solution of n-BuLi (10.56 mL 2.5 M hexanes, 26.4 mmol) was added via syringe at -78 ^{o}C, then the reaction flask was allowed to reach room temperature and stirred at RT for 1 hour. The reaction was again cooled to 78 ^{o}C, and solution of trimethyltin chloride (5.27 g, 26.4 mmol, in 10 mL anhydrous THF) was added, then the reaction mix was allowed to warm to RT. The reaction was stirred for 5 hours at RT, then the reaction mix was diluted with EtOAc, washed with d(H_2O), then washed with brine, dried over $MgSO_4$, filtered, and the solvent removed. Recrystallization in methanol yielded 4.49 g of light-yellow crystals (76 % yield). ^{1}H NMR (300 MHz, $CDCl_3$) δ 7.28 (d, J = 5.3 Hz, 2H), 7.09 (d, J = 3.4 Hz, 2H), 0.38 (s, 18 H). ^{1}H NMR spectrum agrees with literature data.[163] Spectra in Appendix (Figure A-8).

3.2.1.8 Polymerization of PNDI2OD-T2

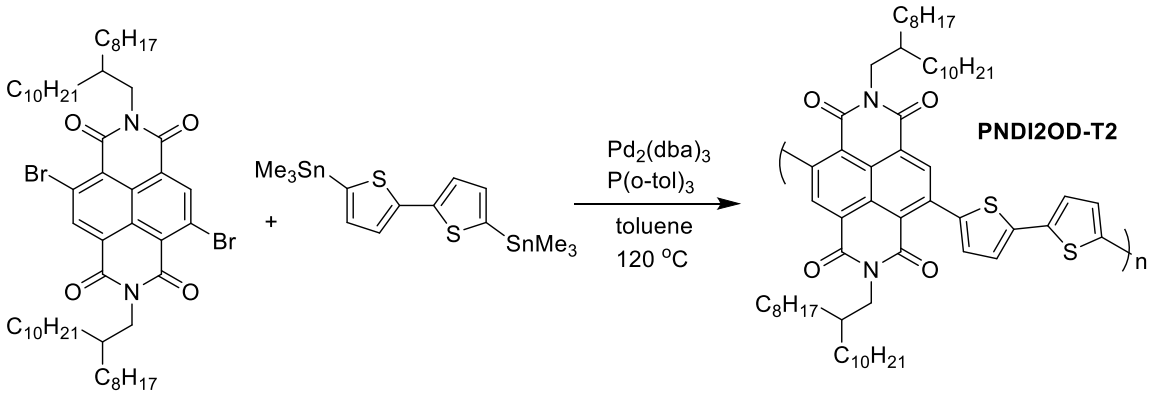

Figure 3-4 Reaction scheme for the polymerization of PNDI2OD-T2

A Stille polymerization was performed using a custom-designed continuous flow chemistry apparatus[164] for increased control of molecular weight and minimization of polydispersity. The system consists of a KDS-200 Legacy syringe pump, ISCO 260D high-pressure syringe pump system, a perfluoroalkoxy (PFA) tubular reactor of 20 mL immersed in a heated oil bath, an Eldex Optos model 1 high pressure liquid metering pump, and a 4-way valve. The entire flow system was pressurized with a back-pressure regulator of 40 psi from Upchurch Scientific.

A microwave reaction vial was charged with 5,5'-Bis(trimethylstannyl)-2,2'-bithiophene (99.9mg, 0.2 mmol) and N,N'-bis(2-octyldodecyl)-2,6-dibromonaphthalene-1,4,5,8-bis(dicarboximide) (200 mg, 0.2 mmol) and transferred to an N_2-filled glovebox. A separate microwave reaction vial was then equipped with $Pd_2(dba)_3$ (5.58 mg, 3 mol%) and $p(o\text{-}Tol)_3$ (7.42 mg, 12 mol%). Each vial was then equipped with a magnetic stir bar and 5 mL chlorobenzene and allowed to stir for 10 minutes to dissolve under N_2 atmosphere. The catalyst and monomer solutions were then placed in separate syringes, and quickly transferred to the flow-reactor apparatus. The reaction was then set to flow at 2 mL/min in a pre-heated oil bath at 120 ^oC for a total reaction time of 45 minutes. The

reaction mixture was then precipitated in MeOH, and blue solids were filtered into an extraction thimble and the polymer purified via successive soxhlet extractions in MeOH, acetone, hexanes (24 hours each) with chloroform used as the final extraction solvent. The chloroform solution was concentrated and precipitated again in methanol. Vacuum filtration collected a blue solid. M_n 51,095, M_w 67,071, $Đ$ 1.3.

3.2.1.9 Molecular Weight Distribution

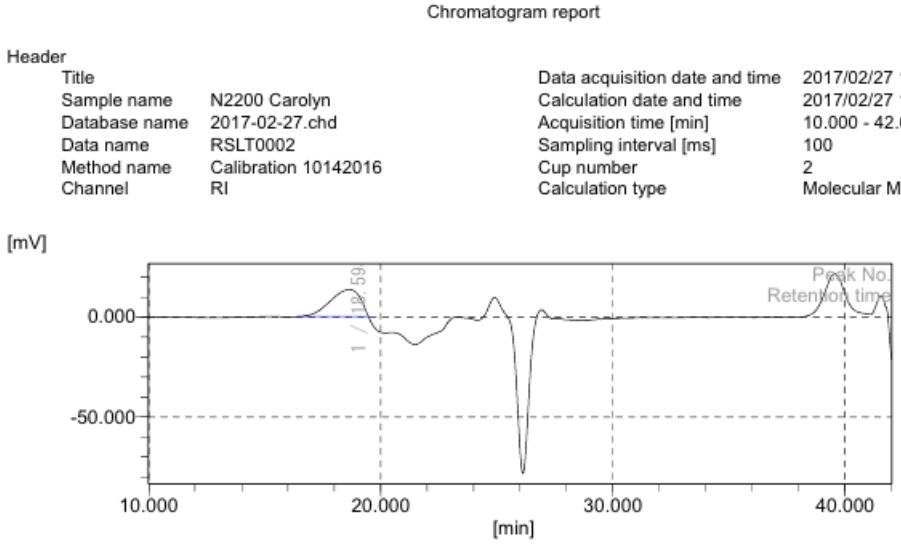

Figure 3-5 GPC characterization of PNDI2OD-T2 in 1,3,5-trichlorobenzene at 130 ^oC[12]

3.2.2 Preparation of Substrates and Processing of Thin Films

[12] GPC done by Dr. Bing Xu

Glass substrates for thin-film UV-*vis* analysis, *p*-doped Si wafers for GIWAXs studies, and OFET device substrates were passivated using identical procedures, with the exception of the OFET devices first being sonicated in a toluene bath for 60 minutes to remove residual photoresists. Passivated substrates were prepared by sequential rinsing in acetone, MeOH, IPA, then dried under a flow of N_2 prior to UV-ozone treatment (Novascan® PSD-VU – Benchtop UV-Ozone Cleaner). The slides were then immediately transferred to anhydrous surface modifier (OTS, PTS, HMDS) solutions (0.1% v/v in toluene) under N_2 atmosphere for 14 hours at room temperature. The substrates were then removed from the surface modifier solutions and sonicated in fresh toluene for 30 minutes (Branson® Ultrasonic Bath, 230 V_{ac}, 50 Hz), followed by sequential rinsing in acetone, MeOH, and IPA, followed by drying under a stream of compressed air (filtered to remove oil and moisture). Contact angle measurements on surface-modified and pristine substrates were measured with a Ramé-Hart Goniometer (Model 200), using 5 μL distilled H_2O and ethylene glycol (EG) individually measured at different sites on the substrates. Final surface free energies (γ_s) were calculated according to the Owens-Wendt method.[165]

Highly *n*-doped (100) silicon wafers with 300 nm thermally grown oxide gate dielectric films were used as substrates to prepare bottom-gate/bottom-contact (BGBC) OFET devices. Au source and drain contacts (50 nm Au, 3 nm Cr adhesion layer) with fixed channel dimensions (50 μm in length, 2 mm in width) were deposited via *e*-beam evaporation using a photolithography lift-off process. The devices were sonicated in toluene for 60 minutes to remove residual photoresist before the surfaces were passivated using the procedures described below. The capacitances of the dielectric layers were measured using an Agilent 4284A Precision LCR meter.

Thin films for OFET devices and GIWAXs characterization were blade-coated onto the substrates using an in-house blade coater equipped with a glass blade and temperature-controlled heating stage. Blade coating speeds were programmed and controlled by a DMX-UMD 23 motor from Arcus Technology. Blade height was controlled to be within a range of 45-55 μm, and blade angle was set to be $8^{o} \pm 1^{o}$. Polymer solutions were dissolved in *p*-xylene or chloroform (5-10 mg/mL) to prepare the active ink. Substrates were heated to 45 ^{o}C for the coating of chloroform polymer solutions, and to 100 ^{o}C for *p*-xylene polymer solutions. 5-10 μL of active ink polymer solution was transferred to the heated substrates (1.5 cm x 1.5 cm) immediately prior to blade-coating. Films were placed in a vacuum oven at 55 ^{o}C overnight to remove residual solvents. The morphology of the films were analyzed using atomic force microscopy (AFM, Bruker Dimension Icon® Atomic Force Microscope with ScanAsyst, MIkromasch® AFM probe tips, 3.5 N/m, 135 kHz), scanning electron microscopy (SEM, Hitachi SU8230 FE-SEM), and grazing incident X-ray scattering (GIWAXS, Beamline 11-3 at Stanford Linear Accelerator Center National Accelerator Laboratory, Stanford University).

3.3 Results and Discussion

3.3.1 PNDI2Tz and PNDI2OD-T2

Gel permeation chromatography with polystyrene standards was used to determine the molecular weights of the polymers used in this study. PNDI2Tz[13] was found to have an

[13] Synthesis and thermal characterization of PNDI2Tz was performed by Dr. Zhibo Yuan. Details can be found in the cited references.

M_n of 49.3 kD with a polydispersity (PDI, $Đ$) of 3.3.[125,161] PNDI2OD-T2 was similarly found to have an M_n of 53 kD and a $Đ$ of 1.3 (Figure 3-5).

Thermogravimetric analysis of PNDI2Tz revealed a decomposition temperature of 427 ^oC.[125] Differential scanning calorimetry revealed a T_g of 63.71 ^oC, however no other thermal transitions were seen between 0-250 ^oC.[125,161] Interestingly, PNDI2OD-T2 was reported to have no thermal transitions up to 300 ^oC.[105] It is important to note that a measured T_g is not a physical constant of a material but is dependent on experimental parameters such as heating/cooling rates and the processing history of the particular sample.[166] The reported DSC scans of PNDI2Tz[125] and PNDI2OD-T2[105] that are being compared were both run under the same conditions (notably at the same scan rate of 10 ^oC/min), however it is likely that the observed differences are due to different degrees of crystallinity between the two samples. More crystalline polymer samples may not have enough amorphous content to generate detectable changes in heat capacity for the T_g to be observed, and hence will appear as not having a T_g.[166] PNDI2Tz thermal analysis was performed after purification, with no intentional processing beforehand. Prior processing of the PNDI2OD-T2 sample used in the reported thermal analysis was not mentioned[105], however the multiple reports on the tendency of PNDI2OD-T2 to form crystalline structures[167,168] leads to the speculation that insufficient amorphous content was the reason for the lack of an observed T_g.

3.3.2 Solution Processing of OFET Devices

Before blade-coating the processed solutions, contact angle measurements were taken on the passivated substrates (Figure 3-7) to determine the surface energies (Figure 3-6).

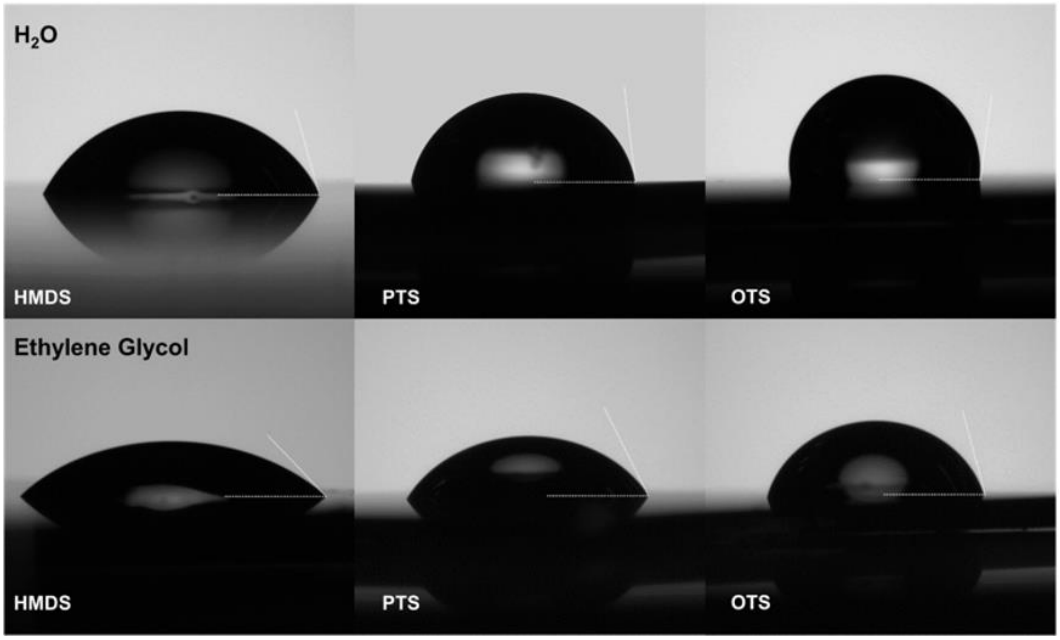

Figure 3-6 Contact-angle measurements on HMDS, PTS, and OTS-passivated surfaces.[14]

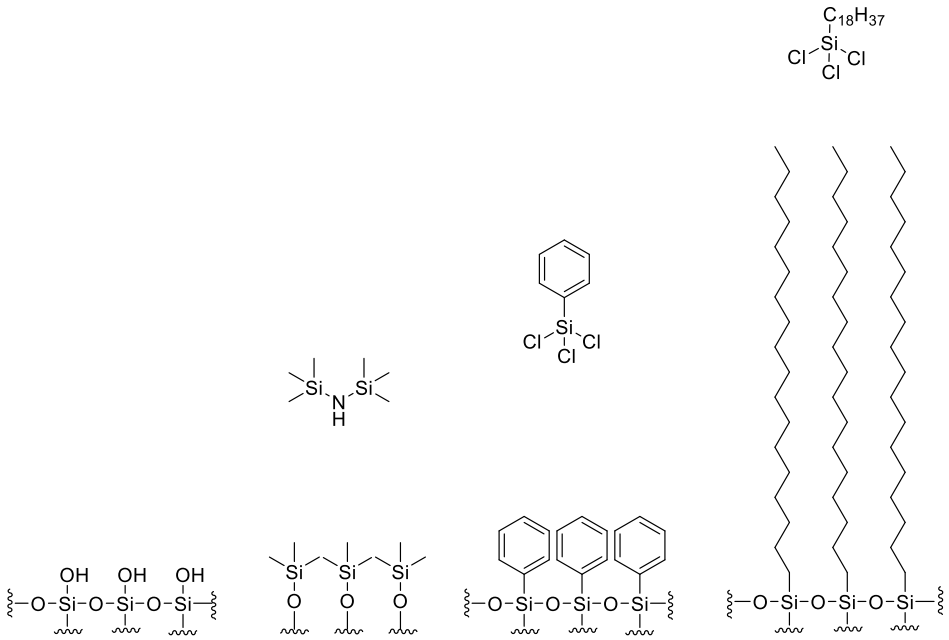

Figure 3-7 Surface modifiers used to passivate the Si/SiO_2 surfaces[169]

Table 3-1 Contact Angle Results with calculated surface energies

Surface Modifier	Water (°)	EG (°)	γ_s_d	γ_s_p	γ_s (mJ/m^2)
HMDS	68.38	48.08	18.68	17.09	35.77
PTS	80.23	57.88	9.75	18.88	28.63
OTS	99.13	74.20	2.01	19.98	21.99

Blade coating the polymer solutions (either PNDI2Tz or PNDI2OD-T2) at room temperature resulted in complete de-wetting on OTS surfaces, and poor film formation on PTS and HMDS surfaces. Complete de-wetting was also observed during attempts to spin-coat the polymer solutions (all surfaces). Polymer thin films were only observed in the blade-coating process when the substrates were heated to elevated temperatures.

The coating stability is determined by the wetting characteristics of the solution on the substrate. For a polymer solution to 'wet' the substrate, the surface tension of the liquid must be lower than the surface energy of the substrate (known as the 'wetting condition'). However, surface tension varies with temperature (Figure 3-8).

[14] Contact angle measurements and calculations done by Dr. Zhibo Yuan

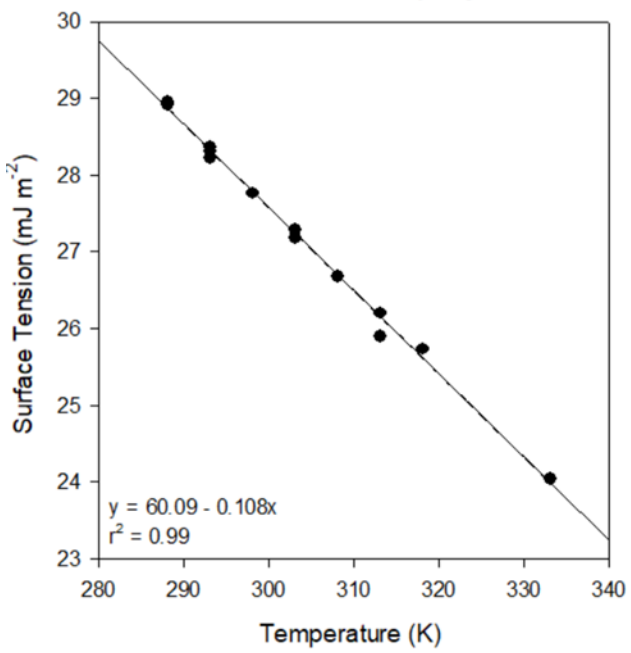

Figure 3-8 Plot of surface tension of p-xylene vs. temperature. Data from [170].

From the plot shown in Figure 3-8, the surface tension of p-xylene at room temperature (298 K) is 27.90 mJ/m^2. Making the simplifying assumptions that the surface tension of the polymer solution is that of p-xylene and that the surface energy of the substrate does not change with temperature, it can be said that the wetting conditions are not met at 298 K for OTS surfaces, which would explain the complete de-wetting. The differences in surface tension between the polymer solutions and the HMDS- and PTS-coated substrates at 298 K would lead to partial de-wetting, and hence poor-quality films. It is likely that the centripetal forces present during the spin-coating process further deteriorated the poorly wetted films, which would explain why no film formation was seen upon spin coating. Adequate film formation on OTS substrates was only observed at temperatures of 100 ^{o}C and above. At this temperature (373 K), the surface tension of p-xylene is 19.81 mJ/m^2, which is just below the surface tension of the OTS-coated substrate (Table 3-1). Coating at temperatures above 100 ^{o}C produced non-homogenous films, as the

solvent evaporated too quickly. While p-xylene has a boiling point of 138 ^{o}C[171], the small amount of polymer solution evaporates quickly due to the relatively large surface area of the drop/film. The speed of evaporation of the solvent in solution-deposited thin films of conjugated polymers has been shown to have a correlation with the crystallinity of the resultant films.[172] In order to balance the time-dependent crystallization of thin-films with the need to wet the substrate, the temperatures used in depositing the thin films did not exceed 100 ^{o}C.

3.3.3 Morphology of Thin Films

Differences in the morphology and molecular orientation of conjugated polymer films upon surface passivation have been reported in the literature, highlighting the sensitivity of thin-film formation on substrate surface chemistry and the effects on charge carrier mobility.[173,174] In poly (2,5-bis(3-dodecylthiophene-2-yl)thieno[3,2-b]thiophene) (PBTTT), substantial increases in the orientational order, size of crystalline terraces, and higher charge carrier mobility was reported upon hydrophobic surface treatment with OTS-8 compared with that observed on bare silicon oxide.[175] Wang *et. al.* reported different microstructures of PBTTT films dip-coated onto bare O_2/plasma-cleaned SiO_2 and base monolayers of PBTTT, which they attributed to the different surface tensions of the substrates.[176] Notably, PBTTT was found to self-assemble into needle-like fibers (thickness 4-6 nm) on the low-energy PBTTT base monolayers, with decreased coating speed leading to increased surface coverage of the initial monolayer and longer nanofiber nuclei of subsequent layers (thickness did not change).[176] In contrast, their later studies of dip-coated films of PNDI2OD-T2 on O_2/plasma-cleaned SiO_2 found the formation of fibrous microstructures to be independent of pulling speed and the presence of a base

monolayer.[177] Considering the similar surface tensions of PBTT and PNDI2OD-T2, it was rationalized that the different microstructural formation patterns under similar processing conditions can be traced to the differences in molecular structure of the polymers (e.g. backbone planarity and alkyl substituents).[177] Changes in the surface energies of substrates results in changes in the growth of polymer film morphology from solution-deposited systems, as the adhesive forces from the substrates compete with the polymer self-assembly process. Bucella *et. al.* later corroborated these results, showing PNDI2OD-T2 films spin-coated from dilute mesitylene solutions showing connected branched aggregate formations on O_2/plasma-treated SiO_2 surfaces and detached, quasi-1D nanodomains on hexamethyldisilazane (HMDS)- treated SiO_2 surfaces.[178] In light of these reports, it was decided to experiment with surface-modified substrates with PNDI2Tz and PNDI2OD-T2.

AFM images of the blade-coated thin films of PNDI2Tz and PNDI2OD-T2 were taken to investigate the surface topologies. The evolution of the thin-film morphology of PNDI2Tz blade-coated onto OTS-coated substrates at increasing blade velocities can be seen in Figure 3-9. At 1 mm/s, no clearly defined morphology can be seen. However, defined morphological features can be observed at higher velocities, with decreasing surface roughness of the films seen when velocities are increased.

At 2 mm/s there is a clearly defined network formation, which appear to be bundles of fibers when looking at the height profile of the film (Figure 3-10). The smallest fiber widths that could be seen on films coated at 2 mm/s are 10 nm, within what are presumably bundles off these fibers of widths varying from 38 nm to 164 nm (Figure 3-11). The height variation of these bundles on the surface of the film is between 1 and 2 nm. The surface

does not appear to change upon annealing, however the surface roughness of the films increased from R_q of 0.836 nm to R_q of 0.990 nm.

At 3 mm/s, finely structured nanofibers can be seen, which appear to again be hierarchically-bundled fibers in the height profile of the film (Figure 3-9, Figure 3-10). The smallest fiber widths that could be seen on PNDI2Tz films coated at 3 mm/s are 2 nm, which again appear to be arranged in bundles of increasing widths on the surface of the film. The widths of the bundles are 6-8 nm on the surface of the film, and interestingly appear more clearly defined that the bundles seen in the films coated at 2 mm/s. It is difficult to determine the lengths of the fibers, as the boundaries (start, end) of each fiber are not clear from the AFM images. Interestingly, the height variation of the surface of the films coated at 3 mm/s appeared to occur in increments of ~0.33 nm (Figure 3-11), with larger heights being multiples of ~0.33 nm. This is suggestive of the stacking of a morphological motif within the thin film. A loss of resolution is seen in the AFM images upon annealing, with an increase in surface roughness from R_q of 0.435 nm to R_q of 0.595 nm.

PNDI2Tz films coated at 4 mm/s on OTS-coated substrates appeared to be a more dense network of fine fibers (Figure 3-9), however specific structural features cannot be seen in the height profiles of the films (Figure 3-10) and the fibers are not as well defined as those seen in the films coated at lower velocities. There appear to be ‘holes’ in the film on the order of 10 nm in the height image of the pristine film, however in the corresponding phase image appears these ‘holes’ appear to be underlayers of more nanofibers (Figure 3-9). A more clearly defined interconnected network formation can be seen on the films

after annealing, with a slight increase in surface roughness from R_q of 1.61 nm to R_q of 1.89 nm.

At 5 mm/s, PNDI2Tz coated onto OTS-modified substrates (Figure 3-12) had consistently poor film formation. Notably, the nanofiber networks seen at lower velocities are not seen in films coated at 5 mm/s, which only show discontinuous coverage of the films.

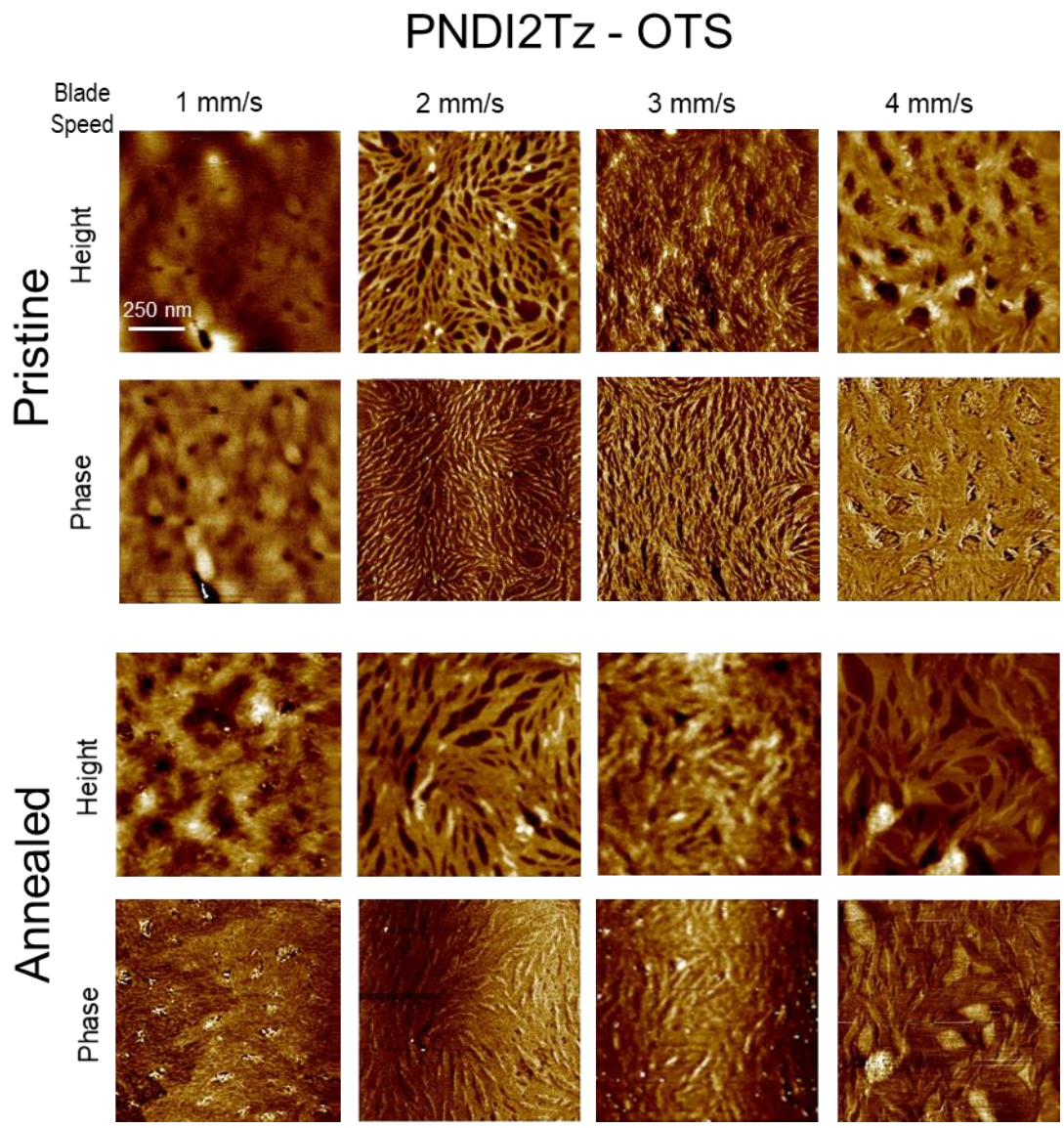

Figure 3-9 AFM images of PNDI2Tz substrates blade-coated onto OTS-coated substrates at increasing velocities.[15] Annealed films were heated to 100 ^{o}C for 30 minutes under N_2.

[15] AFM images taken by undergraduate researchers, including Qianyi "Beth" Qu and Kyle Hamrock

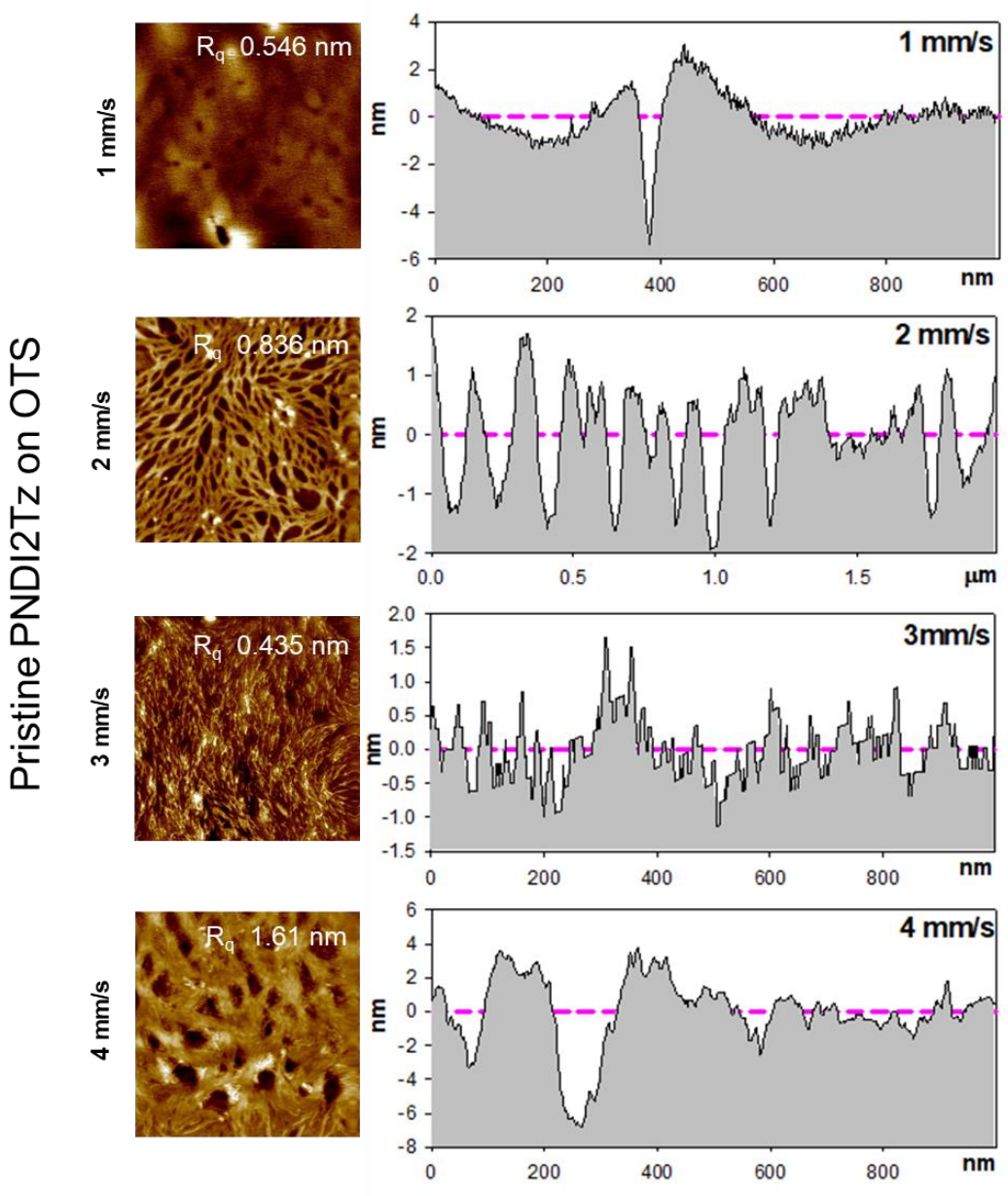

Figure 3-10 Height analysis of PNDI2Tz films blade-coated onto OTS-coated substrates at increasing velocities.

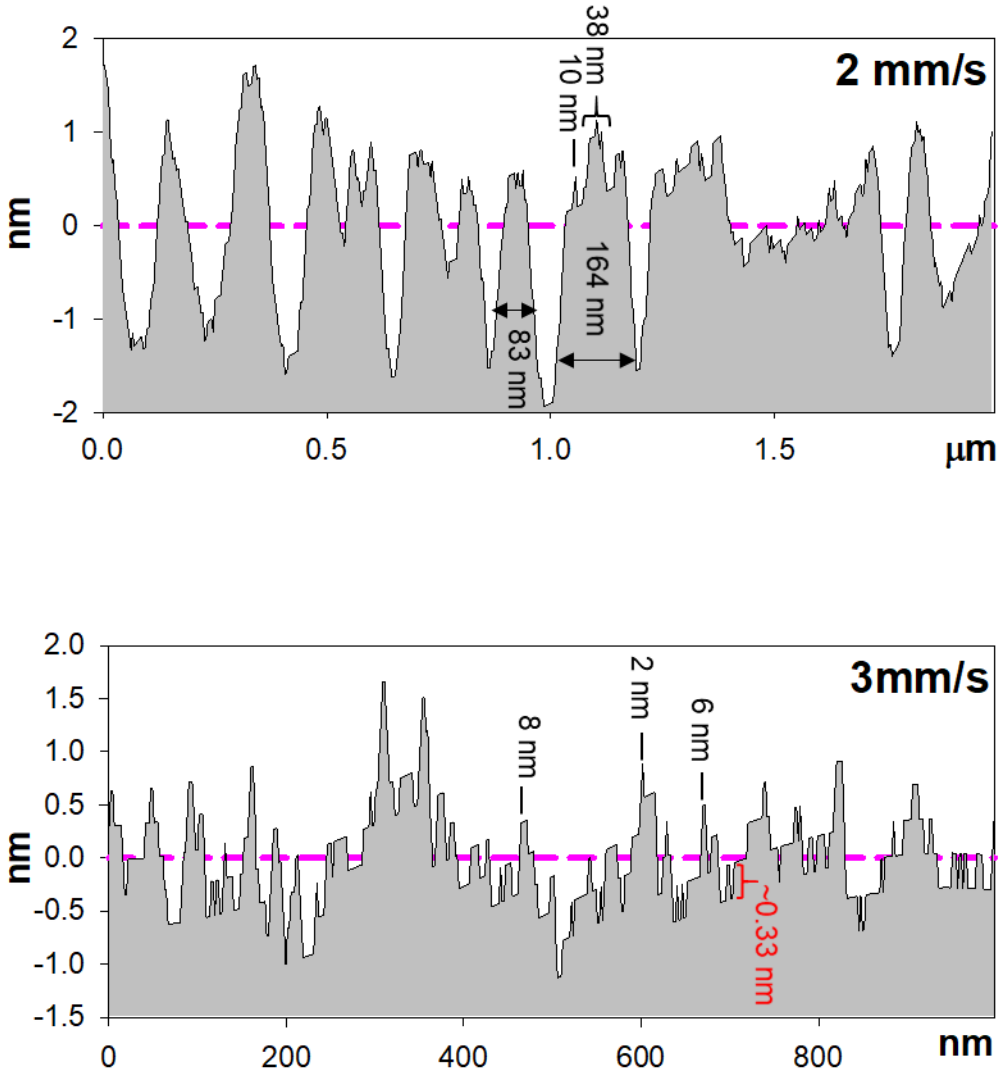

Figure 3-11 Height analysis of pristine PNDI2Tz blade-coated onto OTS-coated substrate at 2 mm/s (top) and 3 mm/s (bottom), with widths of fiber formations shown.

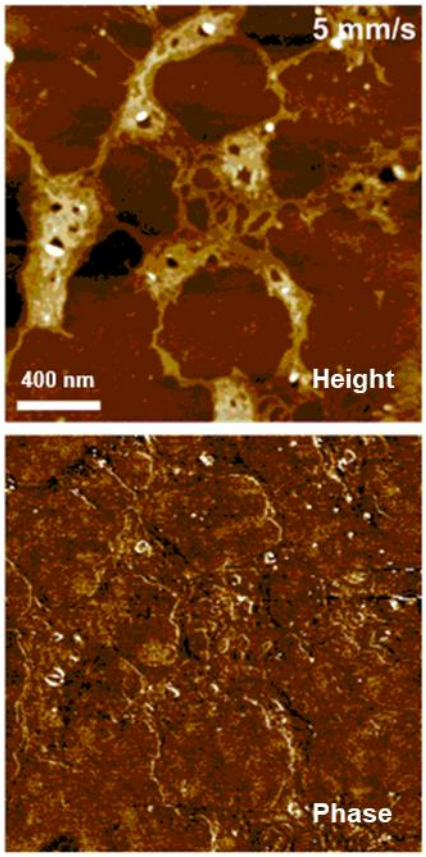

Figure 3-12 AFM images of PNDI2Tz blade-coated onto OTS-modified substrates at 5 mm/s, showing poor film formation.

Less defined structural features were present in the AFM images of PNDI2Tz films blade-coated onto PTS-coated substrates (Figure 3-13). At films coated at 1 mm/s, there are no discernable morphological features, similar to that observed for OTS-coated substrates at the same velocity. At 2 mm/s a network structure can be seen, with the height profile of the film similar to that seen on OTS-coated substrates at 4 mm/s velocity (Figure 3-14). Oddly, no definable features could be seen in films coated at 3 mm/s on PTS-coated films. At 4 mm/s, the AFM images do not appear to have any morphological features however the height profile appears to have packing structures like that seen in the OTS-coated substrates at 3 mm/s (Figure 3-14).

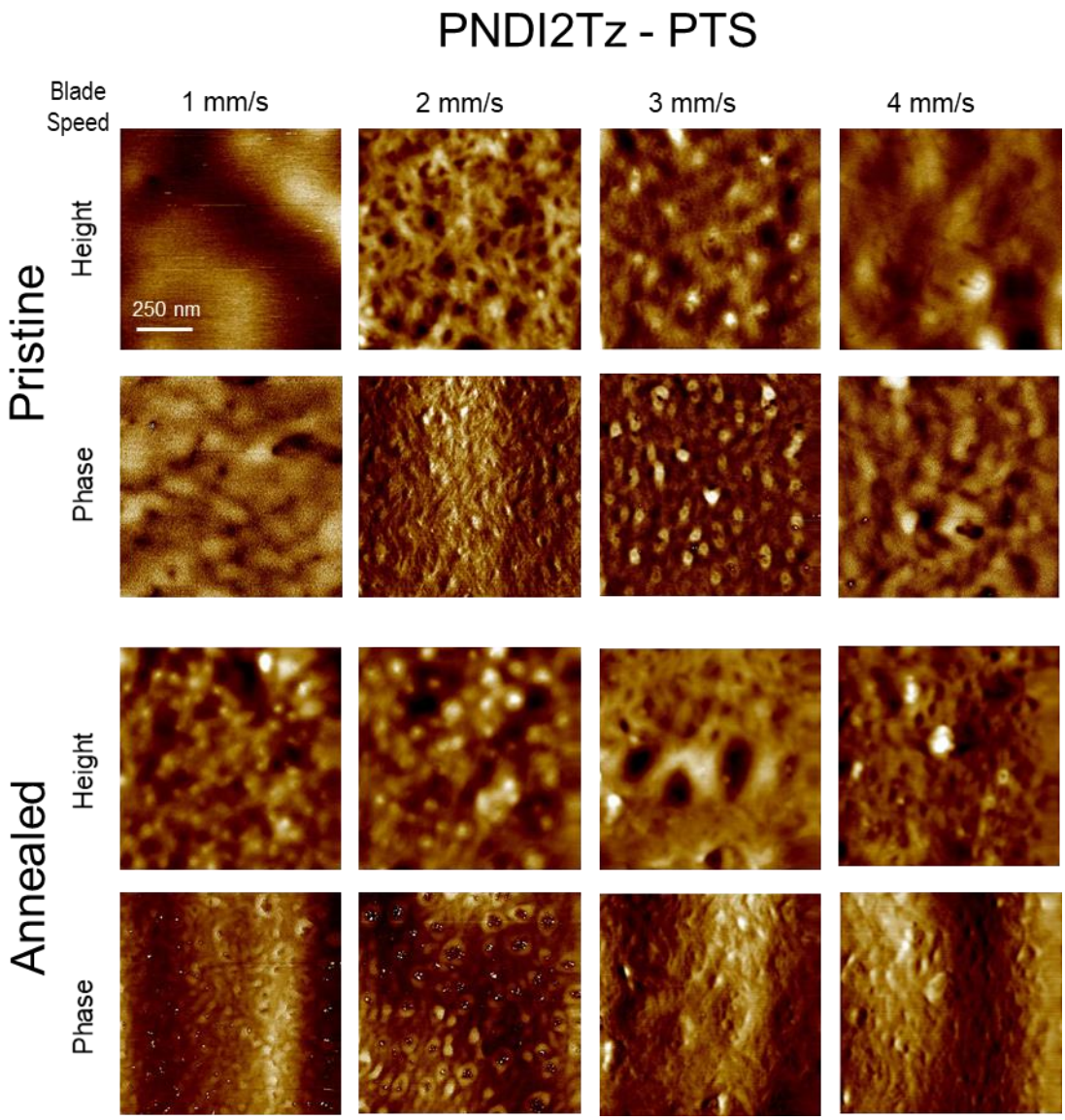

Figure 3-13 AFM images of PNDI2Tz blade-coated onto PTS-coated substrates at different velocities.[16] Annealed films were heated to 100 °C for 30 minutes under N_2.

[16] AFM images taken by undergraduate researchers, including Qianyi "Beth" Qu and Kyle Hamrock.

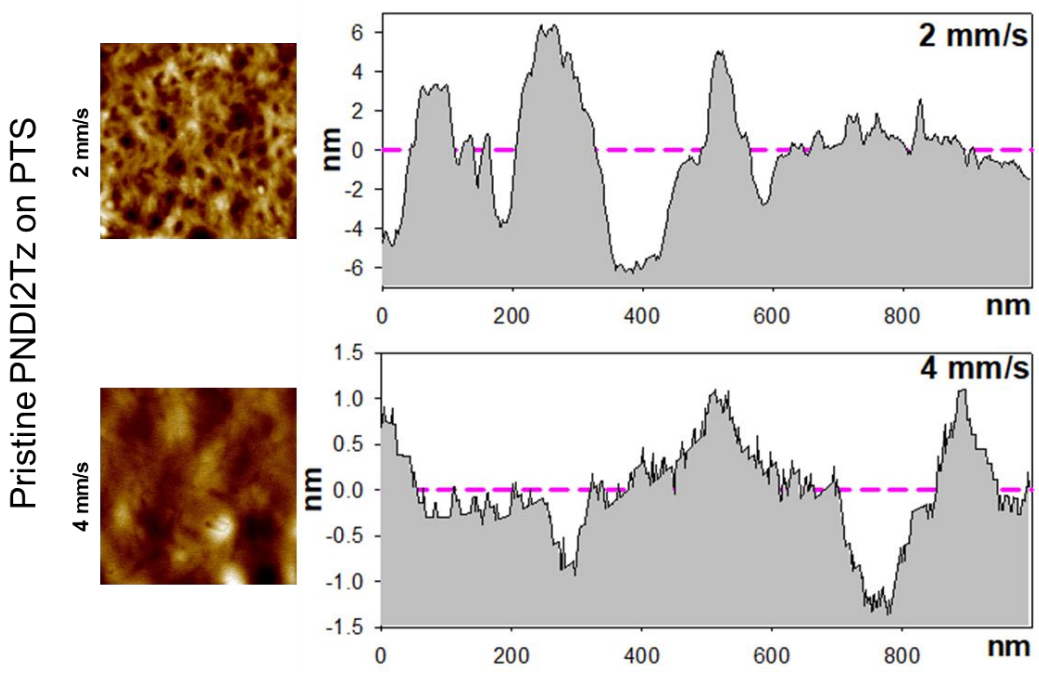

Figure 3-14 Height analysis of PNDI2Tz films blade-coated onto PTS-coated substrates at increasing velocities.

No definable features were observed on HMDS-coated substrates at any velocity, and the films appeared to be of very poor quality under AFM (Figure 3-15).

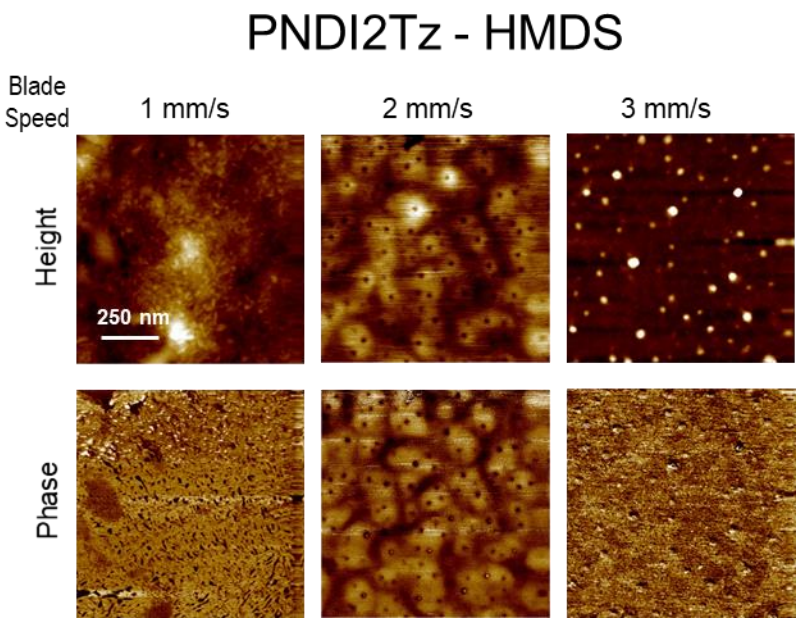

Figure 3-15 AFM images of PNDI2Tz blade-coated onto HMDS-coated substrates at different velocities.[17]

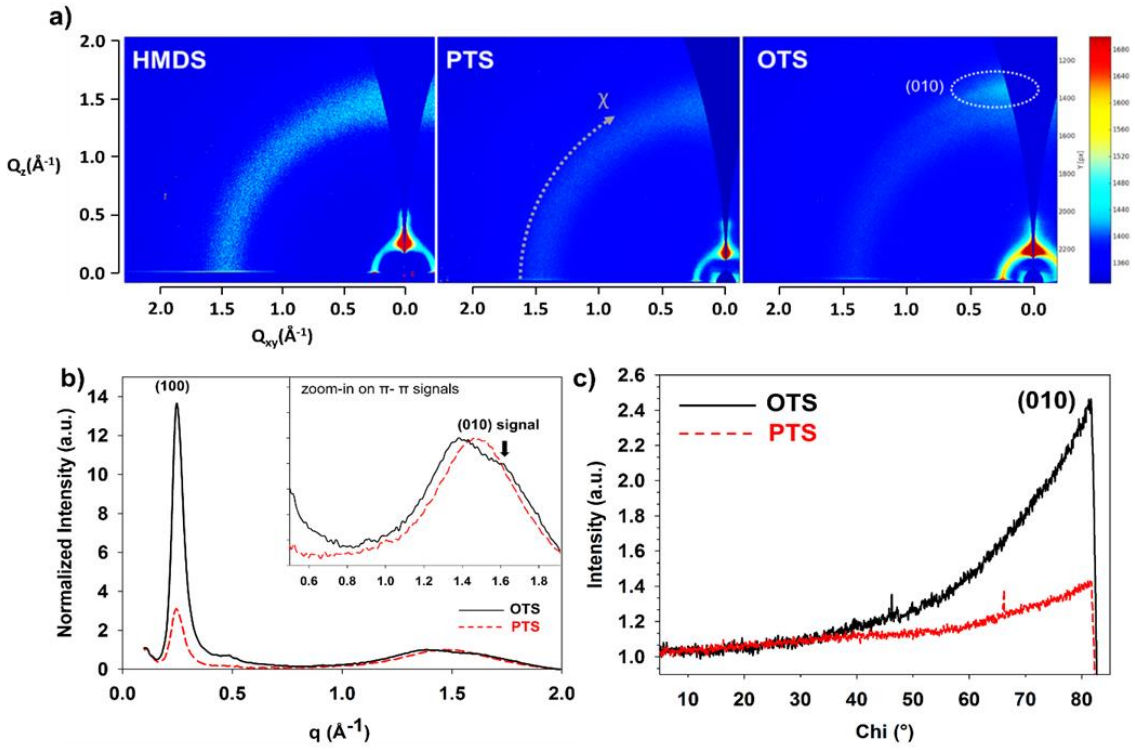

[17] AFM images taken by undergraduate researchers Qianyi "Beth" Qu and Kyle Hamrock.

Figure 3-16 a) GIWAXS image of PNDI2Tz thin films on HMDS, PTS and OTS processed SiO_2 surfaces; b) 1D line cut along chi = 15 ° with zoomed-in plot on q_z = 0.6 ~ 1.8 $Å^{-1}$; c) π-π stacking chi plot from x-y plane (chi = 0°) to z-axis (chi = 90 °).[17]

GIWAXS profiles of PNDI2Tz films presented (100) reflection peaks along the out-of-plane (q_z) direction, corresponding to polymer lamellar stacking oriented normal to the substrate (Figure 3-16[18]). However, halo-like patterns are apparent along the azimuthal angle at the (100) peak in HMDS- and PTS-treated substrates, indicating more isometric distributions of polymer orientations within the film.[179,180] The OTS-treated substrates had the strongest intensity (100) peaks. The calculated average (100) *d*-spacing for high temperature blade-coated polymer films on OTS-treated surfaces was 24.74 Å, which was slightly smaller than the 25.86 Å obtained for the PTS counterparts. Interestingly, the π-π stacking (010) peak at q = 1.623Å is in the film normal direction along q_z for the OTS-treated substrate corresponding to a π-π stacking distance of 3.87Å. While the (010) peak for the PTS-treated substrate is of overall much lower intensity than that for OTS, it also has its highest intensity along q_z. Two overlapping peaks in the π-π stacking

It should be noted that the π-π stacking distance of 3.87 Å on OTS-modified surfaces is (roughly) the size of the incremental height variations seen in the height profile of PNDI2Tz on OTS-modified substrates coated at 3 mm/s (Figure 3-11), which were multiples of 0.33 nm. This is consistent with the face-on orientation seen in the GIWAXS spectra.

[18] Plotting of GIWAXS data in Figure 3-16done by Dr. Zhibo Yuan. GIWAXS images taken by Ian Pelse at the Stanford Synchotron Radiation Light Source (SSRL).

PNDI2OD-T2 under the same blade-coating conditions showed network formation under AFM, however detailed nanofiber formation could not be observed at the same blade velocities as seen in PNDI2Tz (Figure 3-17).

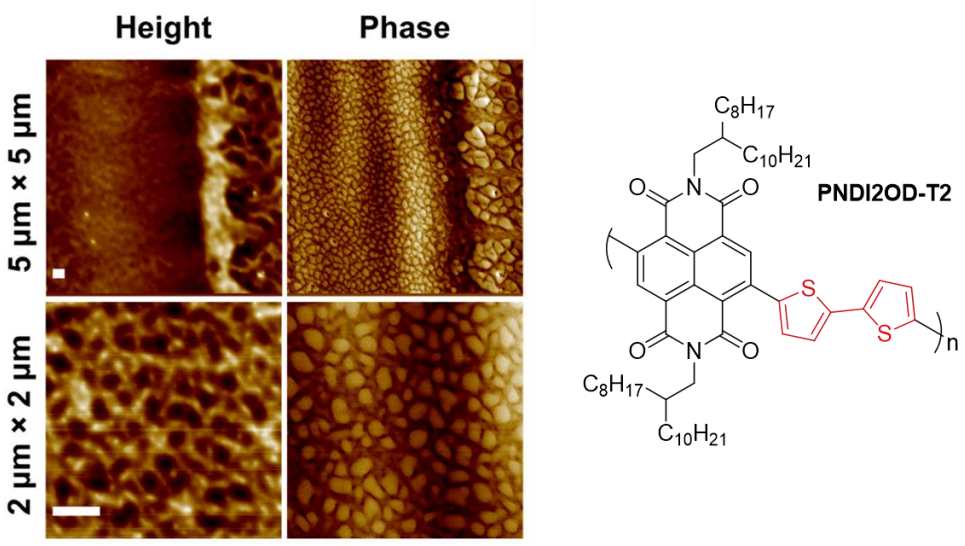

Figure 3-17 AFM images of PNDI2OD-T2 blade-coated on OTS-modified substrates at a coating velocity of 3 mm/s. Scale bar is 400 nm.

3.3.4 OFET Mobilities

OFET performance characteristics for PNDI2Tz devices are presented in Table 3-2, and the transfer characteristics in Figure 3-18. It can be seen that the mobility on OTS-modified substrates exhibited a maximum mobility of 7.05×10^{-2} $cm^2V^{-1}s^{-1}$ at a blade-coating speed of 3 mm/s. The OFET performance trends largely mirror the nanofiber network formation qualities seen in the AFM images. Increasing the blade-coating speed to 5 mm/s resulted in decreased mobility values (1.06×10^{-2} $cm^2V^{-1}s^{-1}$), which was expected from the poor film formation seen in the AFM images. The OTS-modified devices displayed the highest mobilities, which correlates with the nanofiber formation patterns seen previously. PNDI2OD-T2 had in increase in mobility from 0.047 $cm^2V^{-1}s^{-1}$ on

HMDS-modified substrates to 0.216 $cm^2V^{-1}s^{-1}$ on OTS-modified substrates, again mirroring morphology results.

No difference in OFET performance was seen with devices blade-coated perpendicular to the OFET channel vs. those coated parallel with the channel. While both PNDI2Tz and PNDI2OD-T2 were of 'sufficient' molecular weight that would widely make them considered 'polymers', it is important to remember that the repeat units are themselves high in molecular weight as well (998.53 g/mol for PNDI2OD-T2, and 1103.72 g/mol for PNDI2Tz). From the number average molecular weights, this would make for approximately 51 repeat units for PNDI2OD-T2 and 26 repeat units for PNDI2Tz. Given the 'short' chain lengths and the inherent planarity and torsional barriers of the component units, these polymers are likely not in folded or entangled chain formations, and hence would not be as susceptible to shearing effects as other more flexible longer-chain polymers (e.g. P3HT).[134]

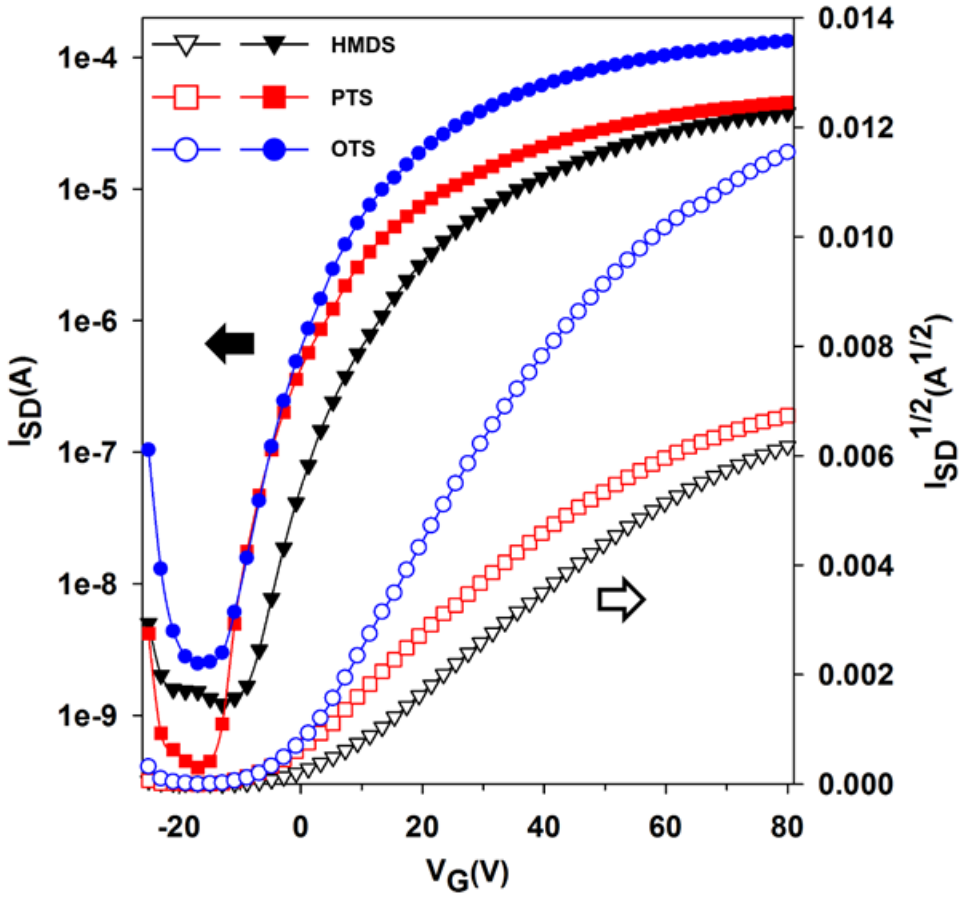

Figure 3-18 Transfer curve of PNDI2Tz devices coated on HMDS, PTS, and OTS-modified SiO_2 BGBC transistors. Solid dots are I_{SD} and V_G curves, while hollow-dots are $I_{SD}^{1/2}$ vs. V_G curves. Devices were fabricated at a blade-coating speed of 3 mm/s.[19]

[19] Plot of PNDI2Tz transfer curves done by Dr. Zhibo Yuan.

Table 3-2 N-channel mobility values of PNDI2Tz BGBC OFET devices blade-coated under the specified conditions. Thermal annealing was carried out at 100 °C for 30 minutes. OFET data shown was taken over 10 devices for each blade coating condition.[20]

	Surface Modifier	Surface Energy γ_s (mJ/m^2)	Blade Velocity (mm/s)	Substrate Temperature (°C)	Thermal Annealing	Mobility ($cm^2V^{-1}s^{-1}$)
A	OTS	21.99	0.5	R.T.	no	9.03E-03 ± 2.08E-03
B			0.5	R.T.	yes	1.12E-02 ± 1.12E-03
C			1	100	-	1.57E-02 ± 1.26E-03
D			2	100	-	1.29E-02 ± 2.19E-03
E			3	100	-	7.05E-02 ± 5.43E-03
F			4	100	-	1.06E-02 ± 2.09E-03
G	PTS	28.63	3	100	-	3.82E-02 ± 4.97E-03
H	HMDS	35.77	3	100	-	1.62E-02 ± 1.49E-03

[20] Mobility values calculated by Dr. Zhibo Yuan

3.4 Summary and Conclusions

Two analogous NDI-based copolymers, PNDI2Tz and PNDI2OD-T2, were synthesized, blade-coated onto SAM-modified substrates and their performance within BGBC OFET devices was characterized. PNDI2Tz exhibited nanofiber formation on OTS-modified substrates, with clearly seen network formations on films blade-coated at 2 and 3 mm/s. In contrast, PNDI2OD-T2 did not exhibit such robust nanofiber formations under similar conditions, despite the structural similarities to PNDI2Tz. GIWAXS showed tighter molecular packing and increased crystallinity of PNDI2Tz on OTS-modified substrates than seen on PTS- or HMDS-modified substrates. Analysis of the height profiles from AFM revealed bundled nanofiber formations in films blade-coated onto OTS surfaces at 2, 3, and 4 mm/s. Both the height profiles and GIWAXS results point to face-on packing of the PNDI2Tz films relative to the substrate. OFET mobilities mirrored the nanofiber network formations seen in AFM images, with the highest n-channel mobility of 7.05×10^{-2} $cm^2V^{-1}s^{-1}$ observed in films with the largest degrees of interconnected nanofiber network formation. This is consistent with the commonly-accepted notion that achieving high-performance polymer OFET devices requires continuous charge pathways extending across the semiconductor channel.

Though increases in nanofiber morphology and field-effect mobility were observed with changes in the surface-modifier used on the substrate, no clear specific relation between the macroscopic properties of the substrate (e.g. polarity, surface energy) and these observed results can be made in the context of recent literature. Yasuda *et. al.* reported higher field-effect mobilities for both crystalline and amorphous organic semiconductors deposited on hydrophobic surfaces, but notably did not find a correlation between

mobilities and the roughness and dielectric constant of the substrates.[181] The analogous polymers chosen for comparison, PNDI2Tz and PNDI2OD-T2, did not behave as similarly as anticipated despite identical processing conditions. Rather, the results can be understood as a superposition of many factors, including inherent chain flexibility, propensity towards π-π stacking, specific interactions with solvents and substrates, etc.[182] Rather than finding a general correlation, this study serves to add another example of nanofiber formation of a semiconducting polymer in a solution-deposition technique amenable to commercial scale-up. Specifically, the need for increased temperatures for adequate film formation on passivated surfaces was identified, which is important to the field of n-channel polymer OFET devices as such surface passivation is necessary to observe electron transport.

SUMMARY AND RECOMMENDATIONS FOR FUTURE WORK

3.5 Summary

The development of semiconducting conjugated polymers for organic field effect transistors (OFETs) has been the focus of intense research efforts for their key role in plastic electronics, as well as a vision of solution processability leading to reduced costs in device fabrication relative to their inorganic counterparts. The pursuit of high-performance *n*-channel (electron transporting) polymer semiconductors vital to the development of robust and low-cost organic integrated circuits has faced significant challenges; mainly for poor ambient operational stability and OFET device performance lagging far behind that of *p*-channel organic semiconductors (OSCs). As an alternative to the ubiquitous donor-acceptor (DA) molecular design strategy, an all-acceptor (AA) unipolar approach was implemented in the design of poly(2-(2-decyltetradecyl)-6-(5-(5'-methyl-[2,2'-bithiaol]-5-yl)-3-(5-methylpyridin-2-yl)-5-(tricosan-11-yl)-2,5-dihydropyrrolo[3,4-c]pyrrole-1,4-dione) (PDBPyBTz). The *n*-channel copolymer allowed investigation of the impact of electron withdrawing moieties on conjugated polymer device performance and the utility of the AA molecular design strategy. As an analog to benzene, the pyridines flanking the diketopyrrolopyrrole moiety in PDBPyBTz were strategically chosen to lower the energy levels and impart planarity to the monomer, both of which aid in achieving stable *n*-channel performance. Incorporation of PDBPyBTz into a bottom-gate-bottom-contact OFET, afforded a device that exhibited unipolar electron transport. In addition to developing a high-performance n-channel polymer, this study allowed for an investigation of structure-property relationships crucial to the design of such materials in high demand for sustainable

technologies including organic photovoltaics and other solution-processed organic electronic devices.

During the study of another all-accepter polymeric semiconductor, nanofiber formation was observed with blade-coat processing on OTS-modified substrates. An investigation of the processing characteristics of PNDI2Tz, and the structurally analogous PNDI2OD-T2 revealed a preference for the hydrophobic OTS-modified substrates in not only forming distinctive morphologies but also maximizing OFET performance. This study highlighted the profound influence on processing characteristics of polymeric semiconductors and the subsequent impact on OFET performance.

3.6 Recommendations for Future Work

The electron-deficient and planar nature of the pyridinyl-flanked DPP has shown promising results of enabling n-channel OFET behavior in polymer semiconductors it is incorporated into. It would be interesting to explore further iterations of this compound, namely, replacing the pyridinyl flanking groups with 1,4-pyrizine flanking groups. The additional electronegative nitrogen in 1,4-pyrazine would further decrease the frontier energy levels of compounds it is incorporated into, and preliminary calculations have shown planar equilibrium geometries between he 1,4-pyrazine moiety and neighboring moieties (such as BTz).

As discussed in chapter 2, it is not clear why PDBPyBTz is solely an electron-transporting semiconductor in the device structure employed in this study. In measuring the temperature-dependent field-effect mobilities of the PDBPyBTz devices described above, the activation energy for the electron (and possibly hole, at higher temperatures)

can be determined, and hence will give the 'depth' of the charge traps that are present. It is speculated that as hole-traps specific to PDBPyBTz are the source of this unipolar charge transport, and hence observing OFET behavior in various device architectures (e.g. TGBC devices to reduce channel resistance), and semiconductor/dielectric interfaces (e.g. PMMA as the insulating dielectric, or different surface modifiers for the SiO2 substrates) would provide evidence for the hole traps being intrinsic to PDBPyBTz (or not). Considering past reports of the 2,2'-bithiazole moiety forming complexes with Lewis acids,[133] it would be interesting to perform studies of spectroscopic changes in PDBPyBTz films upon exposure to various Lewis acids (e.g. BF_3OEt_2, $FeCl_3$, etc.) in controlled environments, which would indicate potential complexation. The results of these suggested experiments would determine the next steps in identifying the sources of the hole-traps.

APPENDIX A. SUPPORTING CHARACTERIZATION DATA

A.1 Synthesis Characterization

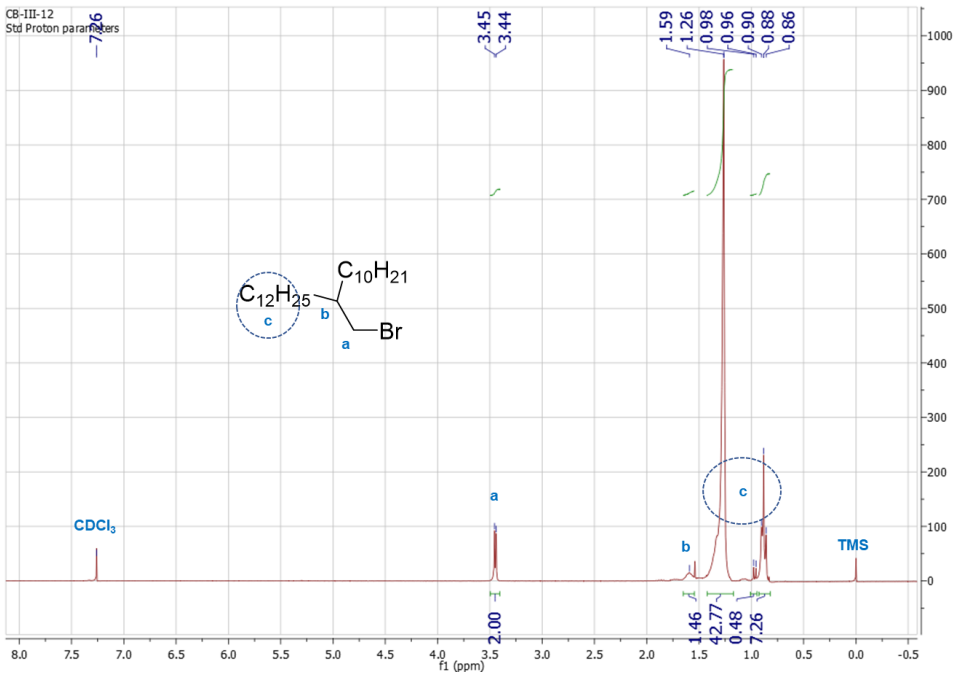

Figure A-1 ^{1}H NMR 11-bromomethyltricosane (**1**)

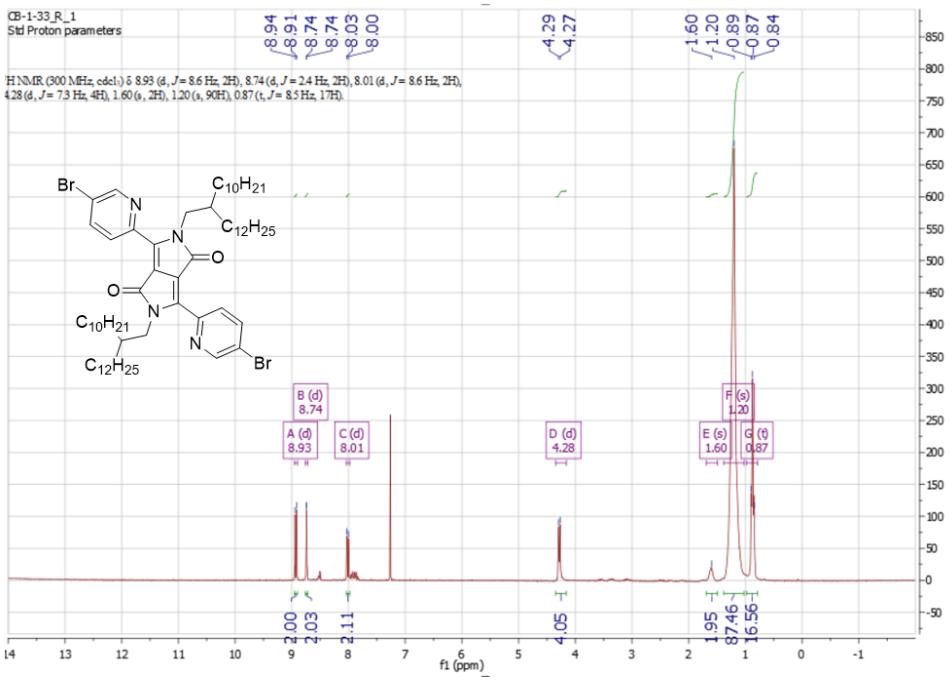

Figure A-2 ^{1}H NMR PyDPP-Al (**3**)

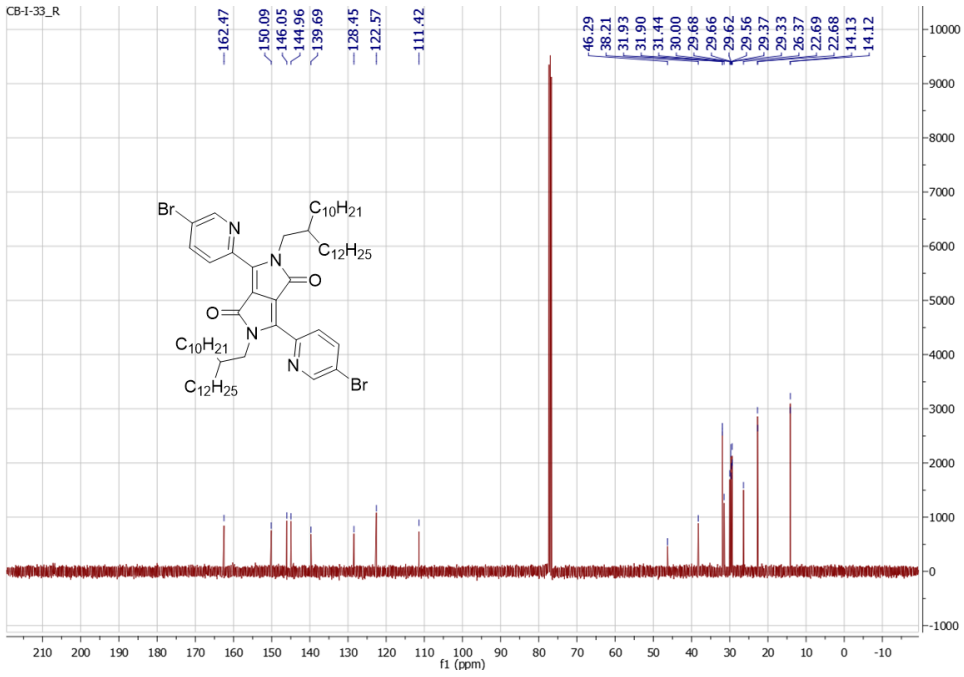

Figure A-3 ^{13}C NMR PyDPP-Al (**3**)

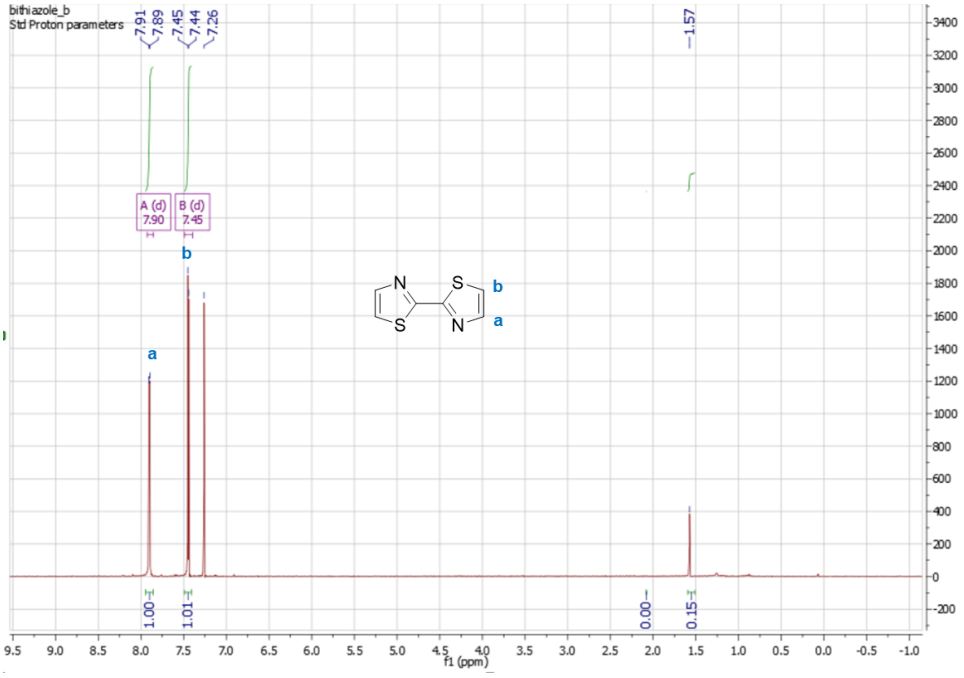

Figure A-4 ^{1}H NMR 2,2'-Bithiazole (**4**)

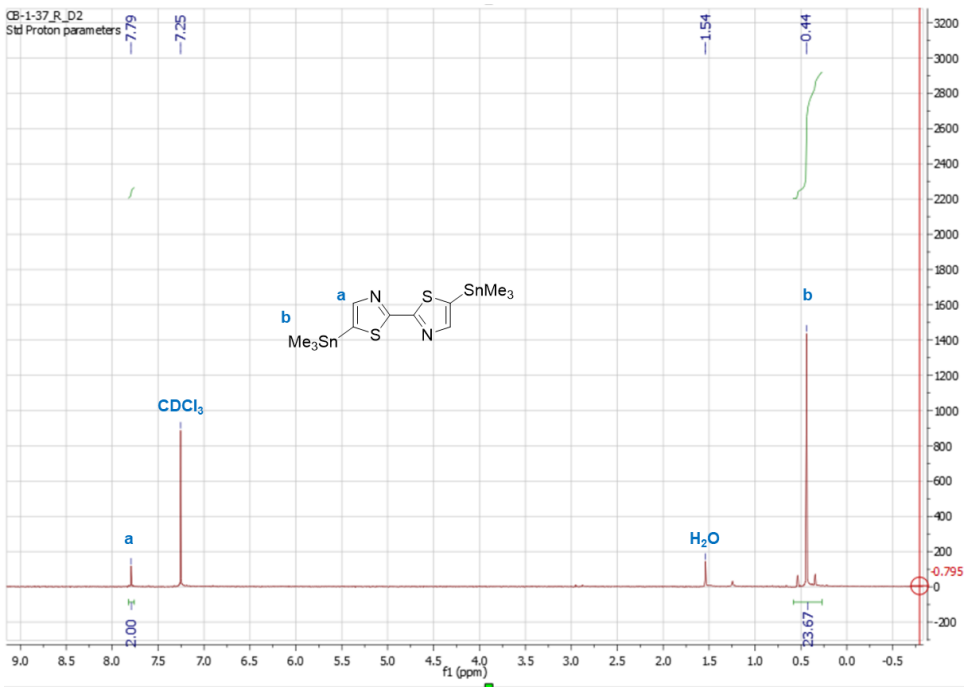

Figure A-5 ^{1}H NMR 5,5'-bis(trimethylstannyl)-2,2'-bithiazole (**5**)

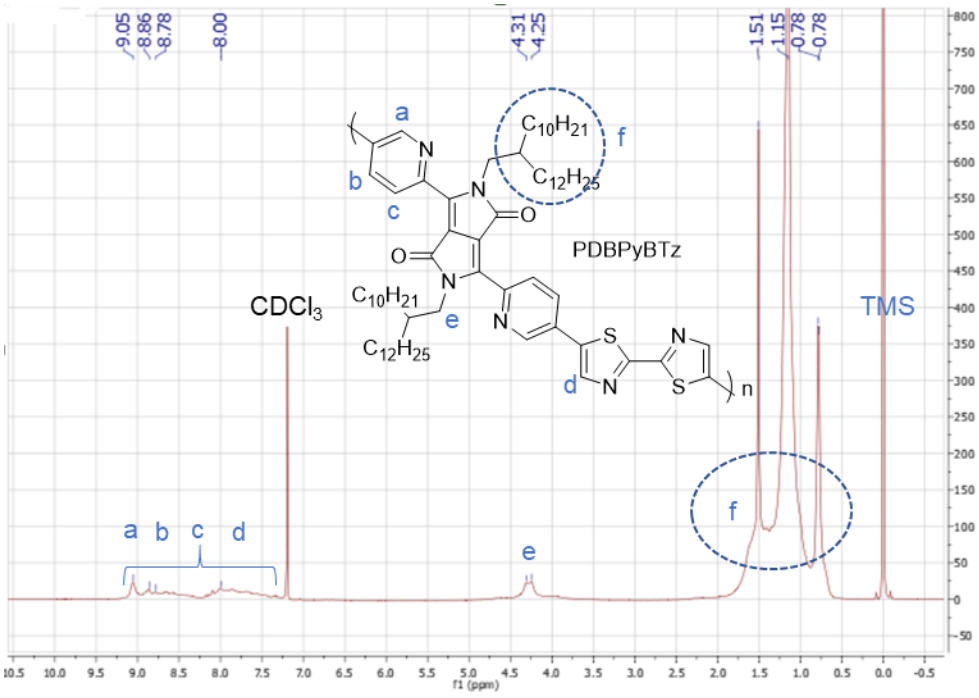

Figure A-6 ^{1}H NMR ($CDCl_3$, 700 MHz) of PDBPyBTz. Overly-large TMS shift due to over-zealous spiking.

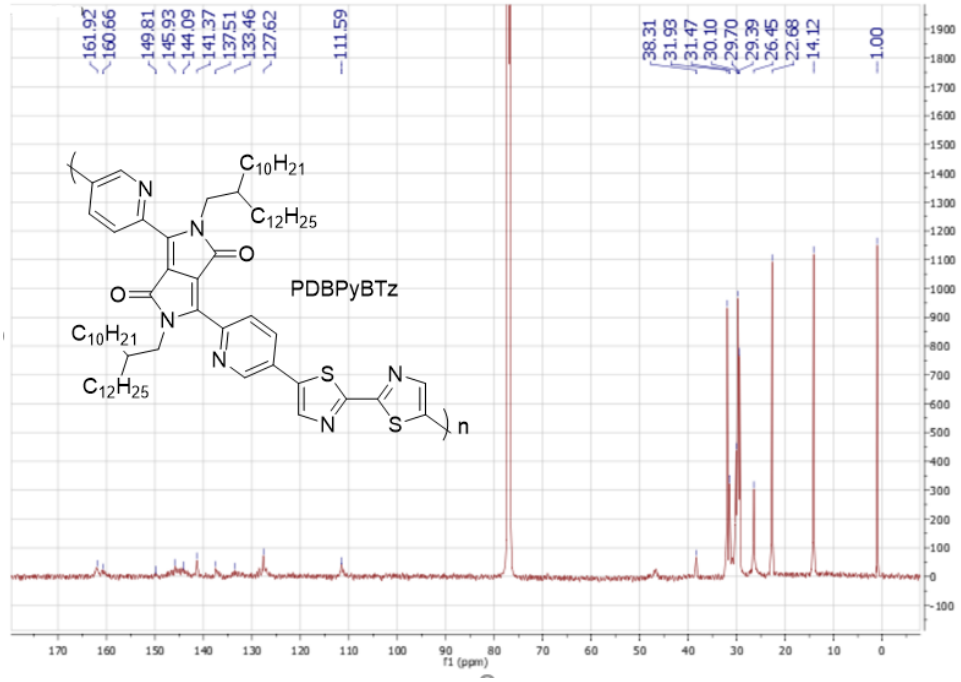

Figure A-7 ^{13}C NMR ($CDCl_3$, 700 MHz) PDBPyBTz

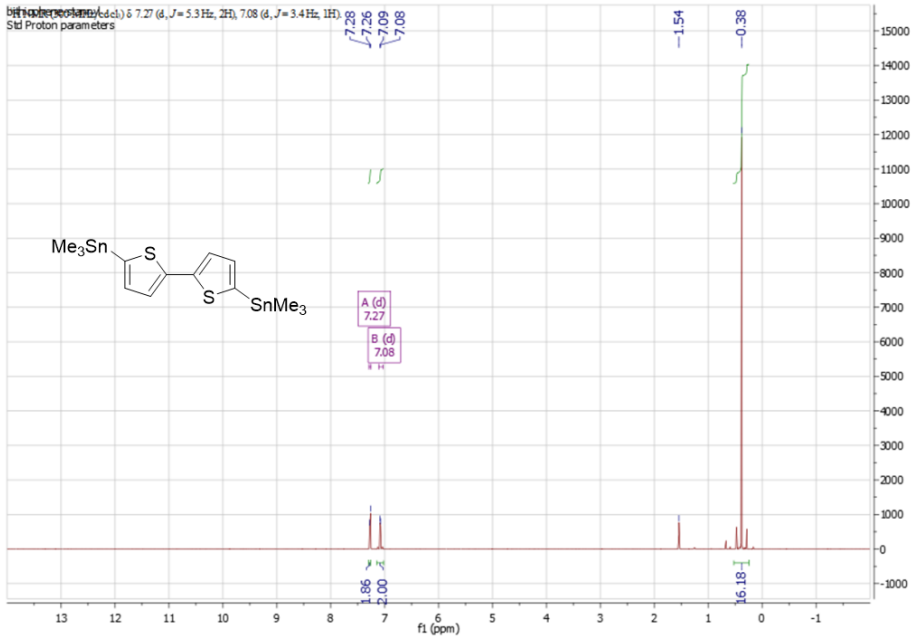

Figure A-8 ^{1}H NMR ($CDCl_3$, 300 MHz) Stannylated bithiophene (**7**)

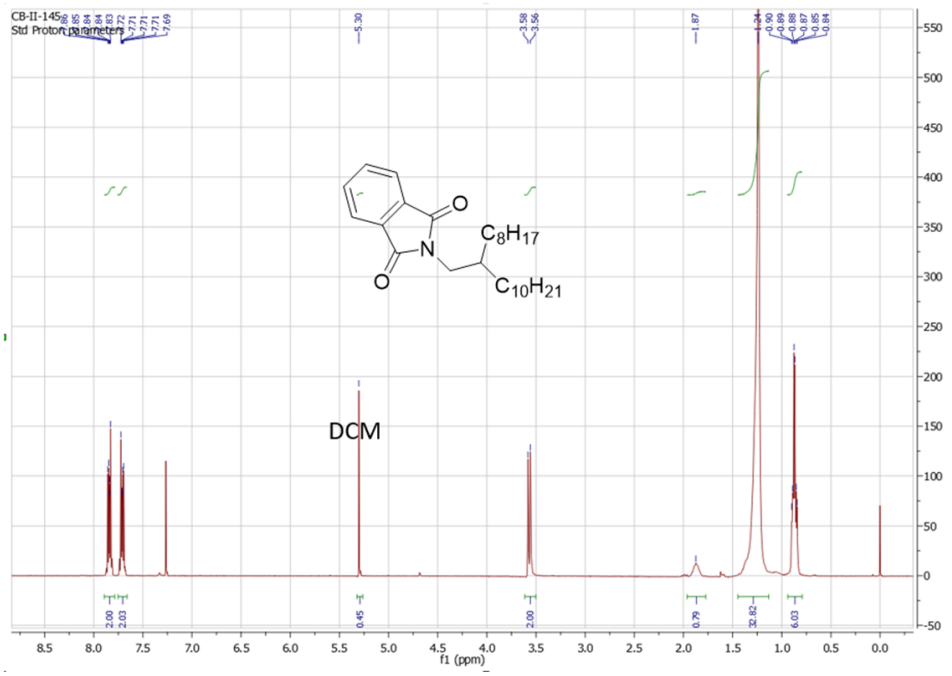

Figure A-9 ^{1}H NMR 2-(2-ocyldodecyl)isoindoline-1,3-dione

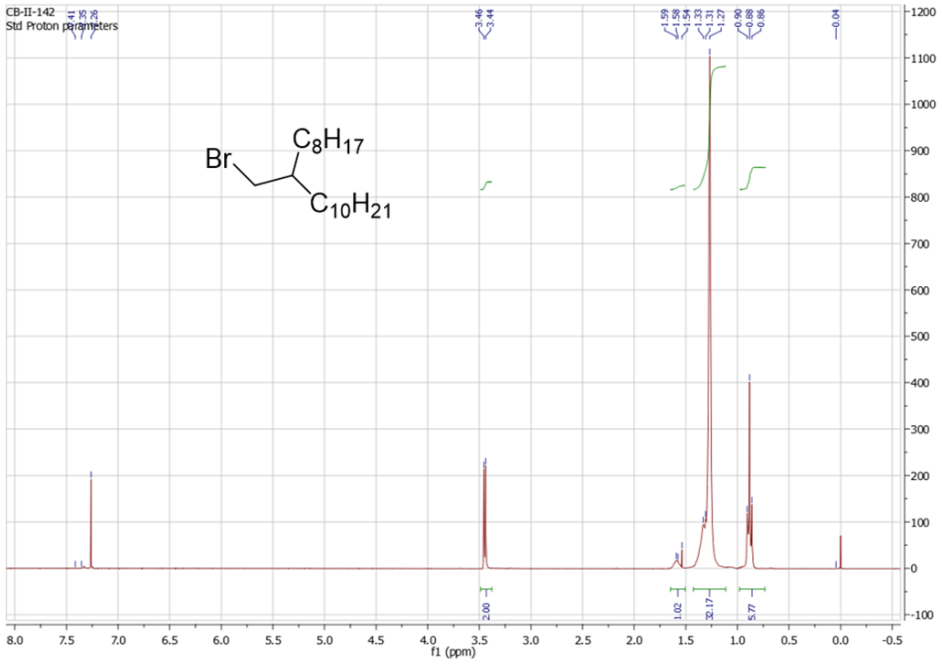

Figure A-10 ^{1}H NMR 9-(bromomethyl)nonadecane

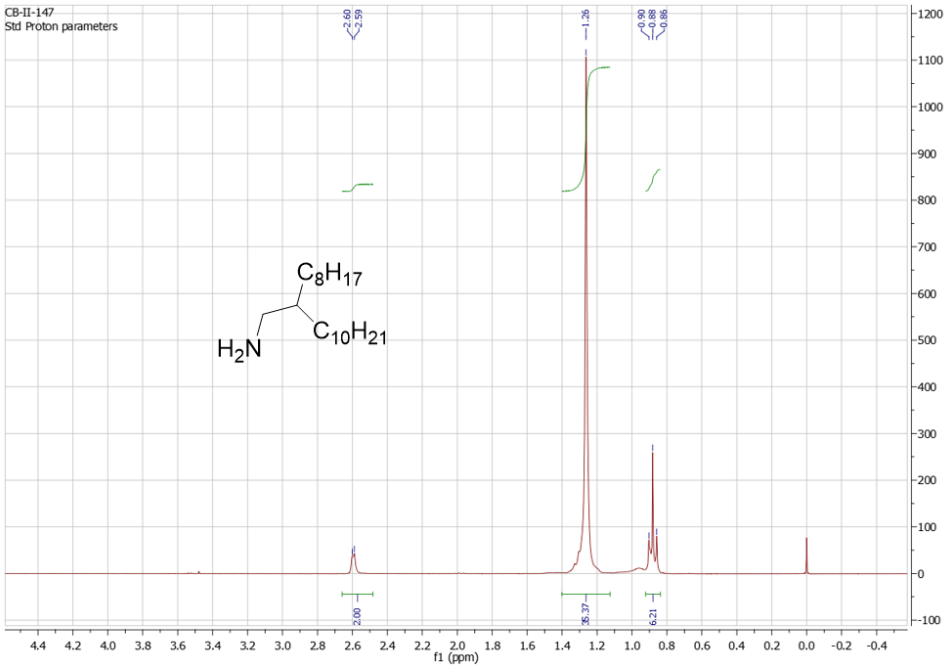

Figure A-11 ^{1}H NMR 2-octyldodecan-1-amine

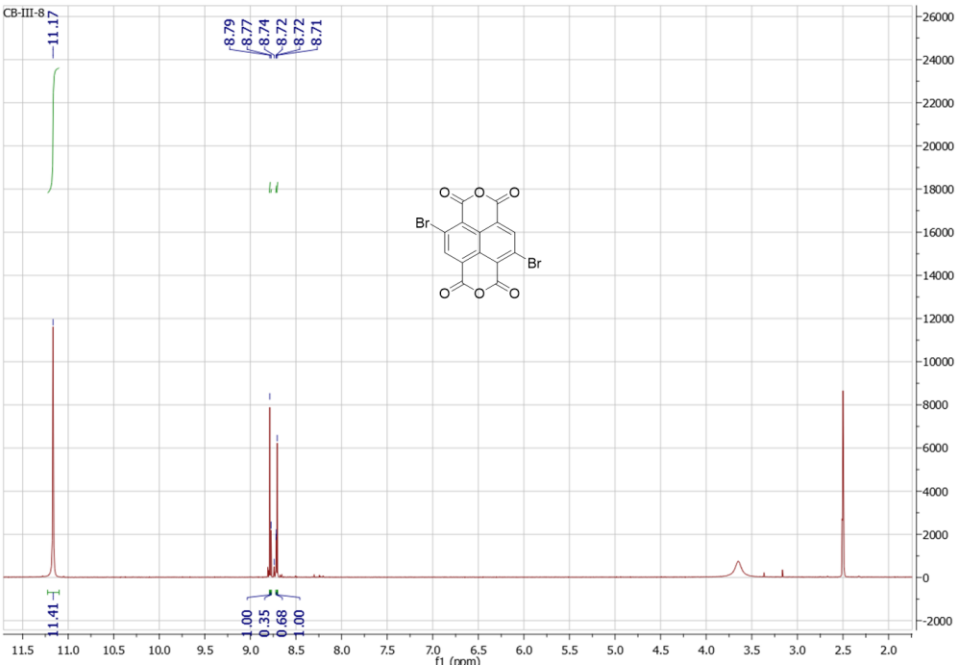

Figure A-12 ^{1}H NMR 2,6-dibromo-1,4,5,8-tetracarboxynaphthalenediimide

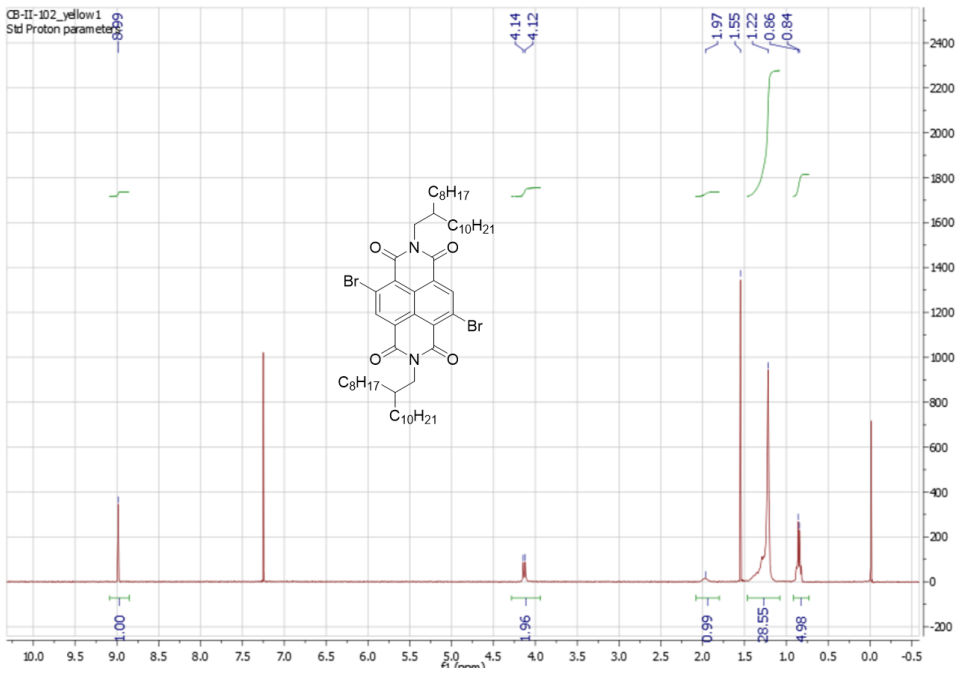

Figure A-13 ^{1}H NMR of Alkylated dibromo NDI

A.2 GIWAXS spectra

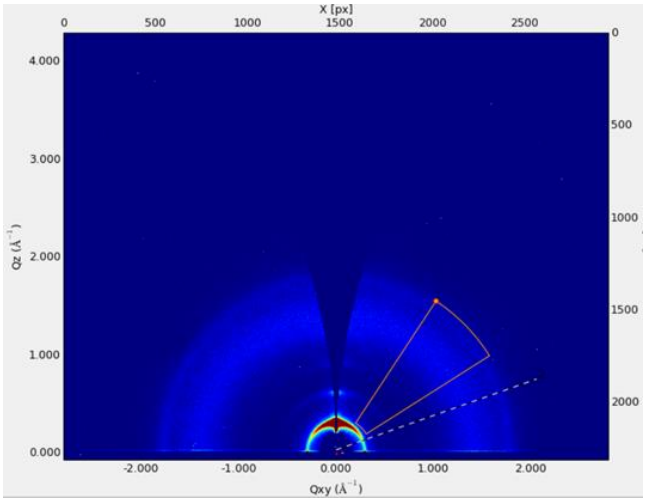

Figure A-14 2D-GIWAXS area detector image of PDBPyBTz film.[21]

A.3 Supporting OFET Characterization

[21] Image taken by Ian Pelse at the Stanford Synchotron Radiation Light Source (SSRL).

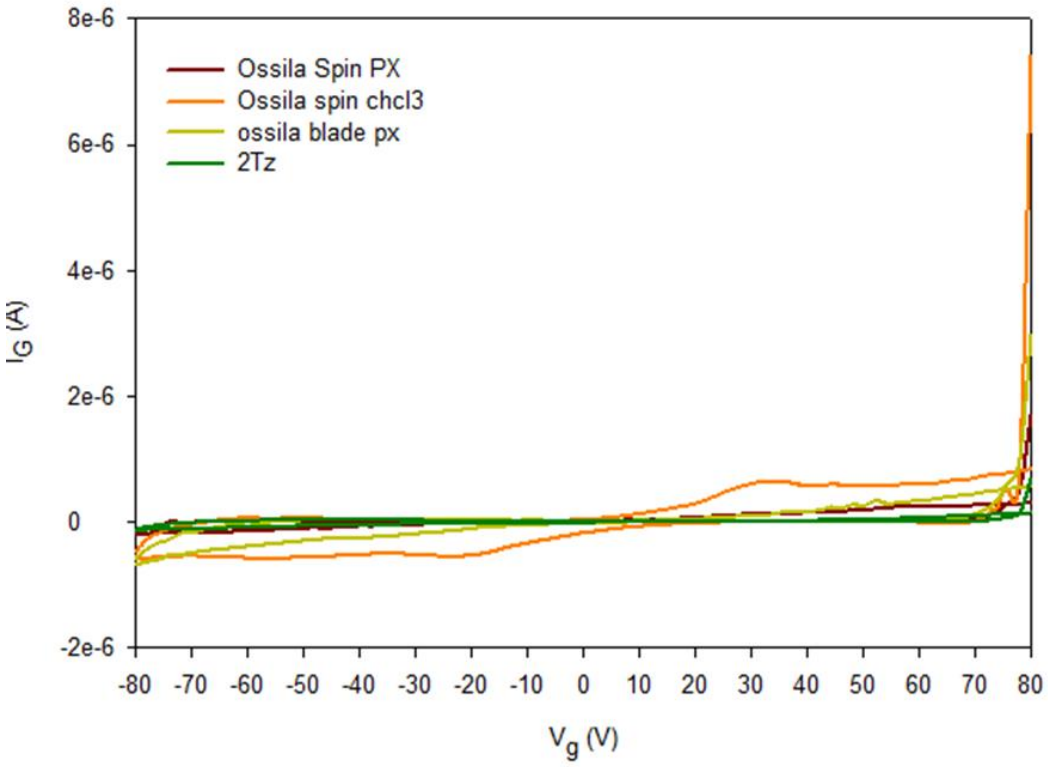

Figure A-15 Plot of gate leakage current vs. Vg for PDBPyBT ("ossila") and PDBTz ("Tz") devices

REFERENCES

(1) Seidler, P. F.; Shaw, J. M. Organic Electronics : Introduction. *IBM J. Res. Dev.* **2001**, *45* (1), 3–9.

(2) Chiang, C. K.; Fincher, C. R.; Park, Y. W.; Heeger, A. J.; Shirakawa, H.; Louis, E. J.; Gau, S. C.; Macdiarmid, A. G. Electrical Conductivity in Doped Polyacetylene. *Phys. Rev. Lett.* **1977**, *39* (17), 1098–1101.

(3) Sirringhaus, H. 25th Anniversary Article: Organic Field-Effect Transistors: The Path Beyond Amorphous Silicon. *Adv. Mater.* **2014**, *26*, 1319–1335.

(4) Mascaro, D. J. Organic Thin- Film Transistors : A Review of Recent Advances. *IBM J. Res. Dev.* **2001**, *45* (1), 11–27.

(5) Forrest, S. R. The Path to Ubiquitous and Low-Cost Organic Electronic Appliances on Plastic. *Nature* **2004**, *428*, 911–918.

(6) Lee, J.-Y. Apple Teams up with LG Display for Foldable IPhone. *The Korea Herald*. Seoul October 11, 2011.

(7) Miller, N. J.; Leon, F. A. *OLED Lighting Products: Capabilities, Challenges, Potenial*; 2016.

(8) OLED-info. AMOLED- introduction and market status https://www.oled-info.com/amoled.

(9) Van Camp, J. LG's OLED TVs Are Cheaper Than We've Ever Seen Them https://www.wired.com/story/lg-b8-c8-oled-deals/.

(10) van Mullekom, H. A. M.; Vekemans, J. A. J. M.; Havinga, E. E.; Meijer, E. W. Developments in the Chemistry and Band Gap Engineering of Donor-Acceptor Substituted Conjugated Polyemers. *Mater. Sci. Eng.* **2001**, *32*, 1–40.

(11) Marszalek, T.; Li, M.; Pisula, W. Design Directed Self-Assembly of Donor-Acceptor Polymers. *Chem. Commun.* **2016**, *52* (73), 10938–10947.

(12) Hashemi, D.; Ma, X.; Ansari, R.; Kim, J.; Kieffer, J. Design Principles for the Energy Level Tuning in Donor/Acceptor Conjugated Polymers. *Phys. Chem. Chem. Phys.* **2019**, *21* (2), 789–799.

(13) Bredas, J. L.; Calbert, J. P.; Filho, D. A. S.; Cornil, J. Organic Semiconductors : A Theoretical Characterization of the Basic Parameters Governing Charge Transport. *Proc. Natl. Acad. Sci.* **2002**, *99* (9).

(14) Roberts, J. D. *Notes on Molecular Orbital Calculations*, 1st ed.;

Benjamin/Cummings Publishing Company Inc.: Reading, MA, 1961.

(15) Carey, F. A.; Sundberg, R. J. *Advanced Organic Chemistry Part A: Structure and Mechanisms*, 5th ed.; Springer: New York, 2007.

(16) Lee, C.; Yang, W.; Parr, R. G. Development of the Colle-Salvetti Correlation-Energy Formula into a Functional of the Electron Density. *Phys. Rev. B* **1988**, *37*, 785–789.

(17) Körzdörfer, T.; Brédas, J. L. Organic Electronic Materials: Recent Advances in the Dft Description of the Ground and Excited States Using Tuned Range-Separated Hybrid Functionals. *Acc. Chem. Res.* **2014**, *47* (11), 3284–3291.

(18) Cohen, A. J. Insights into Current Limitations of Density Functional Theory. *Science (80-.).* **2008**, *321*, 792–794.

(19) Cohen, A. J.; Mori-Sánchez, P.; Yang, W. Challenges for Density Functional Theory. *Chem. Rev.* **2012**, *112* (1), 289–320.

(20) Brédas, J.-L. Organic Electronics: Does a Plot of the HOMO–LUMO Wave Functions Provide Useful Information? *Chem. Mater.* **2017**, *29* (2), 477–478.

(21) Körzdörfer, T.; Brédas, J. L. Organic Electronic Materials: Recent Advances in the Dft Description of the Ground and Excited States Using Tuned Range-Separated Hybrid Functionals. *Acc. Chem. Res.* **2014**, *47* (11), 3284–3291.

(22) Bredas, J. Mind the Gap! *Mater. Horizons* **2014**, *1*, 17–19.

(23) Engle, T.; Reid, P. *Physical Chemistry*, 2nd ed.; Pearson: New York, 2010.

(24) Muchová, E.; Slaviček, P. Beyond Koopmans' Theorem: Electron Binding Energies in Disordered Materials. *J. Phys. Condens. Matter* **2019**, *31* (4), 043001.

(25) McNaught, A. D.; Wilkinson, A. *IUPAC Compendium of Chemical Terminology, 2nd Ed.*, 2nd ed.; Nic, M., Jirat, J., Kosata, B., Jenkins, A., Eds.; Blackwell Scientific Publications: Oxford, 1997.

(26) Miessler, G. L.; Tarr, D. A. *Inorganic Chemistry*, 4th ed.; Pearson: New York, 2011.

(27) James, T. L. X-Ray Photoelectron Spectroscopy. *J. Chem. Educ.* **1971**, *48*, 712–718.

(28) Park, Y.; So, Y.; Chung, S. J.; Jin, J. I. Photoelectron Spectroscopy Study of the Electronic Structures of Poly(p-Phenylenevinylene) Derivatives. *J. Korean Phys. Soc.* **2000**, *37* (1), 59–63.

(29) Duke, C. B.; Paton, A.; Salaneck, W. R.; Thomas, H. R.; Plummer, E. W.; Heeger, A. J.; MacDiarmid, A. G. Electronic Structure of Polyenes and Polyacetylene. *Chem. Phys. Lett.* **1978**, *59*, 146–150.

(30) Hufner, S. *Photoelectron Spectroscopy: Principles and Applications*, 3rd ed.; Springer -Verlag Berlin Heidelberg: Berlin, 2003.

(31) Ballard, R. E. Photoelectron Spectroscopy of Liquids: Relationships between Ionization Energy and Reduction Potential. *Chem. Phys. Lett.* **1976**, *42* (1), 97–98.

(32) Miller, L. L.; Nordblom, G. D.; Mayeda, E. A. A Simple, Comprehensive Correlation of Organic Oxidation and Ionization Potentials. *J. Org. Chem.* **1972**, *37* (6), 916–918.

(33) Neikam, W. C.; Dimeler, G. R.; Desmond, M. M. A Correlation of Electrochemical Oxidation Potential of Organic Compounds with Photoionization Potential. *J. Electrochem. Soc.* **1964**, *111* (10), 1190.

(34) Bhattacharya, R.; Basu, S. Reduction Potentials of Conjugated Systems. *Naturwissenschaften* **1958**, *45* (9), 208–209.

(35) Marken, F.; Neudeck, A.; Bond, A. M. Cyclic Voltammetry. *Electroanal. Methods Guid. to Exp. Appl.* **2010**, *2* (2), 57–106.

(36) Elgrishi, N.; Rountree, K. J.; McCarthy, B. D.; Rountree, E. S.; Eisenhart, T. T.; Dempsey, J. L. A Practical Beginner's Guide to Cyclic Voltammetry. *J. Chem. Educ.* **2017**, acs.jchemed.7b00361.

(37) Gagne, R. R.; Koval, C. A.; Lisensky, G. C. Ferrocene as an Internal Standard for Electrochemical Measurements. *Inorg. Chem.* **1980**, *19* (9), 2854–2855.

(38) Pavlishchuk, V. V.; Addison, A. W. Conversion Constants for Redox Potentials Measured versus Different Reference Electrodes in Acetonitrile Solutions at 25°C. *Inorganica Chim. Acta* **2000**, *298* (1), 97–102.

(39) Gritzner, G.; Kuta, J. Recommendations on Reporting Electrode Potentials in Nonaqueous Solvents. *Pure Appl. Chem.* **1984**, *56*, 461–466.

(40) Visy, C.; Lukkari, J.; Kankare, J. A Thermodynamic Approach to the Interpretation of Anodic and Cathodic Doping of Poly(3-Methylthiophene). *J. Electroanal. Chem.* **1991**, *319* (1–2), 85–100.

(41) Visy, C.; Lukkari, J.; Kankare, J. Scheme for the Anodic and Cathodic Transformations in Polythiophenes. *Macromolecules* **1993**, *26* (13), 3295–3298.

(42) Johansson, T.; Mammo, W.; Svensson, M.; Andersson, R.; Ingana, O. Electrochemical Bandgaps of Substituted Polythiophenes. *J. Mater. Chem.* **2003**, *13*, 1316–1323.

(43) Brédas, J. L.; Silbey, R.; Boudreaux, D. S.; Chance, R. R. Chain-Length Dependence of Electronic and Electrochemical Properties of Conjugated Systems: Polyacetylene, Polyphenylene, Polythiophene, and Polypyrrole. *J. Am. Chem. Soc.*

1983, *105* (22), 6555–6559.

(44) Cardona, C. M.; Li, W.; Kaifer, A. E.; Stockdale, D.; Bazan, G. C. Electrochemical Considerations for Determining Absolute Frontier Orbital Energy Levels of Conjugated Polymers for Solar Cell Applications. *Adv. Mater.* **2011**, *23*, 2367–2371.

(45) Cornil, J.; Brédas, J. L.; Zaumseil, J.; Sirringhaus, H. Ambipolar Transport in Organic Conjugated Materials. *Adv. Mater.* **2007**, *19* (14), 1791–1799.

(46) Olivier, Y.; Lemaur, V.; Brédas, J. L.; Cornil, J. Charge Hopping in Organic Semiconductors: Influence of Molecular Parameters on Macroscopic Mobilities in Model One-Dimensional Stacks. *J. Phys. Chem. A* **2006**, *110* (19), 6356–6364.

(47) Coropceanu, V.; Cornil, J.; da Silva Filho, D. A.; Olivier, Y.; Silbey, R.; Brédas, J. L. Charge Transport in Organic Semiconductors. *Chem. Rev.* **2007**, *107* (4), 926–952.

(48) Brédas, J. L.; Beljonne, D.; Coropceanu, V.; Cornil, J. Charge-Transfer and Energy-Transfer Processes in π-Conjugated Oligomers and Polymers: A Molecular Picture. *Chem. Rev.* **2004**, *104* (11), 4971–5003.

(49) Marcus, R. A. Electron Transfer Reactions. *Rev. Mod. Phys.* **1993**, *65* (3), 599–610.

(50) Liu, C.; Xu, Y.; Noh, Y. Y. Contact Engineering in Organic Field-Effect Transistors. *Mater. Today* **2015**, *18* (2), 79–96.

(51) Kim, C. H.; Bonnassieux, Y.; Horowitz, G. Fundamental Benefits of the Staggered Geometry for Organic Field-Effect Transistors. *IEEE Electron Device Lett.* **2011**, *32* (9), 1302–1304.

(52) Di, C.; Liu, Y.; Yu, G.; Zhu, D. Interface Engineering: An Effective Approach toward High-Performance Organic Field-Effect Transistors. *Acc. Chem. Res.* **2009**, *42* (10), 1573–1583.

(53) Horowitz, G. Organic Thin Film Transistors: From Theory to Real Devices. *J. Mater. Res.* **2004**, *19* (7), 1946–1962.

(54) Dong, H.; Jiang, L.; Hu, W. Interface Engineering for High-Performance Organic Field-Effect Transistors. *Phys. Chem. Chem. Phys.* **2012**, *14* (41), 14165–14180.

(55) Newman, C. R.; Frisbie, C. D.; da Silva Filho, D. A.; Bredas, J.-L.; Ewbank, P. C.; Mann, K. R. Introduction to Organic Thin Film Transistors and Design of N-Channel Organic Semiconductors. *Chem. Mater.* **2004**, *16*, 4436–4451.

(56) Lamport, Z. A.; Haneef, H. F.; Anand, S.; Waldrip, M.; Jurchescu, O. D. Tutorial: Organic Field-Effect Transistors: Materials, Structure and Operation. *J. Appl. Phys.* **2018**, *124*, 071101.

(57) Xu, Y.; Sun, H.; Liu, A.; Zhu, H.; Li, B.; Minari, T.; Balestra, F.; Ghibaudo, G.; Noh, Y. Y. Essential Effects on the Mobility Extraction Reliability for Organic Transistors. *Adv. Funct. Mater*. **2018**, *28* (42), 1–14.

(58) Choi, H. H.; Cho, K.; Frisbie, C. D.; Sirringhaus, H.; Podzorov, V. Critical Assessment of Charge Mobility Extraction in FETs. *Nat. Mater.* **2017**, *17* (1), 2–7.

(59) Liu, C.; Li, G.; Di Pietro, R.; Huang, J.; Noh, Y. Y.; Liu, X.; Minari, T. Device Physics of Contact Issues for the Overestimation and Underestimation of Carrier Mobility in Field-Effect Transistors. *Phys. Rev. Appl.* **2017**, *8* (3), 034020.

(60) Uemura, T.; Rolin, C.; Ke, T. H.; Fesenko, P.; Genoe, J.; Heremans, P.; Takeya, J. On the Extraction of Charge Carrier Mobility in High-Mobility Organic Transistors. *Adv. Mater.* **2016**, *28* (1), 151–155.

(61) Paterson, A. F.; Singh, S.; Fallon, K. J.; Hodsden, T.; Han, Y.; Schroeder, B. C.; Bronstein, H.; Heeney, M.; Mcculloch, I.; Anthopoulos, T. D. Recent Progress in High-Mobility Organic Transistors : A Reality Check. *Adv. Mater*. **2018**, *30*, 1801079.

(62) Reese, C.; Bao, Z. Overestimation of the Field-Effect Mobility via Transconductance Measurements and the Origin of the Output / Transfer Characteristic Discrepancy in Organic Field-Effect Transistors Overestimation of the Field-Effect Mobility via Transconductance Measureme. *J. Appl. Phys.* **2015**, *105* (2009), 024506.

(63) Okachi, T.; Kashiki, T.; Ohya, K. Device Operation Mechanism of Field-Effect Transistors with High Mobility Donor-Acceptor Polymer Semiconductors. In *Organic Field-Effect Transistors XIV; and Organic Sensors and Bioelectronics VIII*; 2015; Vol. 9568, p 95680I–9568–8.

(64) Okachi, T. Mobility Overestimation Due to Minority Carrier Injection and Trapping in Organic Field-Effect Transistors. *Org. Electron.* **2018**, *57* (December 2017), 34–44.

(65) IEEE-SA Standards Board. *IEEE Standard for Test Methods for the Characterization of Organic Transistors and Materials*; 2008; Vol. 1620.

(66) Dimitrakopoulos, C. D.; Malenfant, P. R. L. Organic Thin Film Transistors for Large Area Electronics. *Adv. Mater.* **2002**, *14* (2), 99–117.

(67) Nikolka, M.; Nasrallah, I.; Rose, B.; Ravva, M. K.; Broch, K.; Sadhanala, A.; Harkin, D.; Charmet, J.; Hurhangee, M.; Brown, A.; et al. High Operational and Environmental Stability of High-Mobility Conjugated Polymer Field-Effect Transistors through the Use of Molecular Additives. *Nat. Mater.* **2017**, *16* (3), 356–362.

(68) Bronner, M.; Opitz, A.; Brutting, W. Ambipolar Charge Carrier Transport in

Organic Semiconductor Blends of Phthalocyanine and Fullerene. *Phys. Status Solidi Appl. Mater. Sci.* **2008**, *205*, 549–563.

(69) de Leeuw, D. M.; Simenon, M. M. J.; Brown, a. R.; Einerhand, R. E. F. Stability of N-Type Doped Conducting Polymers and Consequences for Polymeric Microelectronic Devices. *Synth. Met.* **1997**, *87*, 53–59.

(70) Wang, Z.; Kim, C.; Facchetti, A.; Marks, T. J. Anthracenedicarboximides as Air-Stable N-Channel Semiconductors for Thin-Film Transistors with Remarkable Current on-off Ratios. *J. Am. Chem. Soc.* **2007**, *129* (44), 13362–13363.

(71) Takimiya, K.; Osaka, I.; Nakano, M. π - Building Blocks for Organic Electronics: Revaluation of " Inductive " and " Resonance " E Ff Ects of π - Electron De Fi Cient Units. *Chem. Mater.* **2014**, *26*, 587–593.

(72) Chua, L.-L.; Zaumseil, J.; Chang, J.-F.; Ou, E. C.-W.; Ho, P. K.-H.; Sirringhaus, H.; Friend, R. H. General Observation of N-Type Field-Effect Behaviour in Organic Semiconductors. *Nature* **2005**, *434* (7030), 194–199.

(73) Phan, H.; Wang, M.; Bazan, G. C.; Nguyen, T. Q. Electrical Instability Induced by Electron Trapping in Low-Bandgap Donor-Acceptor Polymer Field-Effect Transistors. *Adv. Mater.* **2015**, *27* (43), 7004–7009.

(74) Bobbert, P. A.; Sharma, A.; Mathijssen, S. G. J.; Kemerink, M.; De Leeuw, D. M. Operational Stability of Organic Field-Effect Transistors. *Adv. Mater.* **2012**, *24* (9), 1146–1158.

(75) Di Girolamo, F. V.; Ciccullo, F.; Barra, M.; Carella, A.; Cassinese, A. Investigation on Bias Stress Effects in N-Type PDI8-CN 2 Thin-Film Transistors. *Org. Electron. physics, Mater. Appl.* **2012**, *13* (11), 2281–2289.

(76) Siol, C.; Melzer, C.; Von Seggern, H. Electron Trapping in Pentacene Based P- and n-Type Organic Field-Effect Transistors. *Appl. Phys. Lett.* **2008**, *93* (13), 1–4.

(77) Mathijssen, S. G. J.; Spijkman, M. J.; Andringa, A. M.; Van Hal, P. A.; McCulloch, I.; Kemerink, M.; Janssen, R. A. J.; De Leeuw, D. M. Revealing Buried Interfaces to Understand the Origins of Threshold Voltage Shifts in Organic Field-Effect Transistors. *Adv. Mater.* **2010**, *22* (45), 5105–5109.

(78) Tiwari, S. P.; Knauer, K. A.; Dindar, A.; Kippelen, B. Performance Comparison of Pentacene Organic Field-Effect Transistors with SiO 2 Modified with Octyltrichlorosilane or Octadecyltrichlorosilane. *Org. Electron. physics, Mater. Appl.* **2012**, *13* (1), 18–22.

(79) Ulman, A. Formation and Structure of Self-Assembled Monolayers. *Chem. Rev.* **1996**, *96* (4), 1533–1554.

(80) Angst, D. L.; Simmons, G. W. Moisture Absorption Characteristics of

Organosiloxane Self-Assembled Monolayers. *Langmuir* **1991**, *7*, 2236–2242.

(81) Nicolai, H. T.; Kuik, M.; Wetzelaer, G. A. H.; De Boer, B.; Campbell, C.; Risko, C.; Brédas, J. L.; Blom, P. W. M. Unification of Trap-Limited Electron Transport in Semiconducting Polymers. *Nat. Mater.* **2012**, *11* (10), 882–887.

(82) Quinn, J. T. E.; Zhu, J.; Li, X.; Wang, J.; Li, Y. Recent Progress in the Development of N-Type Organic Semiconductors for Organic Field Effect Transistors. *J. Mater. Chem. C* **2017**, *5* (34), 8654–8681.

(83) Okachi, T.; Kashiki, T.; Ohya, K. Device Operation Mechanism of Field-Effect Transistors with High Mobility Donor-Acceptor Polymer Semiconductors. *Proc. SPIE* **2015**, *14* (4), 420–426.

(84) Lamport, Z. A.; Barth, K. J.; Lee, H.; Gann, E.; Engmann, S.; Chen, H.; Guthold, M.; McCulloch, I.; Anthony, J. E.; Richter, L. J.; et al. A Simple and Robust Approach to Reducing Contact Resistance in Organic Transistors. *Nat. Commun.* **2018**, *9* (1).

(85) Bürgi, L.; Richards, T. J.; Friend, R. H.; Sirringhaus, H. Close Look at Charge Carrier Injection in Polymer Field-Effect Transistors. *J. Appl. Phys.* **2003**, *94* (9), 6129–6137.

(86) Ishii, B. H.; Sugiyama, K.; Ito, E.; Seki, K. Energy Level Alignment and Interfacial Electronic Structures at Organic/Metal and Organic/Organic Interfaces. *Adv. Mater.* **1999**, *11*, 605–625.

(87) van Woudenbergh, T.; Blom, P. W. M.; Huiberts, J. N. Electro-Optical Properties of a Polymer Light-Emitting Diode with an Injection-Limited Hole Contact. *Appl. Phys. Lett.* **2003**, *82* (6), 985–987.

(88) Van Woudenbergh, T.; Blom, P. W. M.; Vissenberg, M. C. J. M.; Huiberts, J. N. Temperature Dependence of the Charge Injection in Poly-Dialkoxy-p-Phenylene Vinylene. *Appl. Phys. Lett.* **2001**, *79* (11), 1697–1699.

(89) Tiwari, S. P.; Zhang, X. H.; Potscavage, W. J.; Kippelen, B. Study of Electrical Performance and Stability of Solution-Processed n -Channel Organic Field-Effect Transistors. *J. Appl. Phys.* **2009**, *106* (5).

(90) Wang, Y.; Hasegawa, T.; Matsumoto, H.; Michinobu, T. Significant Improvement of Unipolar N-Type Transistor Performances by Manipulating the Coplanar Backbone Conformation of Electron-Deficient Polymers via Hydrogen-Bonding. *J. Am. Chem. Soc.* **2019**.

(91) Ortiz, R. P.; Herrera, H.; Seoane, C.; Segura, J. L.; Facchetti, A.; Marks, T. J. Rational Design of Ambipolar Organic Semiconductors: Is Core Planarity Central to Ambipolarity in Thiophene-Naphthalene Semiconductors? *Chem. - A Eur. J.* **2012**, *18* (2), 532–543.

(92) Zaumseil, J.; Sirringhaus, H. Electron and Ambipolar Transport in Organic Field-Effect Transistors. *Chem. Rev.* **2007**, *107*, 1296–1323.

(93) Kim, F. S.; Guo, X.; Watson, M. D.; Jenekhe, S. A. High-Mobility Ambipolar Transistors and High-Cain Inverters from a Donor-Acceptor Copolymer Semiconductor. *Adv. Mater.* **2010**, *22* (4), 478–482.

(94) Jung, I. H.; Lo, W. Y.; Jang, J.; Chen, W.; Zhao, D.; Landry, E. S.; Lu, L.; Talapin, D. V.; Yu, L. Synthesis and Search for Design Principles of New Electron Accepting Polymers for All-Polymer Solar Cells. *Chem. Mater.* **2014**, *26* (11), 3450–3459.

(95) Durban, M. M.; Kazarinoff, P. D.; Luscombe, C. K. Synthesis and Characterization of Thiophene-Containing Naphthalene Diimide n-Type Copolymers for OFET Applications. *Macromolecules* **2010**, *43* (15), 6348–6352.

(96) Guo, X.; Ortiz, R. P.; Zheng, Y.; Hu, Y.; Noh, Y. Y.; Baeg, K. J.; Facchetti, A.; Marks, T. J. Bithiophene-Imide-Based Polymeric Semiconductors for Field-Effect Transistors: Synthesis, Structure-Property Correlations, Charge Carrier Polarity, and Device Stability. *J. Am. Chem. Soc.* **2011**, *133* (5), 1405–1418.

(97) Yuan, Z.; Fu, B.; Thomas, S.; Zhang, S.; Deluca, G.; Chang, R.; Lopez, L.; Fares, C.; Zhang, G.; Bredas, J.; et al. Unipolar Electron Transport Polymers: A Thiazole Based All-Electron Acceptor Approach. *Chem. Mater.* **2016**, *28*, 6045–6049.

(98) Kim, G.; Han, A.-R.; Lee, H. R.; Lee, J.; Oh, J. H.; Yang, C. Acceptor–acceptor Type Isoindigo-Based Copolymers for High-Performance n-Channel Field-Effect Transistors. *Chem. Commun.* **2014**, *50* (17), 2180.

(99) Lee, J. K.; Gwinner, M. C.; Berger, R.; Newby, C.; Zentel, R.; Friend, R. H.; Sirringhaus, H.; Ober, C. K. High-Performance Electron-Transporting Polymers Derived from a Heteroaryl Bis(Trifluoroborate). *J. Am. Chem. Soc.* **2011**, *133* (26), 9949–9951.

(100) Stalder, R.; Mei, J.; Subbiah, J.; Grand, C.; Estrada, L. A.; So, F.; Reynolds, J. R. N-Type Conjugated Polyisoindigos. *Macromolecules* **2011**, *44* (16), 6303–6310.

(101) Zhao, X.; Wen, Y.; Ren, L.; Ma, L.; Liu, Y.; Zhan, X. An Acceptor-Acceptor Conjugated Copolymer Based on Perylene Diimide for High Mobility n-Channel Transistor in Air. *J. Polym. Sci. Part A Polym. Chem.* **2012**, *50* (20), 4266–4271.

(102) Wang, Y.; Guo, H.; Harbuzaru, A.; Uddin, M. A.; Ling, S.; Yu, J.; Tang, Y.; Sun, H.; Wang, Y.; Guo, H.; et al. (Semi)Ladder-Type Bithiophene Imide-Based All-Acceptor Semiconductors : Synthesis , Structure-Property Correlations , and Unipolar n-Type Transistor Performance. *J. Am. Chem. Soc.* **2018**, *140*, 6096–6108.

(103) Xiao, M.; Onwubiko, A.; Yue, W.; Sirringhaus, H.; Wadsworth, A.; Nikolka, M.; Baran, D.; Chen, H.-Y.; McCulloch, I.; White, A. J. P. A Thieno[2,3-b]Pyridine-Flanked Diketopyrrolopyrrole Polymer as an n-Type Polymer Semiconductor for

All-Polymer Solar Cells and Organic Field-Effect Transistors. *Macromolecules* **2017**, *51* (1), 71–79.

(104) Letizia, J. A.; Salata, M. R.; Tribout, C. M.; Facchetti, A.; Ratner, M. A.; Marks, T. J. N-Channel Polymers by Design: Optimizing the Interplay of Solubilizing Substituents, Crystal Packing, and Field-Effect Transistor Characteristics in Polymeric Bithiophene-Imide Semiconductors. *J. Am. Chem. Soc.* **2008**, *130* (30), 9679–9694.

(105) Yan, H.; Chen, Z.; Zheng, Y.; Newman, C.; Quinn, J. R.; Dötz, F.; Kastler, M.; Facchetti, A. A High-Mobility Electron-Transporting Polymer for Printed Transistors. *Nature* **2009**, *457* (7230), 679–686.

(106) Sun, B.; Hong, W.; Yan, Z.; Aziz, H.; Li, Y. Record High Electron Mobility of 6.3 Cm2V−1s−1 Achieved for Polymer Semiconductors Using a New Building Block. *Adv. Mater.* **2014**, *26* (17), 2636–2642.

(107) Li, Y.; Sonar, P.; Singh, S. P.; Soh, M. S.; Van Meurs, M.; Tan, J. Annealing-Free High-Mobility Diketopyrrolopyrrole-Quaterthiophene Copolymer for Solution-Processed Organic Thin Film Transistors. *J. Am. Chem. Soc.* **2011**, *133* (7), 2198–2204.

(108) Sun, B.; Hong, W.; Aziz, H.; Li, Y. A Pyridine-Flanked Diketopyrrolopyrrole (DPP)-Based Donor–acceptor Polymer Showing High Mobility in Ambipolar and n-Channel Organic Thin Film Transistors. *Polym. Chem.* **2015**, *6* (6), 938–945.

(109) Mueller, C. J.; Singh, C. R.; Fried, M.; Huettner, S.; Thelakkat, M. High Bulk Electron Mobility Diketopyrrolopyrrole Copolymers with Perfluorothiophene. *Adv. Funct. Mater.* **2015**, *25* (18), 2725–2736.

(110) Nielsen, C. B.; Turbiez, M.; Mcculloch, I. Recent Advances in the Development of Semiconducting DPP-Containing Polymers for Transistor Applications. *Adv. Mater.* **2013**, *25*, 1859–1880.

(111) Su, H. L.; Sredojevic, D. N.; Bronstein, H.; Marks, T. J.; Schroeder, B. C.; Al-Hashimi, M. Bithiazole: An Intriguing Electron-Deficient Building for Plastic Electronic Applications. *Macromol. Rapid Commun.* **2017**, *38*, 1600610.

(112) Bronstein, H.; Hurhangee, M.; Fregoso, E. C.; Beatrup, D.; Soon, Y. W.; Huang, Z.; Hadipour, A.; Tuladhar, P. S.; Rossbauer, S.; Sohn, E. H.; et al. Isostructural, Deeper Highest Occupied Molecular Orbital Analogues of Poly(3-Hexylthiophene) for High-Open Circuit Voltage Organic Solar Cells. *Chem. Mater.* **2013**, *25* (21), 4239–4249.

(113) Fu, B.; Wang, C. Y.; Rose, B. D.; Jiang, Y.; Chang, M.; Chu, P. H.; Yuan, Z.; Fuentes-Hernandez, C.; Kippelen, B.; Bredas, J.-L.; et al. Molecular Engineering of Nonhalogenated Solution-Processable Bithiazole-Based Electron-Transport Polymeric Semiconductors. *Chem. Mater.* **2015**, *27* (8), 2928–2937.

(114) Guo, X.; Watson, M. D. Conjugated Polymers from Napthalene Bisimide. *Org. Lett.* **2008**, *10* (23), 5333–5336.

(115) Yue, J.; Sun, S.; Liang, J.; Zhong, W.; Lan, L.; Ying, L.; Huang, F.; Yang, W.; Cao, Y. Effects of Pyridyl Group Orientations on the Optoelectronic Properties of Regio-Isomeric Diketopyrrolopyrrole Based π-Conjugated Polymers. *J. Mater. Chem. C* **2016**, *4* (13), 2470–2479.

(116) Guo, F.; Liu, X.; Ding, Y.; Kong, F.; Chen, W.; Zhou, L.; Dai, S. Broad Spectral-Response Organic D–A–π–A Sensitizer with Pyridine-Diketopyrrolopyrrole Unit for Dye-Sensitized Solar Cells. *RSC Adv.* **2016**, *6* (16), 13433–13441.

(117) Hernandez, V.; Lopez Navarrete, J. T. Ab Initio Study of Torsional Potentials in 2,2′-Bithiophene and 3,4′- and 3,3′-Dimethyl-2,2′-Bithiophene as Models of the Backbone Flexibility in Polythiophene and Poly(3-Methylthiophene). *J. Chem. Phys.* **1994**, *101* (2), 1369–1377.

(118) Reichardt, C. Solvatochromic Dyes as Solvent Polarity Indicators. *Chem. Rev.* **1994**, *94* (8), 2319–2358.

(119) Spano, F. C. The Spectral Signatures of Frenkel Polarons in H-and J-Aggregates. *Acc. Chem. Res.* **2009**, *43* (3), 429–439.

(120) Kasha, M. Energy Transfer Mechanisms and the Molecular Exciton Model for Molecular Aggregates. *Radiat. Res.* **1963**, *20* (1), 55–70.

(121) Spano, F. C.; Silva, C. H- and J-Aggregate Behavior in Polymeric Semiconductors. *Annu. Rev. Phys. Chem.* **2014**, *65*, 477–500.

(122) Schwartz, B. J. Conjugated Polymers as Molecular Materials : How Chain Conformation and Film Morphology Influence Energy Transfer and Interchain Interactions. *Annu. Rev. Phys. Chem.* **2003**, *54* (1), 141–172.

(123) Hansen, W. N.; Hansen, G. J. Absolute Half-Cell Potential: A Simple Direct Measurement. *Phys. Rev. A* **1987**, *36* (3), 1396–1402.

(124) Bredas, J.-L. Mind the Gap! *Mater. Horizons* **2014**, *1*, 17–19.

(125) Yuan, Z.; Buckley, C.; Thomas, S.; Zhang, G.; Bargigia, I.; Wang, G.; Fu, B.; Silva, C.; Brédas, J.; Reichmanis, E. A Thiazole−Naphthalene Diimide Based N-Channel Donor−Acceptor Conjugated Polymer. *Macromolecules* **2018**, *51*, 7320–7328.

(126) Bujak, P.; Kulszewicz-bajer, I.; Zagorska, M.; Maurel, V.; Wielgus, I.; Pron, A. Polymers for Electronics and Spintronics. *Chem. Soc. Rev.* **2013**, *42*, 8895–8999.

(127) Barbara, P. F.; Meyer, T. J.; Ratner, M. A. Contemporary Issues in Electron Transfer Research. *J. Phys. Chem.* **1996**, *3654* (96), 13148–13168.

(128) Hulea, I. N.; Fratini, S.; Xie, H.; Mulder, C. L.; Iossad, N. N.; Rastelli, G.; Ciuchi, S.; Morpurgo, A. F. Tunable Frohlich Polarons in Organic Single-Crystal Transistors. *Nat. Mater.* **2006**, *5*, 982–986.

(129) Hoi, N. T.; Cho, D.; Andreasen, J. W.; Rouhanipour, A.; Breiby, D. W.; Pisula, W.; Mu, K. The Influence of Morphology on High-Performance Polymer Field-Effect Transistors. *Adv. Mater.* **2009**, *21*, 209–212.

(130) Noriega, R.; Rivnay, J.; Vandewal, K.; Koch, F. P. V; Stingelin, N.; Smith, P.; Toney, M. F.; Salleo, A. A General Relationship between Disorder, Aggregation and Charge Transport in Conjugated Polymers. *Nat. Mater.* **2013**, *12*, 1038–1044.

(131) Chang, M.; Lim, G. T.; Park, B.; Reichmanis, E. Control of Molecular Ordering, Alignment, and Charge Transport in Solution-Processed Conjugated Polymer Thin Films. *Polymers (Basel).* **2017**, *9* (6), 23–31.

(132) Horowitz, G.; Hajlaoui, R.; Bouchriha, H.; Bourguiga, R.; Hajlaoui, M. Concept of `threshold Voltage' in Organic Field-Effect Transistors. *Adv. Mater.* **1998**, *10* (12), 923–927.

(133) Findlater, M.; Swisher, N. S.; White, P. S. Synthesis and Structure of Boron-Bithiazole Complexes. *Eur. J. Inorg. Chem.* **2010**, *302* (34), 5379–5382.

(134) Virkar, A. A.; Mannsfeld, S.; Bao, Z.; Stingelin, N. Organic Semiconductor Growth and Morphology Considerations for Organic Thin-Film Transistors. *Adv. Mater.* **2010**, *22* (34), 3857–3875.

(135) Botiz, I.; Stingelin, N. Influence of Molecular Conformations and Microstructure on the Optoelectronic Properties of Conjugated Polymers. *Materials (Basel).* **2014**, *7* (3), 2273–2300.

(136) Rivnay, J.; Mannsfeld, S. C. B.; Miller, C. E.; Salleo, A.; Toney, M. F. Quantitative Determination of Organic Semiconductor Microstructure from the Molecular to Device Scale. *Chem. Rev.* **2012**, *112* (10), 5488–5519.

(137) Perez, L. A.; Zalar, P.; Ying, L.; Schmidt, K.; Toney, M. F.; Nguyen, T. Q.; Bazan, G. C.; Kramer, E. J. Effect of Backbone Regioregularity on the Structure and Orientation of a Donor-Acceptor Semiconducting Copolymer. *Macromolecules* **2014**, *47* (4), 1403–1410.

(138) Arias, A. C.; MacKenzie, J. D.; McCulloch, I.; Rivnay, J.; Salleo, A. Materials and Applications for Large Area Electronics: Solution-Based Approaches. *Chem. Rev.* **2010**, *110* (1), 3–24.

(139) Bao, Z. Materials and Fabrication Needs for Low-Cost Organic Transistor Circuits. *Adv. Mater.* **2000**, *12* (3), 227–230.

(140) Zhang, L.; Di, C. A.; Yu, G.; Liu, Y. Solution Processed Organic Field-Effect

Transistors and Their Application in Printed Logic Circuits. *J. Mater. Chem.* **2010**, *20* (34), 7059–7073.

(141) Krebs, F. C. Fabrication and Processing of Polymer Solar Cells: A Review of Printing and Coating Techniques. *Sol. Energy Mater. Sol. Cells* **2009**, *93* (4), 394–412.

(142) Hernandez, J. L.; Deb, N.; Wolfe, R. M. W.; Lo, C. K.; Engmann, S.; Richter, L. J.; Reynolds, J. R. Simple Transfer from Spin Coating to Blade Coating through Processing Aggregated Solutions. *J. Mater. Chem. A* **2017**, *5* (39), 20687–20695.

(143) Zhang, F. J.; Di, C. A.; Berdunov, N.; Hu, Y.; Hu, Y.; Gao, X.; Meng, Q.; Sirringhaus, H.; Zhu, D. Ultrathin Film Organic Transistors: Precise Control of Semiconductor Thickness via Spin-Coating. *Adv. Mater.* **2013**, *25* (10), 1401–1407.

(144) Nguyen, T. Q.; Doan, V.; Schwartz, B. J. Conjugated Polymer Aggregates in Solution: Control of Interchain Interactions. *J. Chem. Phys.* **1999**, *110* (8), 4068–4078.

(145) Meyerhofer, D. Characteristics of Resist Films Produced by Spinning. *J. Appl. Phys.* **1978**, *49* (7), 3993–3997.

(146) Wang, G.; Huang, W.; Eastham, N. D.; Fabiano, S.; Manley, E. F.; Zeng, L.; Wang, B.; Zhang, X.; Chen, Z.; Li, R.; et al. Aggregation Control in Natural Brush-Printed Conjugated Polymer Films and Implications for Enhancing Charge Transport. *Proc. Natl. Acad. Sci.* **2017**, *114* (47), E10066–E10073.

(147) Li, M.; An, C.; Pisula, W.; Müllen, K. Alignment of Organic Semiconductor Microstripes by Two-Phase Dip-Coating. *Small* **2014**, *10* (10), 1926–1931.

(148) Wu, K.; Li, H.; Li, L.; Zhang, S.; Chen, X.; Xu, Z.; Zhang, X.; Hu, W.; Chi, L.; Gao, X.; et al. Controlled Growth of Ultrathin Film of Organic Semiconductors by Balancing the Competitive Processes in Dip-Coating for Organic Transistors. *Langmuir* **2016**, *32* (25), 6246–6254.

(149) Diao, Y.; Shaw, L.; Bao, Z.; Mannsfeld, S. C. B. Morphology Control Strategies for Solution-Processed Organic Semiconductor Thin Films. *Energy Environ. Sci.* **2014**, *7* (7), 2145–2159.

(150) Gu, X.; Shaw, L.; Gu, K.; Toney, M. F.; Bao, Z. The Meniscus-Guided Deposition of Semiconducting Polymers. *Nat. Commun.* **2018**, *9* (1).

(151) Wu, D.; Kaplan, M.; Ro, H. W.; Engmann, S.; Fischer, D. A.; DeLongchamp, D. M.; Richter, L. J.; Gann, E.; Thomsen, L.; McNeill, C. R.; et al. Blade Coating Aligned, High-Performance, Semiconducting-Polymer Transistors. *Chem. Mater.* **2018**, acs.chemmater.7b04835.

(152) Shaw, L.; Yan, H.; Gu, X.; Hayoz, P.; Weitz, R. T.; Kaelblein, D.; Toney, M. F.;

Bao, Z. Microstructural Evolution of the Thin Films of a Donor-Acceptor Semiconducting Polymer Deposited by Meniscus-Guided Coating. *Macromolecules* **2018**, *51* (11), 4325–4340.

(153) Giri, G.; Delongchamp, D. M.; Reinspach, J.; Fischer, D. A.; Richter, L. J.; Xu, J.; Benight, S.; Ayzner, A.; He, M.; Fang, L.; et al. Effect of Solution Shearing Method on Packing and Disorder of Organic Semiconductor Polymers. *Chem. Mater.* **2015**, *27* (7), 2350–2359.

(154) Richter, L. J.; Delongchamp, D. M.; Amassian, A. Morphology Development in Solution-Processed Functional Organic Blend Films: An in Situ Viewpoint. *Chem. Rev.* **2017**, *117* (9), 6332–6366.

(155) Liu, F.; Gu, Y.; Jung, J. W.; Jo, W. H.; Russell, T. P. On the Morphology of Polymer-Based Photovoltaics. *J. Polym. Sci. Part B Polym. Phys.* **2012**, *50* (15), 1018–1044.

(156) Kuei, B.; Gomez, E. D. Chain Conformations and Phase Behavior of Conjugated Polymers. *Soft Matter* **2017**, *13* (1), 49–67.

(157) Noriega, R.; Salleo, A.; Spakowitz, A. J. Chain Conformations Dictate Multiscale Charge Transport Phenomena in Disordered Semiconducting Polymers. *Proc. Natl. Acad. Sci.* **2013**, *110* (41), 16315–16320.

(158) Stafford, C. M.; Roskov, K. E.; Epps, T. H.; Fasolka, M. J. Generating Thickness Gradients of Thin Polymer Films via Flow Coating. *Rev. Sci. Instrum.* **2006**, *77* (2), 23908.

(159) Becerril, H. A.; Roberts, M. E.; Liu, Z.; Locklin, J.; Bao, Z. High-Performance Organic Thin-Film Transistors through Solution-Sheared Deposition of Small-Molecule Organic Semiconductors. *Adv. Mater.* **2008**, *20* (13), 2588–2594.

(160) Le Berre, M.; Chen, Y.; Baigl, D. From Convective Assembly to Landau - Levich Deposition of Multilayered Phospholipid Films of Controlled Thickness. *Langmuir* **2009**, *25* (5), 2554–2557.

(161) Yuan, Z. Design, Synthesis and Characterization of Thiazole-Based Conjugated Polymers and Their Applications to N-Channel Organic Electronics, Georgia Institute of Technology, 2018.

(162) Prentice, G. M.; Pascu, S. I.; Filip, S. V; West, K. R.; Pantoş, G. D. Aromatic Donor–acceptor Interactions in Non-Polar Environments. *Chem. Commun.* **2015**, *51* (39), 8265–8268.

(163) Chen, Z.; Zheng, Y.; Yan, H.; Facchetti, A. Naphthalenedicarboximide- vs Perylenedicarboximide-Based Copolymers. Synthesis and Semiconducting Properties in Bottom-Gate N-Channel Organic Transistors. *J. Am. Chem. Soc.* **2009**, *131* (1), 8–9.

(164) Pirotte, G.; Agarkar, S.; Xu, B.; Zhang, J.; Lutsen, L.; Vanderzande, D.; Yan, H.; Pollet, P.; Reynolds, J. R.; Maes, W.; et al. Molecular Weight Tuning of Low Bandgap Polymers by Continuous Flow Chemistry: Increasing the Applicability of PffBT4T for Organic Photovoltaics. *J. Mater. Chem. A* **2017**, *5* (34), 18166–18175.

(165) Owens, D. K.; Wendt, R. C. Estimation of the Surface Free Energy of Polymers. *J. Appl. Polym. Sci.* **1969**, *13*, 1741–1747.

(166) Müller, C. On the Glass Transition of Polymer Semiconductors and Its Impact on Polymer Solar Cell Stability. *Chem. Mater.* **2015**, *27* (8), 2740–2754.

(167) Steyrleuthner, R.; Schubert, M.; Howard, I.; Klaumünzer, B.; Schilling, K.; Chen, Z.; Saalfrank, P.; Laquai, F.; Facchetti, A.; Neher, D. Aggregation in a High-Mobility n-Type Low-Bandgap Copolymer with Implications on Semicrystalline Morphology. *J. Am. Chem. Soc.* **2012**, *134* (44), 18303–18317.

(168) Rivnay, B. J.; Toney, M. F.; Zheng, Y.; Kauvar, I. V; Chen, Z.; Wagner, V.; Facchetti, A.; Salleo, A. Unconventional Face-On Texture and Exceptional In-Plane Order of a High Mobility n-Type Polymer. *Adv. Mater.* **2010**, *22*, 4359–4363.

(169) Wasserman, S. R.; Tao, Y.; Whitesides, G. M. Structure and Reactivity of Alkylsiloxane Monolayers Formed by Reaction of Alkyltrichlorosilanes on Silicon Substrates. **1989**, 1074–1087.

(170) GmbH, D. Surface Tension of p-Xylene http://www.ddbst.com/en/EED/PCP/SFT_C176.php.

(171) Sigma-Aldrich. Safety Data Sheet 296333 p-Xylene https://www.sigmaaldrich.com/MSDS/MSDS/DisplayMSDSPage.do?country=US&language=en&productNumber=296333&brand=SIAL&PageToGoToURL=https%3A%2F%2Fwww.sigmaaldrich.com%2Fcatalog%2Fproduct%2Fsial%2F296333%3Flang%3Den.

(172) Yang, H.; Shin, T. J.; Yang, L.; Cho, K.; Ryu, C. Y.; Bao, Z. Effect of Mesoscale Crystalline Structure on the Field-EffectMobility of Regioregular Poly(3-Hexyl Thiophene) in Thin-FilmTransistors. *Adv. Funct. Mater.* **2005**, *15*, 671–676.

(173) Salleo, A.; Chabinyc, M. L.; Yang, M. S.; Street, R. A. Polymer Thin-Film Transistors with Chemically Modified Dielectric Interfaces. *Appl. Phys. Lett.* **2002**, *81* (23), 4383–4385.

(174) Salleo, A.; Chen, T. W.; Völkel, A. R.; Wu, Y.; Liu, P.; Ong, B. S.; Street, R. A. Intrinsic Hole Mobility and Trapping in a Regioregular Poly(Thiophene). *Phys. Rev. B - Condens. Matter Mater. Phys.* **2004**, *70* (11), 1–10.

(175) Kline, R. J.; DeLongchamp, D. M.; Fischer, D. A.; Lin, E. K.; Heeney, M.; McCulloch, I.; Toney, M. F. Significant Dependence of Morphology and Charge Carrier Mobility on Substrate Surface Chemistry in High Performance

Polythiophene Semiconductor Films. *Appl. Phys. Lett.* **2007**, *90* (6).

(176) Wang, S.; Kiersnowski, A.; Pisula, W.; Müllen, K. Microstructure Evolution and Device Performance in Solution-Processed Polymeric Field-Effect Transistors: The Key Role of the First Monolayer. *J. Am. Chem. Soc.* **2012**, *134* (9), 4015–4018.

(177) Wang, S.; Pisula, W.; Müllen, K. Nanofiber Growth and Alignment in Solution Processed N-Type Naphthalene-Diimide-Based Polymeric Field-Effect Transistors. *J. Mater. Chem.* **2012**, *22* (47), 24827–24831.

(178) Bucella, S. G.; Luzio, A.; Gann, E.; Thomsen, L.; McNeill, C. R.; Pace, G.; Perinot, A.; Chen, Z.; Facchetti, A.; Caironi, M. Macroscopic and High-Throughput Printing of Aligned Nanostructured Polymer Semiconductors for MHz Large-Area Electronics. *Nat. Commun.* **2015**, *6*, 8394.

(179) Wang, G.; Chu, P. H.; Fu, B.; He, Z.; Kleinhenz, N.; Yuan, Z.; Mao, Y.; Wang, H.; Reichmanis, E. Conjugated Polymer Alignment: Synergisms Derived from Microfluidic Shear Design and UV Irradiation. *ACS Appl. Mater. Interfaces* **2016**, *8* (37), 24761–24772.

(180) Snyder, C. R.; Kline, R. J.; Delongchamp, D. M.; Nieuwendaal, R. C.; Richter, L. J.; Heeney, M.; McCulloch, I. Classification of Semiconducting Polymeric Mesophases to Optimize Device Postprocessing. *J. Polym. Sci. Part B Polym. Phys.* **2015**, *53* (23), 1641–1653.

(181) Yasuda, T.; Fujita, K.; Nakashima, H.; Tsutsui, T. Organic Field-Effect Transistors with Gate Dielectric Films of Poly-p-Xylylene Derivatives Prepared by Chemical Vapor Deposition. *Japanese J. Appl. Physics, Part 1 Regul. Pap. Short Notes Rev. Pap.* **2003**, *42* (10), 6614–6618.

(182) Karpov, Y.; Zhao, W.; Raguzin, I.; Beryozkina, T.; Bakulev, V.; Al-Hussein, M.; Häußler, L.; Stamm, M.; Voit, B.; Facchetti, A.; et al. Influence of Semiconductor Thickness and Molecular Weight on the Charge Transport of a Naphthalenediimide-Based Copolymer in Thin-Film Transistors. *ACS Appl. Mater. Interfaces* **2015**, *7* (23), 12478–12487.